Seismic Structure of the Crust and Upper Mantle in the Southwestern United States Using Teleseismic Receiver Functions

by

David C. Wilson

Submitted in Partial Fulfillment

of the Requirements for the Degree of

Doctor of Philosophy in Earth and Environmental Science

with Dissertation in Geophysics

New Mexico Institute of Mining and Technology

Socorro, New Mexico

May, 2004

ABSTRACT

This dissertation describes the development of receiver function processing methods to create images of the seismic structure of the crust and upper mantle from teleseismic earthquake arrivals. These methods include receiver function estimation and prestack migration techniques which reduce deconvolution instability and produce regularized, multi-phase receiver function images.

The receiver function estimation technique developed here builds on frequency-wavenumber filtering methods by transforming receiver functions into the frequency-pseudo-wavenumber domain. A filter is then applied that downweights receiver function amplitudes that have a high degree of variability as a function of horizontal slowness (epicentral distance) while preserving receiver function phases that have consistent moveout characteristics. This technique is applied to synthetic receiver functions and shows excellent recovery of receiver function phases in the presence of high noise. A receiver function migration technique is developed that is based on regularized Kirchhoff migration. This technique migrates both direct and reverberated P-to-S converted phases to their true subsurface position to produce an image of the velocity discontinuity structure of the subsurface. This migration technique is applied to synthetic receiver functions to demonstrate that it is especially well suited

to irregularly spaced stations and uneven data coverage. An important aspect of both the deconvolution and migration techniques is that they do not require the recording of a single earthquake at multiple stations, making them especially applicable to temporary arrays that may have irregular recording times between stations and allow the incorporation of previous teleseismic data.

The receiver function processing methods described in this dissertation are applied to teleseismic arrivals recorded in the LA RISTRA (Colorado PLAteau, Rio Grande RIft, Great Plains Seismic TRAnsect) experiment. LA RISTRA was a NW-SE trending, 950.7 km linear network of broadband PASSCAL seismometers, deployed during 1999-2001 from Lake Powell, UT to Pecos, TX. Results from application of these methods to LA RISTRA data show much more topography at the base of the crust than has been observed in this region previously, with thickness changes up to 7 km over lateral distances of 50 km. Crustal thickness beneath the LA RISTRA network reaches a minimum of 35 km in the center of the Rio Grande rift (RGR), and ranges from 42 to 50 km in both the Great Plains (GP) and Colorado Plateau (CP). Crustal thinning beneath the RGR is relatively symmetric about the rift axis, with the thinnest crust located directly beneath the rift axis, suggesting a predominantly pure shear stretching of the lithosphere beneath the RGR. This is further supported by the rift centered region of low velocities observed in surface wave inversions and tomography results, as well as by regional isotopic data. Colorado Plateau

crust is on average 2.7 km thicker than Great Plains crust, providing up to .5 km of Colorado Plateau uplift. This, along with added buoyancy from a deep, low-velocity channel imaged in surface wave analysis, may explain the excess elevation of the Colorado Plateau. Lithospheric receiver function images also indicate a prominent northwest-dipping discontinuity, ranging from 65 to 85 km deep beneath the CP, and possible sub-crustal discontinuities beneath the GP. These discontinuities, along with recent xenolith data, may indicate preserved ancient lithospheric structures such as relict suture zones or subducted slabs associated with Proterozoic subduction. Upper mantle receiver function images beneath the LA RISTRA network show a prominent discontinuity at 250-300 km depth that may correlate with similar discontinuities observed beneath eastern North America. This discontinuity may represent the base of an asthenospheric low velocity channel observed in surface wave velocity images. Upper Mantle discontinuities at 410 and 660 km depth are relatively flat, indicating there is not a large scale thermal anomaly beneath the RGR at these depths.

ACKNOWLEDGMENT

Thanks to my advisor, Rick Aster, for insight, encouragement, and support (both financial and moral). Thanks also to the members of my committee: Kent Condie, Harold Tobin, John Schlue, and Dave Westpfahl. I have received countless hours of valuable discussion with the members of the RISTRA research group, including Jim Ni, Steve Grand, Mike West, Anca Rosca, Rengin Gok, Wei Gao, Steve Semken, and Scott Baldridge. Thanks to Gary Pavlis for many discussions on the finer philosophical points of receiver functions. Thanks also to my wife, Jen, for geologic input, endless support, and for pulling me away from the computer long enough to enjoy the sunshine. This research supported by NSF grants EAR 9707190 and EAR 9706094, and the Los Alamos National Laboratory Institute for Geophysics and Planetary Physics.

This dissertation was typeset with LaTeX[1] by the author.

[1] LaTeX document preparation system was developed by Leslie Lamport as a special version of Donald Knuth's TeX program for computer typesetting. TeX is a trademark of the American Mathematical Society. The LaTeX macro package for the New Mexico Institute of Mining and Technology dissertation format was adapted from Gerald Arnold's modification of the LaTeX macro package for The University of Texas at Austin by Khe-Sing The.

TABLE OF CONTENTS

LIST OF TABLES

LIST OF FIGURES

This dissertation is accepted on behalf of the faculty of the Institute by the following committee:

Richard C. Aster, Advisor

David C. Wilson

Date

CHAPTER 1

Introduction

The primary aim of this project has been the development of receiver function estimation and imaging techniques as a primary application of data from the Colorado PLateau/Rio Grande RIft/Great Plains Seismic TRAnsect (LA RISTRA) experiment. LA RISTRA is designed to image and interpret crust and mantle structures beneath the southwestern United States. Key questions addressed by LA RISTRA relate both to specific issues associated with the southwestern U.S. and general issues associated with the evolution of the crust and mantle. These questions include the nature of crustal and mantle structures and thermal conditions beneath the Rio Grande rift, and clues to understanding the anomalously unextended Colorado Plateau, which is currently surrounded by the predominantly extensional deformation of the American West.

The data collecting stage of LA RISTRA provided 18 months (1999-2001) of broadband teleseismic data along a 950-km great-circle transect of 54 sites with 18±3.6 km station spacing with endpoints near Lake Powell, UT and Pecos, TX (Figure 1.1). The northwest-southeast trending transect was oriented parallel to the azimuth of the very active western Pacific seismogenic zones. LA RISTRA data are now freely available from the Incorporated Research Institutions for Seismology (IRIS) Data Management Center (DMC) (http://www.iris.edu). Table A.1 contains detailed specifications for the LA RISTRA stations, including time of deployment for each station. Analysis applied to this seismic data set by other members of the LA RISTRA team includes surface wave dispersion inversion for crustal and mantle structure (West et al., 2004), teleseismic body wave tomography (Gao et al., 2004), and teleseismic mantle anisotropy (Gok et al., 2003). This dissertation focuses on the

use of RISTRA data to examine lithospheric structure using P-to-S mantle and crustal forward scattering, observed in the S phases immediately following (several tens of seconds) the teleseismic P arrival.

The area covered by LA RISTRA has a geologic history spanning nearly 2 b.y. The crustal basement of the region was assembled in a series of continental accretionary events in which island arcs, oceanic plateaus, and marginal basin terranes were succesively adhered to the continent (Condie, 1982; Bowring and Karlstrom, 1990). LA RISTRA follows the approximate continental age accretionary gradient to cross two major Proterozoic province boundaries, the Mazatzal and Yavapai (1.6-1.7 b.y. old and 1.7-1.8 b.y. old, respectively) suture in the northwest, and entering the Grenville ($\approx$ 1.1 b.y. old) province near the eastern edge of the Delaware basin in the southeast (Figure 1.1).

The LA RISTRA region underwent east-west compression during the Mesozoic (80-50 Ma) Laramide orogeny as the Farallon slab was subducting beneath western North America. During this period the slab is thought to have been subducting at a low angle (e.g., Dickinson and Snyder, 1978). Between approximately 43 and 30 Ma, as the initiation of the San Andreas fault was shutting off subduction, a portion of the slab may have detached, spurring the dramatically enhanced volcanism in the southwestern U.S. referred to as the "ignimbrite flare-up" (Humphreys, 1995). During the past 30 m.y. the region has been in extension, along with much of interior western North America. This regional extension stimulated the formation of the Rio Grande rift along a concentrated north-south zone of extension, while leaving the adjacent Col-

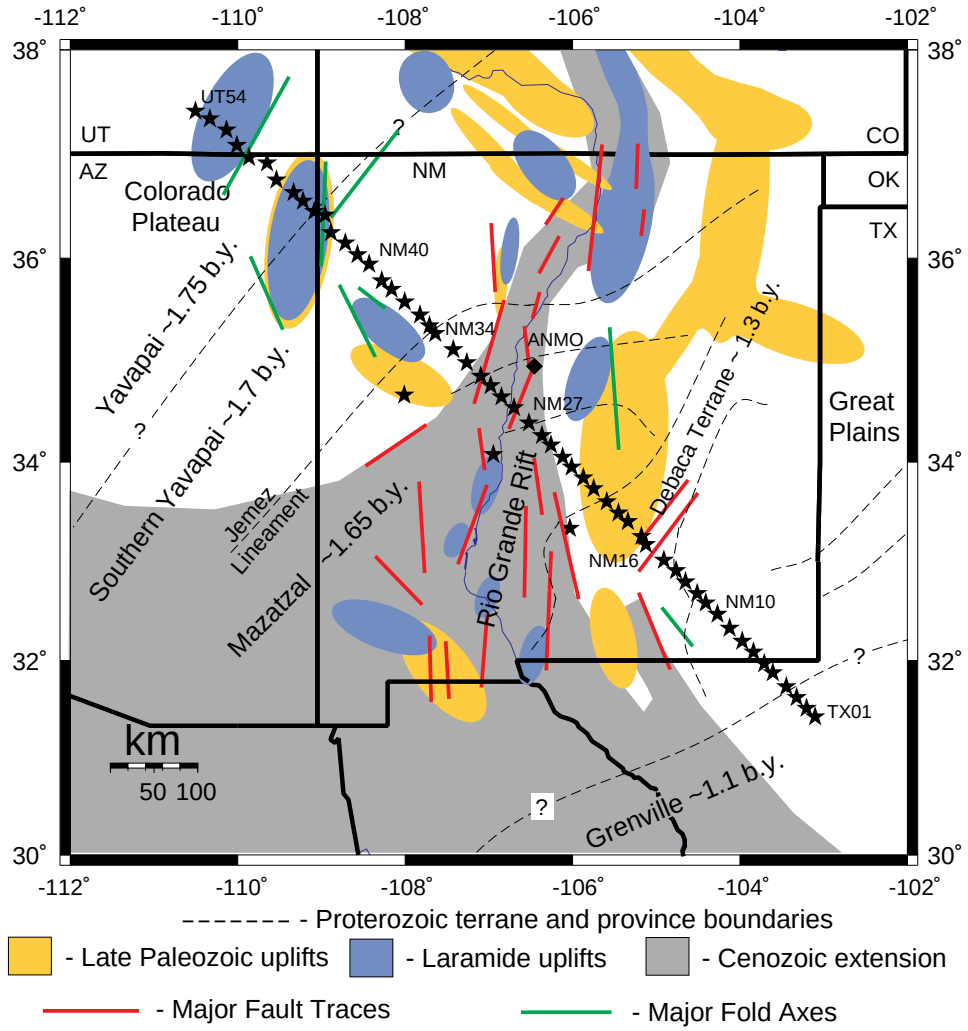

Figure 1.1: Regional tectonic setting of the LA RISTRA network, compiled from Baldridge et al. (1995), Bowring and Karlstrom (1990), Reed and others (1993), and Sloss (1988).

orado Plateau relatively undeformed. Rifting is thought to have formed in at least two stages (e.g., Olsen et al., 1987). An initial stage at 30 to 20 Ma, associated with low angle faulting and doming in the crust, may have been caused by upper-mantle asthenospheric upwelling and thermal erosion of the lithosphere. After perhaps 10 m.y. of quiescence, a second stage of rift activity resumed with high-angle normal faulting and alkalic basaltic volcanism. During the past 4 m.y., there has been increased volcanism along the Jemez Lineament, which approximately follows the Yavapai/Mazatzal suture.

These tectonic and geologic issues are addressed in the following chapters through the development and application of receiver function estimation and imaging methodologies to produce an image of the crust and upper mantle discontinuity structure beneath LA RISTRA.

1.1 Organization

Chapter 2 is a detailed analysis of the background seismic noise environment of the LA RISTRA array. This chapter was published in the *Bulletin of the Seismological Society of America* with co-authors Joe Leon, Rick Aster, Jim Ni, John Schlue, Steve Grand, Steve Semken, W. Scott Baldridge, and Wei Gao. This noise analysis is work that was started as an independent study by co-author Joe Leon (Leon, 2001). I subsequently reprocessed the data used in his study and applied additional analysis such as quantifying the spatial correlation of the background noise.

Chapters 3 and 4 are to be submitted as companion papers to the *Journal of Geophysical Research* with co-authors Rick Aster, Jim Ni, Steve

Grand, Mike West, Wei Gao, W. Scott Baldridge, and Steve Semken. The chapters constitute the focus of this dissertation: the development of receiver function estimation and imaging methods, and their application to LA RISTRA data. The interpretation of LA RISTRA results has been a cooperative effort between LA RISTRA coworkers.

Chapter 5 is a detailed examination of the lithospheric structure beneath the Rio Grande rift. This chapter has been submitted to *Nature* with co-authors Mike West, Rick Aster, Jim Ni, Steve Grand, Wei Gao, W. Scott Baldridge, and Steve Semken. This chapter addresses the symmetric nature of crustal thinning beneath the Rio Grande rift, as well as the symmetry observed in the upper mantle velocity structure beneath the rift, and its implications for pure shear lithospheric deformation of the Rio Grande rift lithosphere.

CHAPTER 2

Background Noise Analysis of LA RISTRA Seismic Stations[1]

[1]This chapter has appeared in the *Bulletin of the Seismological Society of America*: Wilson, D., J. Leon, R. Aster, J. Ni, J. Schlue, S. Grand, S. Semken, S. Baldridge, and W. Gao, Broadband Seismic Background Noise at Temporary Seismic Stations Observed on a Regional Scale in the Southwestern United States, *Bull. Seis. Soc. Amer.*, 92, n. 8, 3335–3341, (2002).

Abstract

Background noise Power Spectral Density (PSD) estimates for 54 PASSCAL LA RISTRA (Colorado p**LA**teau/**RI**o Grande Rift/Great Plains **S**eismic **TRA**nsect) stations were computed using data from 1999-2000. At long periods (0.01 to 0.1 Hz) typical vertical noise levels are approximately 12 dB higher than the nearby GSN borehole station ANMO, but horizontal power spectral density (PSD) noise levels are approximately 30 dB higher. Long period noise levels exhibit essentially no spatial correlation along the LA RISTRA transect, indicating that local thermal or atmosphere-driven local slab tilt is the dominant source of noise in this band. Between 0.1 and 0.3 Hz, typical noise levels are dominated by naturally occurring microseismic noise and are essentially identical to those observed at ANMO. At short periods, 0.3 to 8 Hz, typical noise levels along the network exceed ANMO levels by approximately 15 dB, with the highest levels corresponding to proximity to cultural noise sources. No significant day/night variations were observed in the microseismic band, however, both low and high frequency noise levels show an increase of up to 8 dB in median midday versus midnight noise levels. We find that the major shortcomings of these shallow PASSCAL-style temporary vaults relative to a GSN-style borehole installation are increased susceptibility to long-period horizontal ($\geq$ 20 s) noise and to surface noise sources above approximately 2 Hz. Although the high-frequency near-surface noise field is unavoidable in shallow vaults, we suggest that increased understanding and mitigation of local tilt effects in shallow vaults offers the possibility of significantly improving the long-period noise environment.

2.1 Introduction

With the advent of ever larger campaign deployments of broadband seismometers (e.g., Kennett and van der Hilst, 1996; Henyey, 2000) for periods of several months to years, it is increasingly imperative to rapidly identify high signal-to-noise sites and to standardize and optimize the design of portable seismometer vaults. We examine ambient background noise levels from the RISTRA experiment, a relatively long (950.7 km) and densely occupied (18.1 $\pm$ 3.6 km) network of IRIS PASSCAL broadband seismic stations, to investigate factors that influence noise levels. RISTRA and similar broadband deployments are commonly designed to image mantle and gross crustal structures by recording high signal-to-noise teleseismic signals ranging from long period surface waves through short period body waves.

Although noise can be dominated by the recording system in rare instances (e.g., Rodgers et al., 1987), or at extremely quiet sites, system noise levels with currently standard 24-bit dynamic range recorders and broadband seismometers such as those used in the PASSCAL program are typically well below those of the ambient natural and cultural seismic noise field.

Principal natural noise sources include microseisms, diurnal temperature and other atmospheric conditions (Zurn and Widmer, 1995; Beauduin et al., 1996), flow and waves associated with regional rivers and lakes, and wind. Principal cultural sources of noise are generally transportation corridors (roads, railways, pipelines, etc.). At high frequencies (above 0.3 Hz), the seismic noise field is commonly dominated by cultural- or wind-generated noise (e.g., Rodgers et al., 1987; Withers et al., 1996; Young et al., 1996; Given

and Fels, 1993; Given, 1990; Gurrola et al., 1990; Peterson, 1993; Vila, 1998; Uhrhammer, 2000), with wind noise being the predominant high frequency noise source at remote sites (e.g., Withers et al., 1996).

2.2 RISTRA Seismic Data

To address the regional tectonic questions of mantle and crustal rifting processes in the Rio Grande rift and geophysical conditions underlying the Colorado Plateau (e.g., Baldridge et al, 1995), the RISTRA team recently (May, 2001) completed the collection of seismic data along a 950.7 km transect running NW-SE from Lake Powell, Utah, near the center of the Colorado plateau, across the central Rio Grande rift, and into the Great Plains near Pecos, Texas (Figure 2.1a). RISTRA consisted of 57 continuously recording PASSCAL broadband stations deployed between August, 1999 and May, 2001.

Locating RISTRA stations uniformly along a great-circle path aligned with teleseismic source zones along a western South American-Alaskan transect resulted in very diverse local site conditions, ranging from remote sites on Colorado plateau bedrock to culturally compromised sites on deep alluvium in sight of dwellings and highways (Figure 2.1b). Due to experimental design preferences, such as uniform station spacing, and access issues, local cultural noise sources such as oil field operations, ranch improvements, and roads, could not always be avoided. Although RISTRA occupied sites on Private, National Forest, Bureau of Land Management, New Mexico State Land Office, Navajo Nation, Laguna Pueblo, and Isleta Pueblo lands, we note that, with informational mailings, coupled with preliminary on-site visits with landowners and land managers, beginning approximately 1 year before deployment, we encoun-

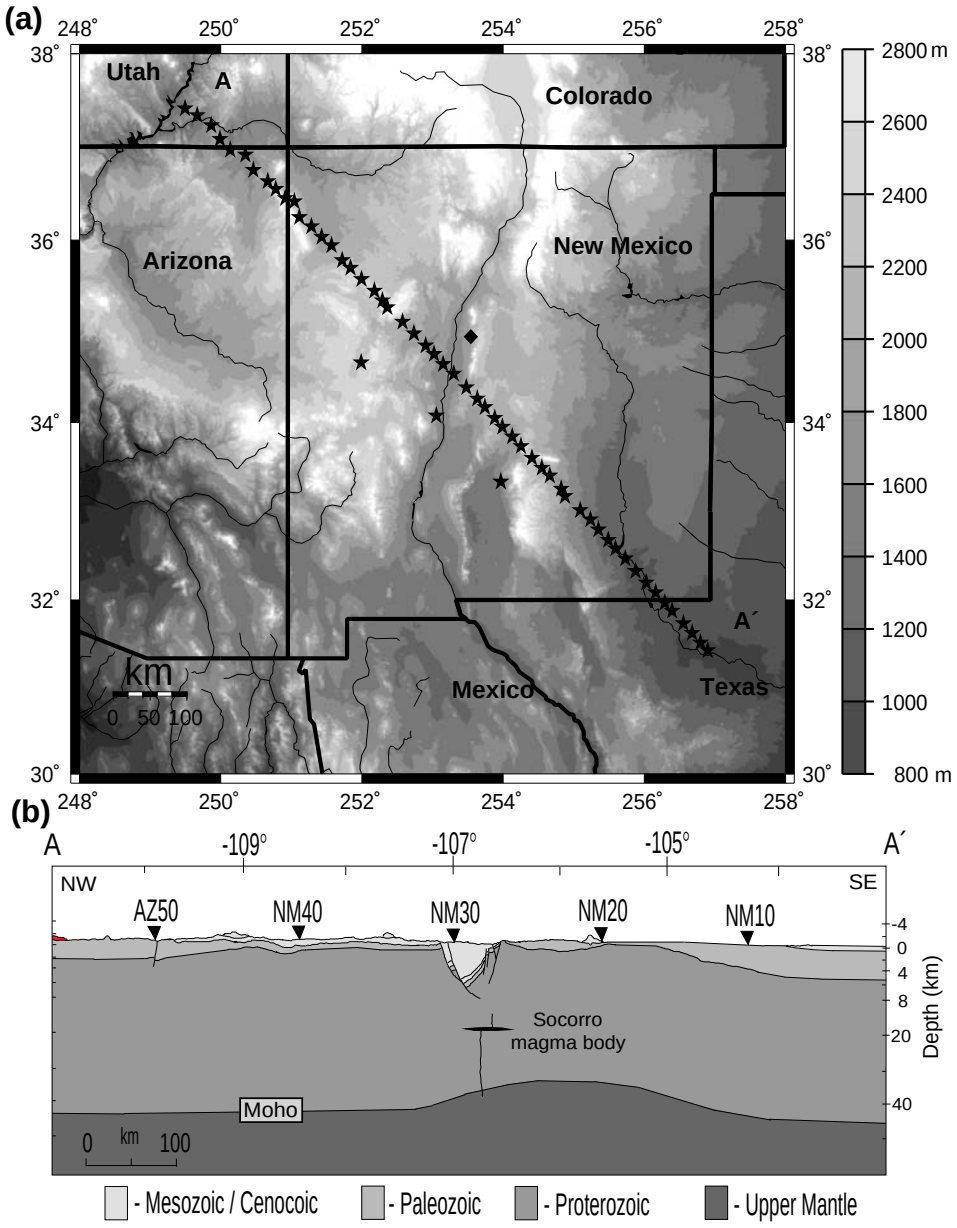

Figure 2.1: a) Topographic map with RISTRA station locations. Greyscale indicates elevation in meters. Stars show main transect station locations and the diamond shows the location of the Global Seismic Network borehole station ANMO. b) Geological cross-section along the RISTRA main transect.

tered no significant problems in obtaining permission for an extensive passive seismic experiment with a duration of about 18 months.

All sites were configured with Streckeisen STS-2 (120 s) seismometers and a sampling rate of 20 samples/sec. Three off-line stations deployed parallel to and southwest of the main network (Figure 2.1a) are not considered in this study. RefTek 24-bit recording systems (72A-07 and 72A-08) were used at all sites. There were two types of seismometer vault construction which we found to be approximately equally good in terms of noise and other characteristics. Most vaults in the southern part of the network were constructed from plywood with 2.5 cm thick polystyrene insulation, while vaults at sites northwest of the Rio Grande rift used medical styrofoam containers with 10 cm thick walls. Seismometers were mounted on 10 cm thick pre-mix concrete pads with a diameter of approximately 0.3 m. Up to 0.4 m of dirt was mounded on top of each vault to provide further insulation and thermal mass. Local power supplies consisted of two 30 W solar panels and approximately 110 A-hrs of lead-acid battery capacity.

2.3 Noise Power Spectral Density Estimation

Median noise acceleration power spectral density (PSD) estimates between 0.01 and approximately 8.5 Hz (the approximate onset of the antialiasing filter transition band) were calculated for each component of each RISTRA station using 1-hour data windows between August, 1999 and November, 2000. Times between data windows ranged from about 1 to approximately 5 weeks. Preliminary determinations of epicenters reported by NEIC were referred to in selecting each data window to avoid earthquake signals according to: (1)

no earthquakes with Mb $\geq$ 6.0 reported in the preceding 24 hrs; (2) no earthquakes with Mb $\geq$ 5.0 reported with $\Delta \leq 70^{\circ}$ in the preceding 24 hrs; (3) no earthquakes with Mb $\geq$ 4.0 reported for $\Delta \leq 20^{\circ}$ in the previous 12 hrs; (4) no earthquakes with Mb $\geq$ 3.0 reported for $\Delta \leq 15^{\circ}$ in the previous 3 hrs. Mid-night (between 23:00 and 00:00 local time) and mid-day (between 11:00 and 12:00 local time) periods which met the above criteria were sampled from each month of data collected between August, 1999 and November, 2000. All prospective data windows were visually inspected to ensure that obvious signals from local microearthquakes or other obvious cultural contaminants (e.g., mining explosions) were excluded. An identical selection procedure was performed for data recorded at ANMO, a 100-m borehole IRIS/USGS Global Seismic Network (GSN) station incorporating a Teledyne Geotech 54100 3-component seismometer. ANMO is located approximately 55 km from the midpoint of the RISTRA line (Harold Bolton, pers. commun.; Figure 2.1a).

Noise PSD estimates for all data windows were obtained for each component of each station using Welch's (Welch, 1967) averaging method with a Hanning taper and 18 375-s windows with 50% overlap. A median PSD was then calculated at each frequency for each component of each station. Overall median PSD estimates calculated for the entire RISTRA network and for ANMO are shown in Figure 2.2. The ratio of background noise for each station compared to the network median is shown in Figure 2.3. The spatial autocorrelation of the data in Figure 2.3 is shown in Figure 2.4. Differences between mid-day and mid-night median noise levels were calculated for the network median (Figure 2.5a), for ANMO (Figure 2.5b), and for individual RISTRA stations (Figure 2.5c).

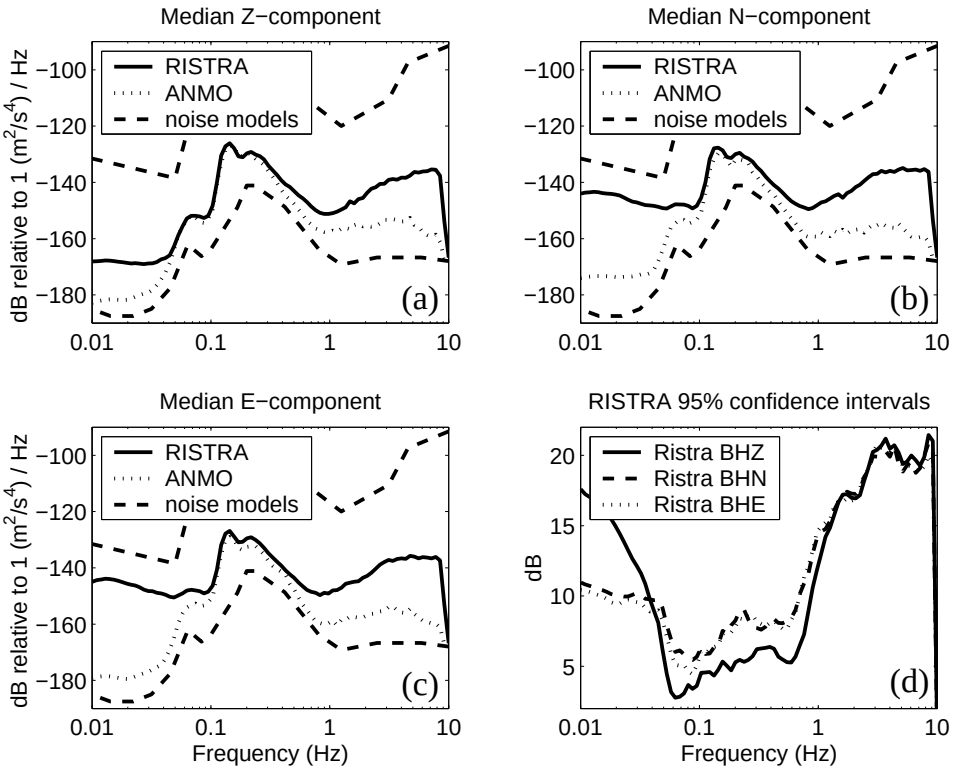

Figure 2.2: a,b,c) Median seismic noise levels. Solid lines show RISTRA network median levels for each component; dotted lines show estimates for ANMO. The dashed lines are the USGS high and low noise models of Peterson (1993). d) Symmetric 95% variation intervals (1.96 x standard deviation) on the RISTRA median seismic noise levels of (a-c).

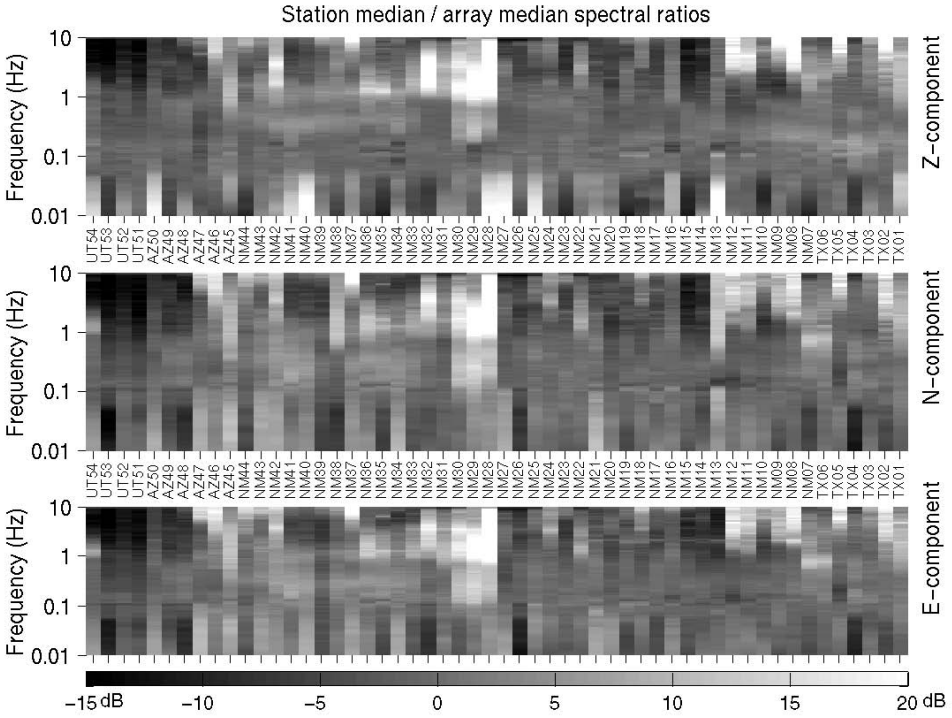

Figure 2.3: RISTRA station-by-station median noise levels, relative to network median PSD levels shown in Figure 2.2a-c. Maximal deviations from network median PSD level are approximately (+20 dB, -15 dB), as indicated by the greyscale.

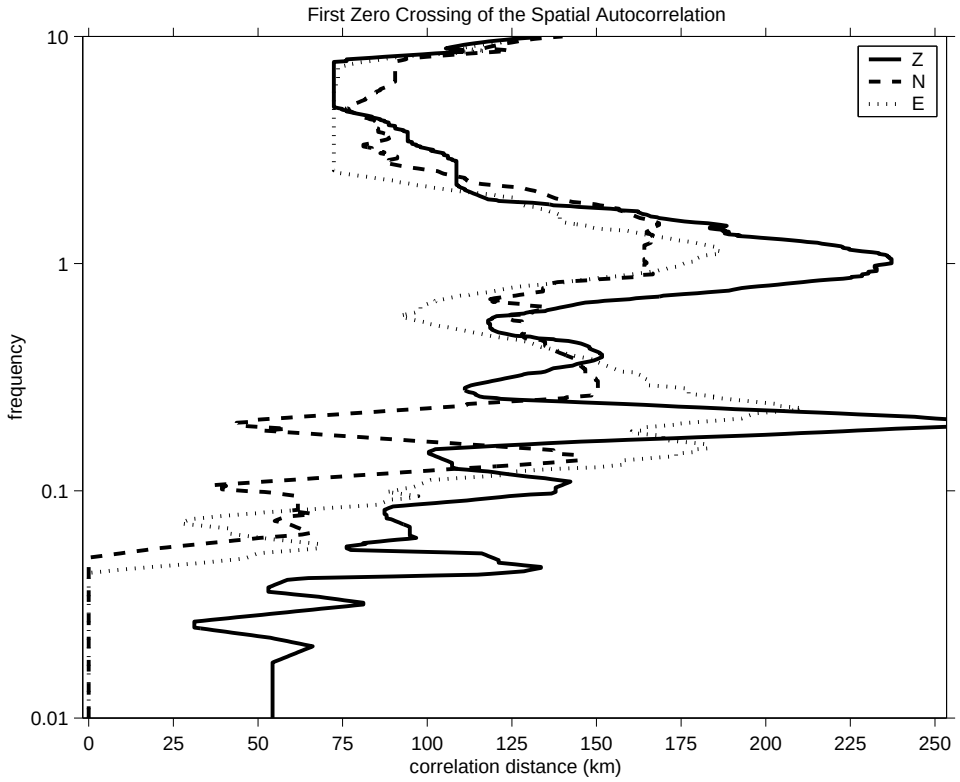

Figure 2.4: Spatial autocorrelation of the noise levels of Figure 2.3 (first zero crossing of the autocorrelation function).

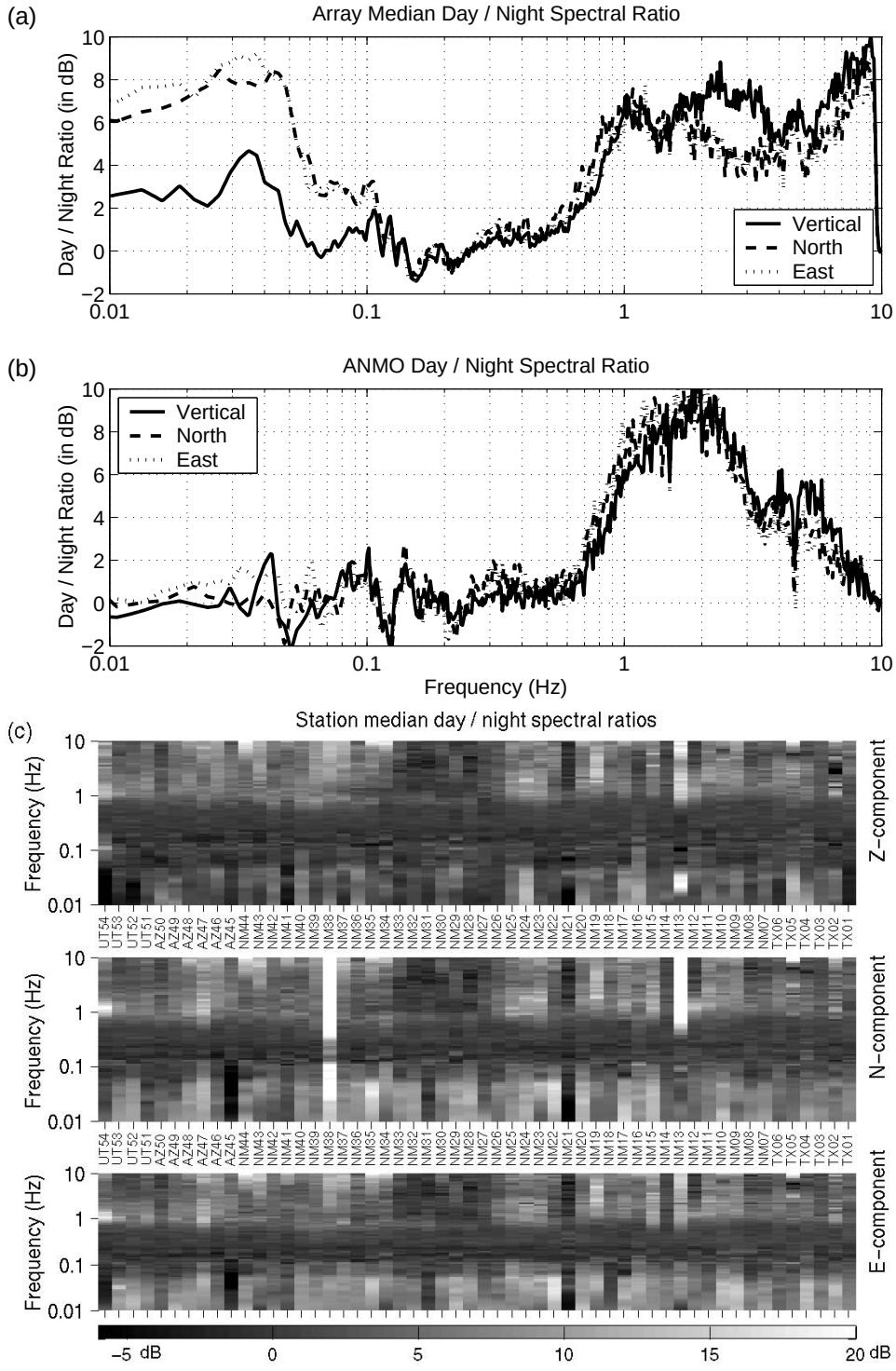

Figure 2.5: Mid-day versus mid-night noise differences for RISTRA stations (a) and ANMO (b). c) Individual station median mid-day versus mid-night differences.

2.4 Results and Discussion

At long periods (0.01 to 0.06 Hz) RISTRA vertical component median noise levels were approximately 10 to 12 dB above ANMO, and 17 dB above the USGS low noise model of Peterson (1993) (Figure 2.2a-c), with 95% variation limits (1.96 x standard deviation) ranging up to approximately 10 dB for horizontal and 17 dB for vertical components (Figure 2.2d). The higher variation limits for the vertical component are due to some sites having a very quiet vertical component (Figure 2.3) so that more variation is seen across the network than on the horizontal components which are uniformly noisier. The noise environment is highly anisotropic in that the horizontal components are much noisier at long periods, 25 to 30 dB higher than ANMO, and 40 dB higher than the USGS low noise model. This is due to the sensitivity of surface-mounted broadband seismometers to local tilt caused by thermal and/or barometric effects, and has been ubiquitously observed in non-borehole broadband sites, even examples located in tunnels (e.g., Given and Fels, 1993). Site testing at the USGS Albuquerque Seismological Laboratory has shown that even a shallow borehole installation (a few m) is capable of greatly reducing this effect (H. Bolton, pers. commun.). Long period background noise levels also show considerable (up to 15 dB) variation across the network (Figure 2.3), further demonstrating the local aspect of this component of the noise environment. Such local variation is reflective of surface site conditions, and systematic tests to further illuminate this local noise process should consider differences in slope, diurnal shading conditions, soil type, and moisture content as well as vault design. Removing the barometric pressure signal and/or vault temperature from seismic data has been shown to lower background noise levels

by up to 20 dB between 0.001 and 0.03 Hz (Beauduin, 1996; Zurn and Widmer, 1995), this suggests that a similar noise/barometric correlation/removal process might be useful for PASSCAL-style vaults; perhaps also incorporating temperature fluctuations. To our knowledge, this has not been done for typical shallow vaults, although it has shown great promise in ocean bottom seismographs (e.g., Crawford and Webb, 2000).

At microseismic frequencies (0.06 to 0.3 Hz), RISTRA network median noise is 5 to 20 dB above the USGS low noise model (Figure 2.2a-c), and is essentially indistinguishable from ANMO. 95% variation intervals in the microseismic band span a range up to approximately 7 dB (Figure 2.2d).

At high frequencies (0.3 to 8.5 Hz), RISTRA noise levels are approximately 30 dB above the USGS low noise model, and approximately 15 dB above ANMO noise levels (Figure 2.2a-c). Predictably, stations most isolated from cultural activity, e.g. AZ50-UT54 on the Colorado Plateau (Figure 2.3), are the quietest sites at high frequencies. The noisiest stations in this frequency band are those in the densely populated and major transportation corridor along the deep sedimentary basin of the Rio Grande rift valley (NM28-NM30), and those unavoidably deployed near oil and gas production in southeast New Mexico and west Texas (NM12 - TX01). Rift stations are up to 20 dB noisier in the high frequency band than the network median. 95% variation limits span a range of approximately 18 dB at high frequencies (Figure 2.2d).

To further characterize the local versus regional aspects typical of the RISTRA noise environment, we examined the spatial autocorrelation of the station median to network median levels of Figure 2.3. Figure 2.4 shows the

distance to the first zero crossing of the autocorrelation function for each component. Long period noise ($\leq$ 0.1 Hz) exhibits no significant spatial correlation (Figure 2.4) along the network at the station spacing resolution of about 18 km, confirming that this component of the noise environment is effectively local. At microseismic frequencies (0.06 to 0.3 Hz) background noise correlates up to approximately 250 km (thirteen stations) on the vertical component, and 175 km on the horizontal components. At high frequencies (0.3 to 8.5 Hz) vertical component noise levels correlate up to 225 km and horizontal component background noise correlates up to 175 km. We attribute the spatial correlation of high frequency noise levels with regional weather patterns and extended regions of cultural noise along the network, especially those of the high population, high-noise, Rio Grande rift and producing oil and gas fields of southwestern New Mexico and west Texas (Figure 2.3).

We also examined the spatial noise level autocorrelation of several synchronous time windows across the network. At microseismic frequencies (0.06 to 0.3 Hz) synchronous time windows showed similar results to the autocorrelation of station median spectra (Figure 2.4). However, at high frequencies synchronous time window autocorrelations were highly variable, some roughly matching the correlation lengths of Figure 2.4, others having no significant spatial correlation. This is most likely because the high frequencies are dominated by weather generated noise and cultural noise which can be highly variable from day to day, either being local or regional depending on wind and other factors. At long periods we observed negligible noise level correlation for the synchronous time windows, similar to the station median spectra (Figure 2.4).

Comparing median mid-day and mid-night noise levels (Figure 2.5a, c), we note that at long periods (0.1 to 0.06 Hz), RISTRA vertical component mid-day noise levels are only approximately 2 dB above night levels, while the observed increase for the horizontal components is in excess of 7 dB. Increases in daytime long period horizontal component noise have been noted previously at surface stations (e.g., Butler and Hutt, 1992) and attributed to diurnal variations of wind, barometric pressure, and temperature. Comparison with ANMO noise levels (Figure 2.5b) from the same period shows the clear superiority of the borehole installation in reducing diurnally varying long-period noise levels.

In the microseismic band (0.06 to 0.3 Hz) there are no day/night variations in excess of about 1 dB at either RISTRA or ANMO sites.

At high frequencies (0.3 to 8.5 Hz), we observe an average increase of up to 8 dB in mid-day vs. mid-night noise levels. The performance below 1 Hz is comparable to ANMO, but ANMO shows significantly better performances at higher frequencies. Both RISTRA and ANMO show a mid-day/mid-night increase in vertical versus horizontal noise between about 2 and 5 Hz. The greatest diurnal increases in RISTRA high frequency noise are seen above approximately 5 Hz. While the rift stations, NM28-NM30, are the noisiest at high frequencies (Figure 2.3), they do not exhibit strong day to night noise ratios (Figure 2.5c); evidently the high-frequency cultural noise sources are not significantly linked to the workday cycle, and may be linked to more continuous pipeline and regional rail activity.

2.5 Conclusions

Long period (0.01 to 0.06 Hz) typical (median) noise levels at these shallow broadband sites are controlled by very local site conditions (as exhibited by a negligible spatial correlation) and are typically 10 to 12 dB (vertical) and 25 to 35 dB (horizontals) higher than the highest quality site that is likely achievable in this region (the ANMO GSN borehole station). The horizontal long-period noise environment shows an increase in excess of 7 dB during mid-day relative to mid-night, not observed at ANMO, that we conclude is driven by temperature and/or other atmospheric effects interacting with the vault geometry and/or soil conditions to produce slab tilt. We note that this long-period noise is conceivably partially removable at the longest periods through the application of temperature or barometric correlations, and that this possibility should be tested for general application in PASSCAL-style deployments.

RISTRA microseism (0.06 to 0.3 Hz) noise shows comparable noise levels to ANMO, with negligible mid-day/mid-night variations, and significant correlation out to approximately 250 km, indicating both regional and local aspects to this noise band.

High frequency (0.3 to 8.5 Hz) median noise levels are controlled by proximity to local cultural noise sources, particularly the relatively developed Rio Grande rift south of Albuquerque and the oil and natural gas producing regions of southeastern New Mexico and west Texas. The lowest noise levels are correspondingly observed at the most culturally remote sites on the Colorado Plateau. Mid-day versus mid-night typical noise ratios at high frequencies were not always correlated with absolute noise levels. Sites within the relatively

noisy Rio Grande rift, for example, were equally noisy even during mid-night periods. Because of the extended nature of the principal high-frequency noise regions in this network (the Rio Grande rift and the southwestern oil and gas fields), high frequency noise levels also display a general correlation out to approximately 225 km, but correlations during synchronous time periods do not always show this effect.

We conclude that the most likely prospect for significantly improving the broadband noise environment in shallow portable broadband deployments below about .1 Hz lies in a more detailed understanding of the local long-period noise environment. This is especially notable for horizontal components, where key details include improved understanding of how slab tilt effects are related to thermal, atmospheric pressure, and ground effects interacting with vault design and near-surface site geology.

Acknowledgments

The RISTRA team especially thanks the PASSCAL Instrument Center at New Mexico Tech for planning and data processing assistance. We also thank the dozens of private landowners, the New Mexico State Land Office, the United States Forest Service, the United States Bureau of Land Management, the United States Fish and Wildlife Service, the Southern Utah Wilderness Alliance, Isleta Pueblo, Laguna Pueblo, and the Navajo Nation for assistance in the permitting the siting of these instruments. Persons wishing to conduct geological investigations on the Navajo Nation must first apply for and receive a permit from the Navajo Nation Minerals Department, PO Box 1910,

Window Rock, Arizona, 86515, 928-871-6587. This study was supported by NSF grant EAR 9707190 and EAR 9706094. We also thank Los Alamos National Laboratory IGPP and the NMSU Arts and Sciences Research Center for their support. Essential field assistance was provided by Eric Matzel, Richard Rapine, Frederik Tilmann, Wei-Chuang Huang, Al Blackhorse, Anca Rosca, Laurecita Luna, and Dueker's Diggers. The comments of Bob Hutt, Harold Bolton and an anonymous reviewer were incorporated in the final version.

References

Baldridge, W.S., G.R. Keller, V. Haak, E. Wendlandt, G.R. Jiracek, and K.H. Olsen, The Rio Grande Rift, from Olsen, K.H., ed., *Continental Rifts: Evolution, Structure, Tectonics, Developments in Geotectonics, 25,* Elsevier, 233-273, 1995.

Beauduin, P., P. Lognonne, J. Montagner, S. Cacho, J. Karczewski, M. Morand, The effects of atmospheric pressure changes on seismic signals, or how to improve the quality of a station, *Bull. Seism. Soc. Am., 86,* 1760-1799, 1996.

Butler, R. and C.R. Hutt, Seismic noise on Rarotonga: surface versus downhole, *EOS Trans. Am. Geophys. Union., 73,* 548-549, 1992.

Crawford, W., and S. Webb, Identifying and removing tilt noise from low-frequency (< 0.1 Hz) seafloor vertical seismic data, *Bull. Seism. Soc. Am., 90,* 952-963, 2000.

Given, H. K., Variations in broadband seismic noise at IRIS/IDA stations in the USSR with implications for event detection, *Bull. Seism. Soc. Am. 80,* 2072-2088, 1990.

Given, H. K., F. Fels, Site characteristics and ambient ground noise at IRIS IDA stations AAK (Ala-Archa, Kyrgyzstan) and LY (Talaya, Russia), *Bull. Seism. Soc. Am., 83,* 945-953, 1993.

Gurrola, H., J. B. Minster, H. Given, F. Vernon, J. Berger, and R. Aster, Analysis of high frequency seismic noise in the western United States and

eastern Kazakhstan, *Bull. Seism. Soc. Am., 80,* 951-970, 1990.

Henyey, T., EarthScope: A look into our continent, *Geotimes, 45,* 5-7, 2000.

Kennett, B. and van der Hilst, R., Using a synthetic continental array to study the earth's interior, *Journal Phys. Earth., 44,* 669-674, 1996.

Peterson, J., Observations and modeling of seismic background noise, *Open-File Report 93-322,* U.S. Department of Interior Geological Survey, 1993.

Rodgers, P. W., S. R. Taylor, and K. K. Nakanishi, System and site noise in the regional seismic test network from 0.1 to 20 Hz, *Bull. Seism. Soc. Am., 77,* 663-678, 1987.

Uhrhammer, R. A., Background Noise PSD Analysis of USNSN Broadband Data for 1998, *Berkeley Seismological Laboratory report,* 22 pp., 2000.

Vila, J., The broadband seismic station CAD (Tunel del Cadi, eastern Pyrenees): Site characteristics and background noise, *Bull. Seism. Soc. Am. 88,* 297-303, 1998.

Welch, P., The use of Fast Fourier Transform for the estimation of power spectra: a method based on time averaging over short, modified periodograms, *IEEE Trans. Audio Electroacoustics, AU15,* 70-73, 1967.

Withers, M. M., R. C. Aster, C. J. Young, and E.P. Chael, High frequency analysis of seismic background noise as a function of wind speed and shallow depth, *Bull. Seism. Soc. Am., 86,* 1507-1515, 1996.

Young, C. J., E. P. Chael, M. M. Withers, and R. C. Aster, A comparison of high frequency ($\geq$1 Hz) surface and subsurface noise environment at three sites in the United States, *Bull. Seism. Soc. Am., 86,* 1516-1528, 1996.

Zurn, W, and R. Widmer, On noise-reduction in vertical seismic records below 2 mHz using local barometric-pressure, *Geop. Res. Lett., 22,* 3537-3540, 1995.

CHAPTER 3

Receiver Function Estimation and Imaging Methods

[1]A modified version of this chapter will be submitted to *Journal of Geophysical Research*, Wilson, D., R. Aster, J. Ni, S. Grand, M. West, W. Gao, W.S. Baldridge, and S. Semken, Imaging the Seismic Structure of the Crust and Upper Mantle Using Receiver Functions, Part 1: Methods, in preparation, JGR, 2004

Abstract

Receiver functions provide a valuable tool for producing images of the crust and upper mantle from teleseismic earthquake arrivals. However, image quality can be compromised by instabilities in the process of receiver function estimation, as well as irregular station spacing and uneven data coverage. We present the foundations for receiver function estimation and prestack migration techniques which reduce receiver function deconvolution instability and produce regularized, multi-phase receiver function images. The receiver function estimation technique builds on frequency-wavenumber filtering methods by transforming receiver function amplitudes into the frequency-pseudo-wavenumber domain. We then filter receiver function amplitudes that have a high degree of variability as a function of horizontal slowness (epicentral distance) while preserving receiver function phases that have consistent moveout characteristics. We apply this method to synthetic receiver functions and show excellent recovery of receiver function phases in the presence of high noise. We present a method of receiver function migration based on regularized Kirchhoff migration that migrates both direct and reverberated P-to-S converted phases to their true subsurface position to produce an image of the velocity discontinuity structure of the subsurface. We apply this migration technique to synthetic receiver functions to demonstrate that it is especially well suited to irregularly spaced stations and uneven data coverage. An important aspect of both the deconvolution and migration techniques is that they do not require the recording of a single earthquake at multiple stations, making them especially applicable to temporary arrays which may have irregular recording times between stations and allow the incorporation of previous teleseismic data.

3.1 Introduction

As earthquake body waves waves travel through the Earth they produce a series of reflections, refractions, and conversions (e.g., from compressional to shear waves) at every boundary between regions of differing elasticity and/or density. Radial receiver function analysis isolates P-to-S converted phases at these interfaces through a cross-component signal deconvolution of the horizontal component seismograms by the vertical component (Langston, 1977; Ammon, 1991; Cassidy, 1992). In receiver function analysis the vertical seismogram is characterized as a convolution of the instrument response, vertical site response, propagation effects, and an earthquake's source function. The radial seismogram is characterized as the convolution of the radial site response with the same instrument response, propagation effects, and source function. The deconvolution then removes the common features from the radial seismogram, leaving a source-equalized "receiver function" which is only a function of the near-surface (upper mantle and crust) site response. This source equalization allows for direct comparison of teleseismic recordings which may have had very different source-time functions.

An inherent problem in calculating receiver functions is the stability of the deconvolution which may be compromised by high noise levels or holes in the vertical component spectrum. In this paper we develop receiver function estimation techniques which take advantage of the characteristic moveout of receiver phases to enhance receiver function phases and filter out energy caused by noise and deconvolution instability.

Receiver functions were first applied to solitary stations to obtain

a local, 1-dimensional estimate of structure (e.g., Langston, 1977). Receiver functions at a single station can be moveout corrected to a reference epicentral distance, to vertical travel time, or to a common depth axis, then stacked. As the number of stations in portable seismic arrays has increased, the receiver function technique has been used to create 2-dimensional images of fundamental structures such as the Moho or upper mantle transition zone discontinuities (e.g., Sheehan et al., 1995; Yuan et al., 1997; Li et al., 2002). A commonly used method of producing receiver function 2-D depth cross sections is by using the exploration seismic analog of the common conversion point (CCP) image (Tessmer and Behle, 1988; Dueker and Sheehan, 1998). The CCP image is created by first back-projecting the recorded signal along the theoretical ray path, and then binning the data into lateral and depth bins. The depth cross section is then calculated by taking the mean sample value (or some other central tendency measure) in each bin. Although this imaging method does transform the data into offset and depth space, it does not correct for diffracted energy, so that if significant lateral heterogeneity is present the resulting image will not be an accurate depiction of true earth structure.

If the Earth's velocity structure is laterally heterogeneous, the incoming wavefield will be diffracted so that the recorded wavefield is a distorted version of the subsurface structure. Migration is required to produce a subsurface structural image from the recorded data (Abers, 1998; Eaton, 2002). Migration of seismic data moves recorded phases to their true subsurface position (either in time or in depth) and collapses diffracted energy. Recently, researchers have begun to apply seismic data migration techniques to teleseismic wavefields, including both prestack (Sheehan et al., 2000; Poppliers and

Pavlis, 2003a,b) and poststack (Ryberg and Weber, 2000) migration of receiver functions, as well as methods of prestack migration/inversion of the full three component teleseismic wavefield (e.g., Bostock and Rondenay, 1999; Bostock et al., 2001; Fan et al., 2003; Shragge and Artman, 2003).

Here we present a method of receiver function migration that migrates both direct and reverberated P-to-S converted phases to their true subsurface position. The migrated image is constructed using receiver functions calculated at each station independently, making it unnecessary to simultaneously record the teleseismic wavefield from a single earthquake at multiple stations. Migration with receiver functions rather than the full three component wavefield reduces a vector imaging problem to a scalar imaging problem (e.g., Levander, 2003), and allows us to use seismic data migration methods based on the simpler acoustic approximation to the seismic wave equation, rather than fully elastic methods. We develop a receiver function migration methodology based on regularized Kirchhoff migration (Duquet et al., 2000; Nemeth et al., 1999) which has been shown to produce subsurface images with higher resolution and fewer migration artifacts and acquisition geometry artifacts than standard migration algorithms. We develop and apply this migration technique to synthetic receiver functions to demonstrate the benefits of applying this technique to recording geometries where imaging can be degraded by irregular station spacing and uneven data coverage. In Chapter 4 we apply the receiver function estimation and migration methods developed here to data from the LA RISTRA network.

3.2 Receiver Function Estimation

Receiver functions are computed by the deconvolution of the horizontal component seismograms by the vertical component either in the time domain (e.g., Sheehan et al., 1995; Zandt et al., 1995; Poppliers and Pavlis, 2003a,b) or frequency domain (e.g., Ammon, 1991; Cassidy, 1992; Duker and Sheehan, 1998). It is important to note that although the time scale of receiver functions is determined by the phase lag times in the deconvolution, we can still use the ray nomenclature used to describe arrivals on typical seismograms because the receiver function can be thought of as a scaled version of the radial component of displacement with P multiples removed (Ammon, 1991). For a typical receiver function, four dominant converted/refracted modes of ray propagation are commonly observed (Figure 3.1a): 1) Direct P , observed as a prominent pulse near zero time. The deconvolution process should place this pulse exactly at zero time, however shallow structure such as sedimentary layers can cause a slight delay, typically less than 1 second, as well as a decrease in amplitude of the direct P pulse (Cassidy, 1992). 2) Direct P-to-S (Ps) generated at each discontinuity. Assuming a flat layered velocity geometry, the travel time for the Ps phase is given by

$$T_{Ps} = T_s - T_p \tag{3.1}$$

where

$$T_s = H(Vs^{-2} - p^2)^{1/2}, \qquad T_p = H(Vp^{-2} - p^2)^{1/2}, \tag{3.2}$$

H is the depth to the converting interface, Vp and Vs are the average P-wave and S-wave velocity to the converting interface, and p is the horizontal slowness

(ray parameter) of the teleseismic event. For conversions from the Moho, the Ps phase typically arrives at a delay time of 4-6 sec. 3) The $PpPs$ phase resulting from incoming P refracting as P at a discontinuity, reflecting downward as P off the earth's free surface, then converting/reflecting upwards as S at each discontinuity. The travel time for the $PpPs$ phase is given by

$$T_{PpPs} = T_s + T_p, \tag{3.3}$$

and typically occurs around 15-20 seconds for the Moho. 4) The (simultaneously arriving) $PpSs$ and $PsPs$ phase resulting from incoming P, refracting/converting as P or S at a discontinuity, reflecting downward as P or S, off the earth's free surface, and finally reflecting upwards as S at each discontinuity. The travel time for the $PpSs$+$PsPs$ phase is given by

$$T_{(PpSs+PsPs)} = 2T_s, \tag{3.4}$$

and typically occurs a few seconds after the $PpPs$ phase for the Moho. Since this phase propagates along two simultaneously arriving ray paths, it is especially sensitive to lateral velocity heterogeneity which can decrease amplitude or produce a double arrival.

An inherent problem in calculating receiver functions is the stability of the deconvolution which may be compromised by high noise levels or holes in the vertical component spectrum. A common regularization technique used to stabilize the deconvolution is water-level deconvolution (Clayton and Wiggins, 1976; Ammon, 1991) which sets a lower bound on the value of the denominator (the vertical seismogram spectra) in the frequency-domain

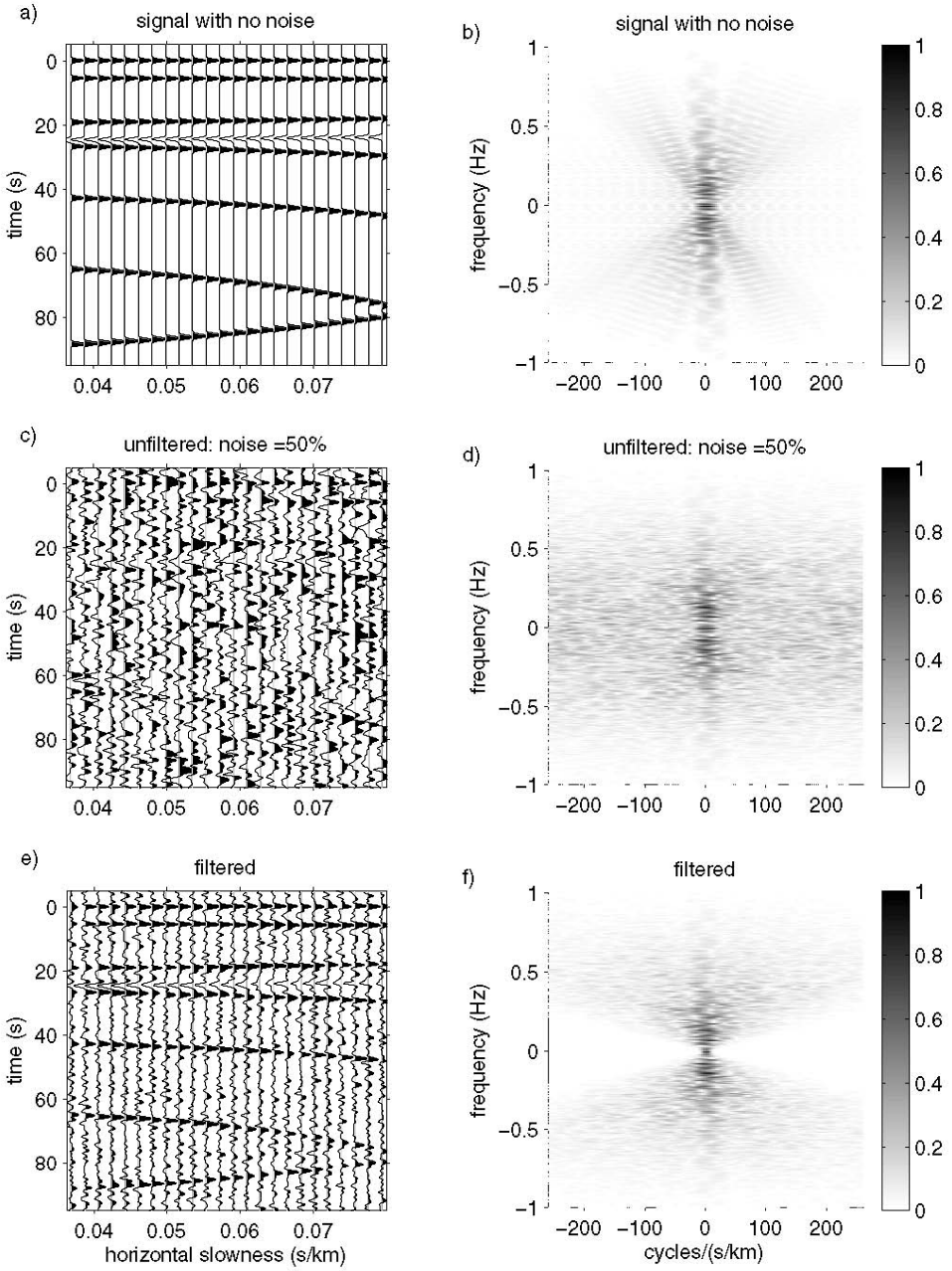

Figure 3.1: a) Predicted travel times for receiver function phases as a function of horizontal slowness (epicentral distance). b) Receiver function phases transformed to frequency-pseudowavenumber ($f-k$) space. c) Receiver function phases in the time domain with noise added; d) $f-k$ domain with noise added; e) time domain filtered; f) $f-k$ domain filtered. The added noise has a standard deviation of 1/2 the maximum receiver function amplitude.

spectral division. To further combat this instability we implement a variation of frequency-wavenumber filtering which takes advantage of the moveout times predicted by equations 3.1-3.4. We do this by first transforming receiver functions calculated by waterlevel deconvolution at a single station from time-slowness $(t-p)$ domain to the frequency-pseudo-wavenumber $(f-k)$ domain using the 2-dimensional Fourier transform (e.g. Bracewell, 2000), given by

$$U(f,k) = \int\int u(t,p)e^{(i2\pi kp - i2\pi ft)}dpdt. \tag{3.5}$$

Note that we use the variable k to represent pseudo-wavenumber which has units of cycles/slowness, or cycles/(s/km), in contrast to the traditional usage of k to represent wavenumber (cycles/km). The advantage in transforming to the $f-k$ domain is that the location to which energy is mapped in the $f-k$ domain is determined by the phase time moveout in the $t-p$ domain, allowing discrimination among phase moveout characteristics. A receiver function phase which has the linear moveout of dt/dp and frequency f is mapped to pseudo-wavenumber $k = f\cdot\ d\mathrm{t}/dp$ at frequency f. Thus, receiver function phases which have a positive moveout as a function of p, such as predicted for Tps phases (equation 3.1), will be mapped to positive k, and receiver function phases which have a negative moveout as a function of p, such as predicted for $PpPs$ and $PpSs{+}PsPs$ phases (equation 3.3 and 3.4), will be mapped to negative k. Figure 3.2 shows the predicted mapping to the $f-k$ domain predicted for various phases predicted from equations 3.1-3.4.

In the $f-k$ domain, receiver function amplitudes which have large magnitude k represent amplitudes which have a high degree of variability as a function of p. This could be due to either phases with very large time moveout

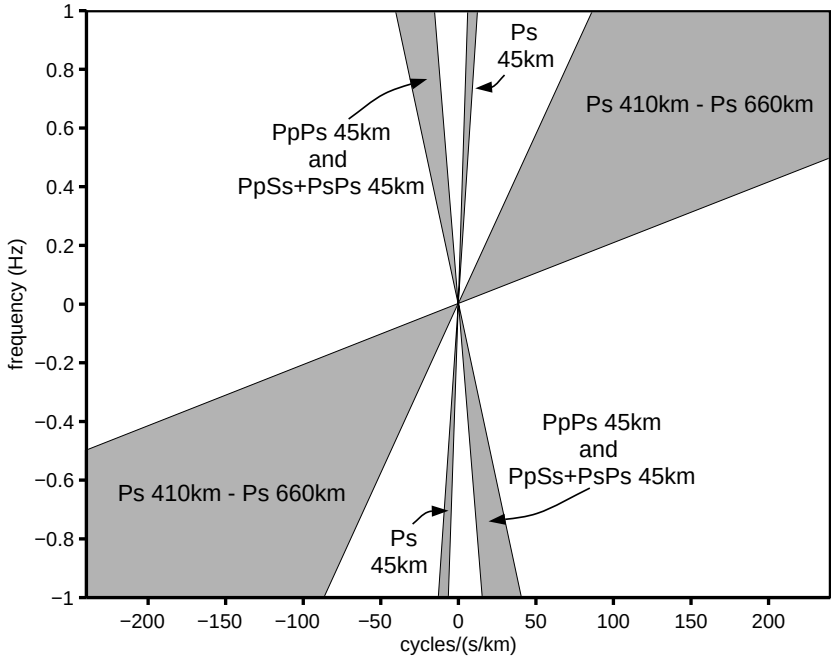

Figure 3.2: Predicted mapping to $f - k$ space of receiver function phases.

(dt/dp), or to receiver function spikes which do not appear on adjacent receiver functions caused by either high background noise or instability in the receiver function deconvolution. By calculating the maximum predicted $d\mathrm{t}/dp$ from equations 3.1-3.4 we can calculate the maximum magnitude of k and design a filter to eliminate receiver function amplitudes that have a high degree of variability as a function of horizontal slowness (epicentral distance) while preserving receiver function phases which have consistent moveout characteristics.

Filtering of receiver function amplitudes is accomplished by multiplication in the $f-k$ domain by a Gaussian filter described by

$$F(f,k) = e^{\{-(2\pi k)^2./(4[3.75\alpha]^2)\}}, \tag{3.6}$$

where $\alpha = f\cdot \max(d\mathrm{t}/dp)$. The scaling of α by 3.75 results in approximate filter amplitudes of .1 when $k = 1.88\cdot f\cdot \max(d\mathrm{t}/dp)$, .5 when $k = f\cdot \max(d\mathrm{t}/dp)$, and .9 when $k = .375\cdot f\cdot \max(d\mathrm{t}/dp)$. We use a Gaussian shaped filter rather than a narrower filter targeted at specific phases to allow for deviations in predicted moveout times due to dipping or laterally heterogeneous velocity geometries. The filter applies the strongest downweighting to receiver function amplitudes that do not vary relatively smoothly as a function of p, thus characterizing these amplitudes as noise due to either high background noise or instability in the receiver function deconvolution.

Figure 3.1 is an illustration of the receiver function filtering process. Figure 3.1a shows receiver function amplitudes in $t-p$ domain as predicted by equations 3.1-3.4 using the TNA reference Earth velocity model (Grand and Helmberger, 1984), and Figure 3.1b shows the same receiver function amplitudes transformed to the $f-k$ domain. For display purposes, receiver function

phase amplitudes at all depths have been normalized to 1. In Figures 3.1c,d we have added noise that has a standard deviation of 1/2 the maximum receiver function amplitude. The effect of the added noise in the $t-p$ domain is quite dramatic, making it difficult to discern the lateral coherency of many of the receiver function phases. Since the added noise is random, or "white", in the $t-p$ domain, the noise appears in the $f-k$ domain (Figures 3.1d) as increased amplitudes across both the f and k spectra.

We design a filter by calculating the maximum predicted dt/dp from equations 3.1-3.4 using the TNA reference Earth velocity model. The maximum time moveout occurs for the Ps phase from the 660 km upper mantle discontinuity, giving $\max(dt/dp) = 520$ s/(s/km). Using this value in equation 3.6 we obtain a filter in the $f-k$ domain. The resulting filtered receiver function phases are shown in Figures 3.1e,f in the $t-p$ and $f-k$ domains respectively. There is evident improvement in the $t-p$ domain, with a significant increase in the lateral coherency of receiver function phases. The correlation coefficient between Figure 3.1a and 3.1c is 0.39 and the correlation coefficient between Figure 3.1a and 3.1e is 0.76, which is equal to a 95% increase in correlation coefficient for the filtered receiver functions.

3.3 Receiver Function Imaging

3.3.1 Migration

We present a method of receiver function migration that migrates both direct and reverberated P-to-S converted phases to their true subsurface position to produce an image of the velocity discontinuity structure of the subsurface. We cast the migration as a Kirchhoff-style prestack migration (Yil-

maz, 1987; Dellinger et al., 2000) by characterizing the model space as a grid of point scatterers. For each station we then ray trace recorded receiver function phases (direct converted phases as well as reverberated phases) from each station to possible scattering points within the model space. Receiver function amplitudes are scaled and summed onto the output migration grid according to the Kirchhoff integral, which relates the wavefield measured at the surface to the wavefield at depth. The far field portion of the Kirchhoff integral can be expressed as (Yilmaz, 1987)

$$U_{out}(x,z) = \frac{1}{2\pi} \int \left(\frac{\cos\theta}{vr} \frac{\partial}{\partial t} U_{in}(x_{in}, z=0, t) \right) dx, \tag{3.7}$$

where v is the rms velocity at the output point (x, z), r is the distance between the input $(x_{in}, z = 0)$ and the output (x, z) model points, and t is the source-to-model point travel time plus the receiver-to-model point travel time. The dependence on $cos\theta$, known as the obliquity factor, is due to the recording geometry. For vertical component P-wave migration, θ is the angle between vertical and the incidence angle of the ray being imaged. For receiver function migration, θ is the angle between the L component (the incidence angle of the specular raypath for a given event) and the incidence angle of the ray being imaged. The dependence on $\frac{1}{vr}$ is the spherical spreading term and the time derivative gives the phase shift required by Huygens' principle. In two dimensions the half derivative is used (multiplication by $(i\omega)^{1/2}$ in the frequency domain).

Seismic data migration can further be expressed as the linear operator (Green's function), $\mathbf{G}$, which maps the velocity discontinuity structure of the subsurface, $\mathbf{m}$, onto data which we record, $\mathbf{d}$. This gives the linear

relationship $\mathbf{d} = \mathbf{Gm}$. The $\mathbf{G}$ is constructed using the travel times and scaling relationships specified in equation 3.7. Seismic data migration algorithms produce approximate subsurface images from seismic data. In particular, the Kirchhoff migration operator gives a model estimate produced by the solution $\mathbf{m} = \mathbf{G}^T\mathbf{d}$ (Nemeth et al., 1999). Although migration algorithms do collapse diffracted energy and migrate reflections to their true subsurface positions, they also produce artifacts due to irregular sampling geometries (i.e., seismographs may not be evenly spaced) and uneven subsurface illumination due to velocity heterogeneities.

Regularized migration (Duquet et al., 2000; Nemeth et al., 1999) uses the regularized inverse of the forward modeling operator, $\mathbf{G}$, and gives a more accurate subsurface model by the solution $\mathbf{m} = \mathbf{G}^{-g}\mathbf{d}$. Regularized migration has been shown to produce subsurface images with higher resolution and fewer migration artifacts and acquisition geometry artifacts than standard migration algorithms (Duquet et al., 2000; Nemeth et al., 1999). However, it is not routinely used in the exploration industry (where large surveys often have over 10^6 data traces) due to the computing power needed to compute an inverse for $\mathbf{G}$. Passive teleseismic experiments such as RISTRA have on the order of 10^3 to 10^4 traces, making inversion techniques far more tractable. By setting up the migration as an inverse problem we can use regularization to decrease the sensitivity of our solution to noise. This is done by minimizing the following objective function (Nemeth et al., 1999):

$$p(\mathbf{m}) = ||\mathbf{Gm} - \mathbf{d}||^2 + \epsilon||\mathbf{Cm}||^2 \tag{3.8}$$

The first term after the equal sign is the data misfit function and the second

term is the regularization term. The $\mathbf{C}$ matrix is a conditioning matrix which can be used to minimize desired model properties and ϵ is a constant which weights the regularization. For example, to obtain a smooth model, the $\mathbf{C}$ matrix would contain the spatial derivatives of the model, and to minimize the model norm, the $\mathbf{C}$ matrix would be an identity matrix. We implement second order Tikhonov regularization so that $\mathbf{C}$ contains the second order spatial derivatives of the model. To determine the appropriate magnitude of ϵ, we compute the solution to equation 3.8 for a range of values of ϵ, and then construct a tradeoff curve to determine the magnitude of ϵ that gives the optimal tradeoff (corner value) between misfit ($||\mathbf{Gm} - \mathbf{d}||^2$) and model roughness ($||\mathbf{Cm}||^2$). We employ a conjugate gradient iterative scheme to obtain the solution since the $\mathbf{G}$ matrix can be an extremely large sparse matrix.

Travel times for each phase are calculated relative to the P-wave arrival at the recording station according to the raypaths shown in Figure 3.5. Travel time for the Ps phase is given by

$$t_{psmig} = t_{mod-sta} - T_p + (t_{src-Xp} - t_{src-sta}) \tag{3.9}$$

where $t_{mod-sta}$ is the travel time from the model point to the station, T_p is given by equation 3.2, t_{src-Xp} is the travel time from the epicenter to point Xp (Figure 3.5), and $t_{src-sta}$ is the travel time from the epicenter to the recording station. If we assume a flat-layered velocity geometry, such as in migrating synthetic data, we can calculate the quantity $(t_{src-Xp} - t_{src-sta})$ directly from the horizontal slowness without actually calculating the travel time from the epicenter. When using real data, we need to account for the curvature and velocity structure of the earth which causes the horizontal slowness to change

with increasing epicentral distance. In that case, we can calculate the quantity $(t_{src-Xp} - t_{src-sta})$ based on travel times predicted for a reference earth velocity as a function of epicentral distance. Since rays traveling from the epicenter to Xp, and from the epicenter to the recording station, have taken nearly the same path, the quantity $(t_{src-Xp} - t_{src-sta})$ is primarily a function of the distance between Xp and the station and the horizontal slowness at Xp and the station, and the choice of reference earth velocity does not have a large effect. Similarly, for the $PpPs$ migration, the travel time is given by

$$t_{ppmig} = t_{mod-sta} + T_p + (t_{src-Xp} - t_{src-sta}), \tag{3.10}$$

and for the $PpSs + PsPs$ migration

$$t_{ssmig} = t_{mod-sta} + T_s + (t_{src-Xs} - t_{src-sta}), \tag{3.11}$$

where t_{src-Xs} is the travel time from the epicenter to point Xs (Figure 3.5), and T_s is given by Equation 3.2. Sharp velocity contrasts at the Moho and deep sedimentary basins introduce large multiples into the images which can overprint deeper structure. To suppress such multiples the three phases are migrated onto three separate output grids which can then be stacked to suppress multiples arising from any single phase. The three output grids can also be analyzed independently; if the phases do not align correctly it is an indicator that the velocity model used for the migration is not correct.

Figure 3.4a-f shows migrated cross sections for a synthetic receiver function data set containing 20 stations with irregular station spacing of 20 ± 10 km. Each station has 4 receiver functions with random backazimuth in-line with the imaging plane (i.e., $\pm 180°$) and random epicentral distance between

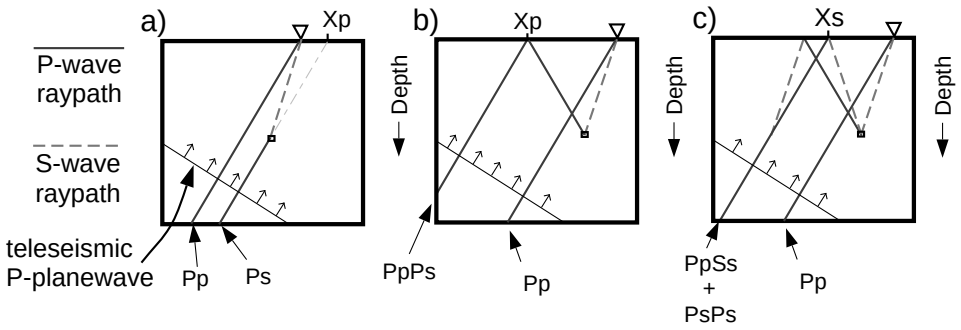

Figure 3.3: Raypaths for the a) Ps, b) PpPs, and c) PpSs + PsPs phases.

35° and 95°, which corresponds to a range in values of horizontal slowness (p) between .039 and .078 s/km. Synthetic receiver functions were calculated using a 45 km thick crust over a halfspace. Figure 3.4a,c,e shows Kirchhoff migrated cross sections ($\mathbf{m} = \mathbf{G}^T\mathbf{d}$) of the Ps, $PpPs$, and $PpSs + PsPs$ phases, and the corresponding regularized migration cross sections are shown in Figure 3.4b,d,f. For each phase the regularized migration shows improved lateral coherency of imaged receiver function amplitudes. In areas where there is a large gap between adjacent stations, the regularized migration attempts to create an image that is spatially continuous while fitting the data. The regularized migration also shows a reduction in migration artifacts, or "smiles", caused by sparse data coverage, which are most evident in the Ps migration (Figure 3.4a). The regularized migration is not simply smoothing the data, it is determining the optimal tradeoff between fitting the data and a smooth model. Areas with high data coverage will experience less smoothing, and areas with poor data coverage will be influenced more by adjacent data in an attempt to produce a spatially continuous migration.

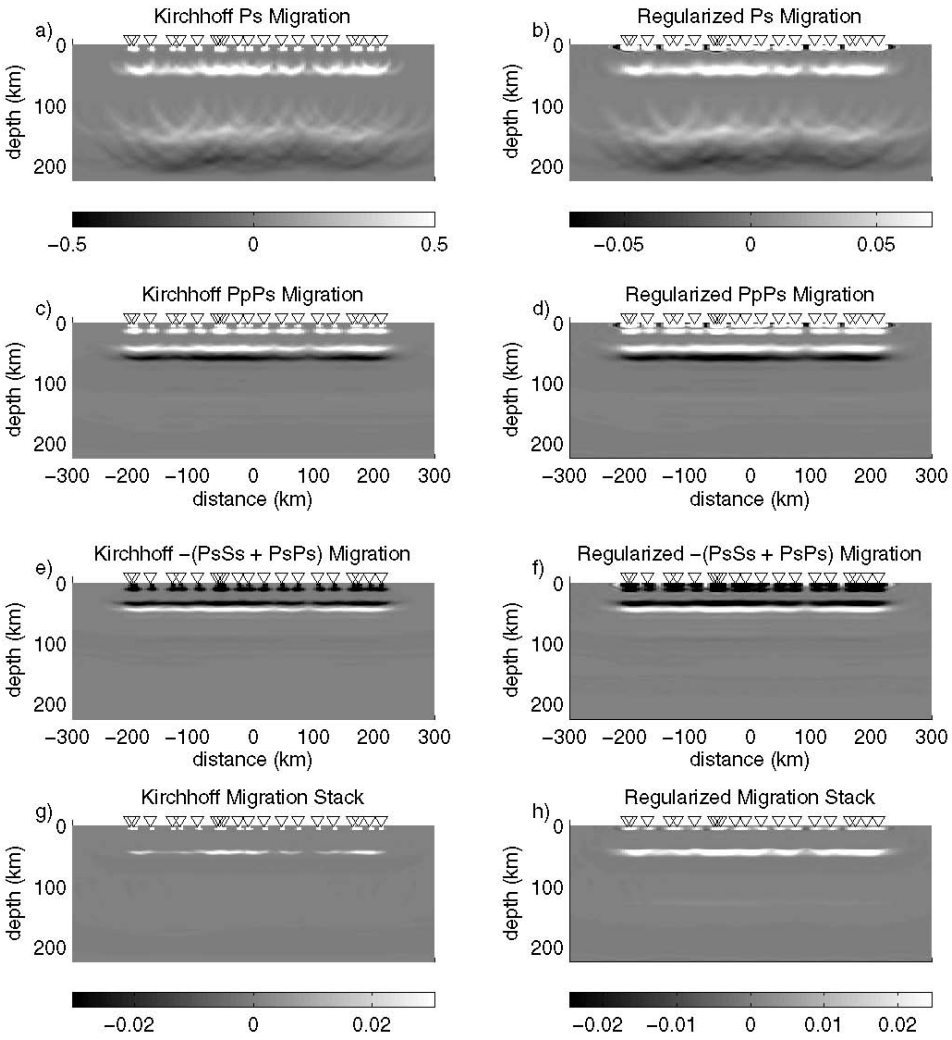

Figure 3.4: Kirchhoff migrated cross sections for the a) Ps, c) PpPs, and e) PpSs + PsPs phases, with the corresponding regularized migrated cross sections shown in b), d), and f). g) shows the stack of the Kirchoff migrated cross sections, and h) is the stack of the regularized migrated cross sections.

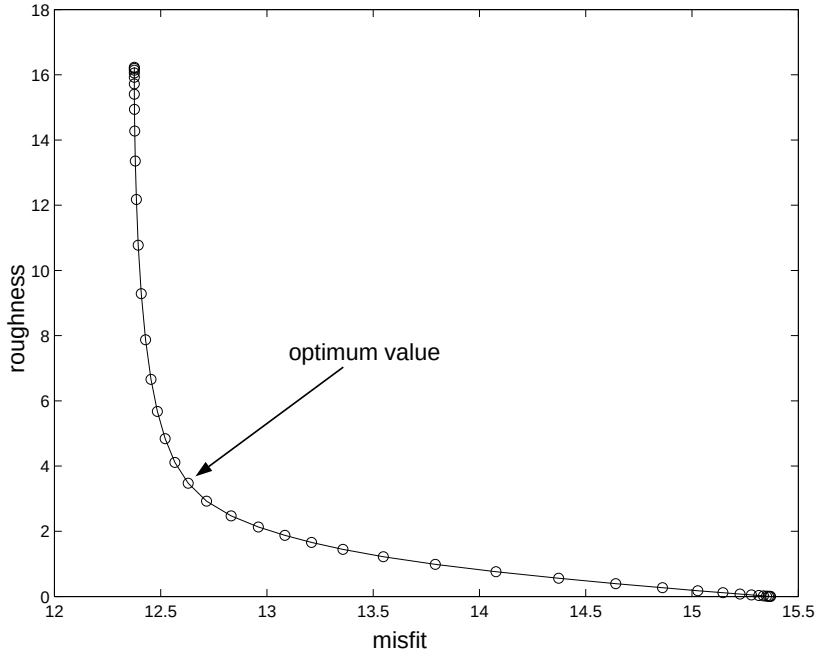

Figure 3.5: Tradeoff curve (misfit vs. roughness) for the synthetic migrations. Each data point on the curve represents a solution to equation 3.8 for a different value of ϵ. The optimum value of ϵ is then picked as the corner value of the tradeoff curve.

The depth to which each of the receiver function phases are migrated depends on the velocity model used in the migration. However, each phase has its own sensitivity to errors in the velocity model, and we can use these systematic errors to determine the accuracy of the velocity model. Figure 3.6 shows the imaging depth error for each of the receiver function phases as a function of errors in the velocity model, calculated from equations 3.1-3.4. for a 45 km thick crust. The depth of the resulting migrated images are least sensitive to the starting P-wave velocity model. A five percent over-estimation of Vp shifts each phase nearly uniformly 2-2.5 km deeper, and a five percent under-estimation shifts the phases 2-2.5 km shallower. Errors in the Vp/Vs ratio can be much more significant, and do not affect all phases in a uniform fashion. A five percent over-estimate of the Vp/Vs ratio results in imaging the Ps phase 4.5 km too shallow, the $PpPs$ phase 1.5 km too shallow, and the $PpSs + PsPs$ phase 2.3 km too shallow. A five percent under-estimate of Vp/Vs results in imaging the Ps phase 6 km too deep, the $PpPs$ phase 1.5 km too deep, and the $PpSs + PsPs$ phase 2.5 km too deep.

3.3.2 Stacking Multiple Migrated Images

The migrated output grids are stacked (summed) and then multiplied by a scaling matrix, so that large amplitudes in the image will only occur when the Ps, $PpPs$, and the (negative of the) $PpSs + PsPs$ migration images have the same polarity. The scaling matrix for stacking the Ps, $PpPs$, and $PpSs + PsPs$ phase migrations is given by

$$S = A \cdot B^n, \tag{3.12}$$

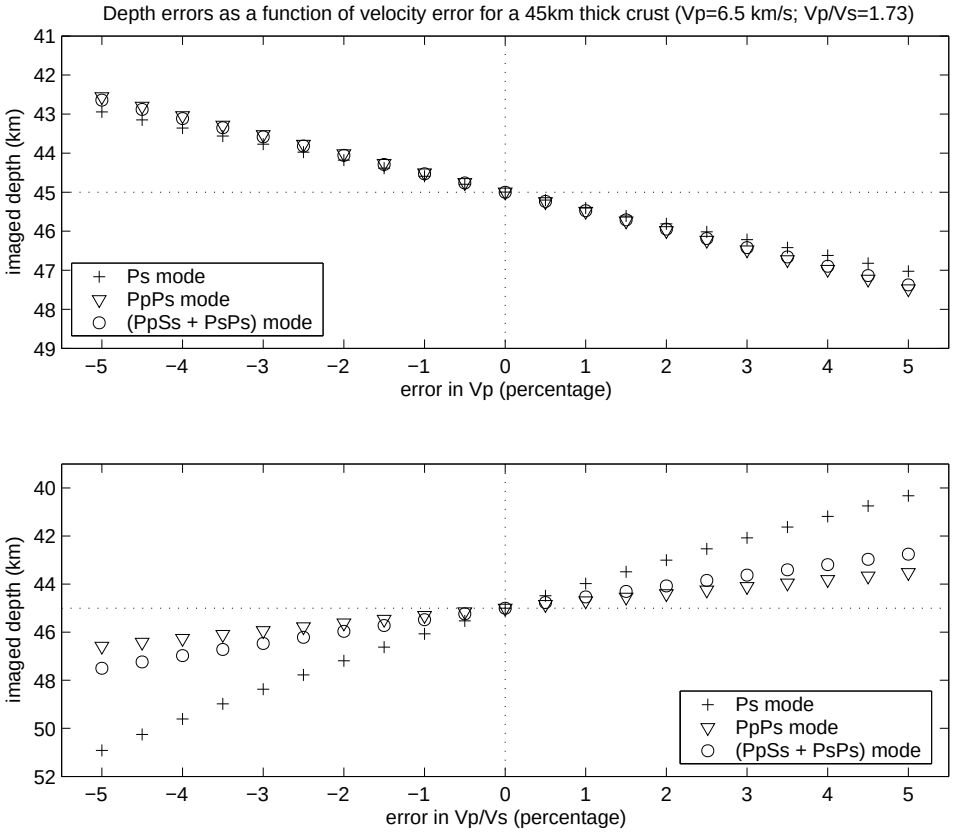

Figure 3.6: Imaging depth error as a function of velocity errors.

where

$$A = \frac{|median(M_{Ps} + M_{PpPs} - M_{PpSs+PsPs})|}{(|M_{Ps}| + |M_{PpPs}| + |M_{PpSs+PsPs}|)} \tag{3.13}$$

and

$$B = \frac{|M_{Ps} + M_{PpPs} - M_{PpSs+PsPs}|}{(|M_{Ps}| + |M_{PpPs}| + |M_{PpSs+PsPs}|)}, \tag{3.14}$$

and M_{Ps}, M_{PpPs}, and $M_{PpSs+PsPs}$ are the Ps, $PpPs$, and $PpSs+PsPs$ migrations respectively. The matrix **A** is a measure of the relative amplitude of the three images, and will have the maximum magnitude when at least two of the three images are the same polarity, and have similar amplitudes. The matrix **B** is a measure of the relative polarity of each image; in regions where all three images have the same polarity, **B** will have a magnitude of 1, otherwise it will have a magnitude less than 1. The parameter n controls the amount of scaling applied to the summed images. As $n \to \infty$, the summed images are multiplied by 1 where they all have the same polarity, and multiplied by 0 where they do not. We use scaling matrix **A** in conjunction with matrix **B** to downweight regions where two of the three images are nearly zero. In these regions matrix **B** will retain a value of 1, while matrix **A** will have a value near zero.

Figure 3.7 is an illustration of this stacking process for a single synthetic receiver function calculated for a 45 km thick crust. The first three panels show depth-converted receiver functions for the Ps, $PpPs$, and $PpSs + PsPs$ phases respectively, and the fourth panel is the stack of all three phases, which has been scaled by the scaling matrix **S**. Each of the three single-phase depth-converted traces shows a positive amplitude at 45 km which produces a positive phase on the stacked trace. Other phases present in the single-phase traces which do not have the same polarity are downweighted to approximately zero

in the stacked trace. Figure 3.4g,h shows the multiple phase, stacked images computed from the Kirchhoff-migrated and regularized-migrated single-phase images shown in 3.4a-f. Energy from receiver function multiples ($PpPs$ and $PpSs + PsPs$ phases) which was migrated to incorrect depths (125-200km) in the Ps migration (Figure 3.4a,b) has been cancelled out by the stacking process. Similarly, energy which was migrated to incorrect depths in the $PpPs$ and $PpSs+PsPs$ migrations is also cancelled out by the stacking process. The stacks show positive amplitudes placed at the correct depth of 45 km, and amplitudes near zero at all other locations. There are also small regions of positive amplitudes just beneath each station location associated with energy from the direct P-wave pulse that was not properly cancelled out by the stacking. The benefits of regularized migration versus standard Kirchoff migration is most evident in the stacked images (Figure 3.4g,h), with the regularized migration showing much better lateral coherency of receiver function amplitudes.

3.3.3 Migration Resolution

For imaging at crustal levels (to 60 km depth) the direct converted phase (Ps) for the basins and Moho, as well as basin multiples, has maximum energy at approximately 1-2 Hz, while the crustal multiples have most of their energy at 0.25-0.5 Hz. At Moho depths, this translates to about 1.5 km vertical resolution (1/4 wavelength) for the Ps phase, and 4 km vertical resolution for the crustal multiples. Fresnel zone widths at Moho depths are approximately 8 km at 1 Hz, and 18 km at 4 sec. periods. However, if we assume that the migration has properly collapsed diffracted energy, the horizontal resolution after migration is improved to approximately 1 wavelength (Stolt and Benson,

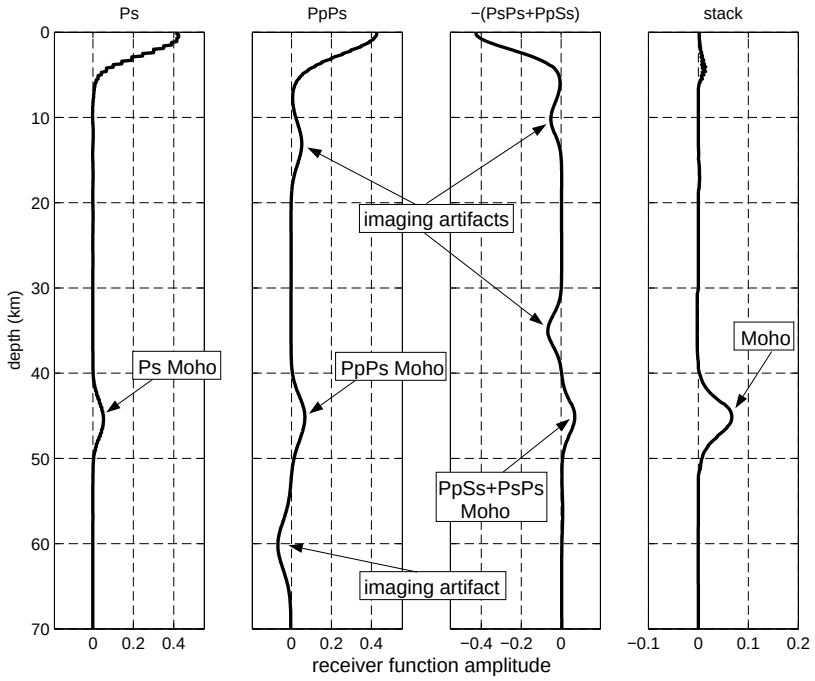

Figure 3.7: Example stack of the Ps, PpPs, and PpSs+PsPs phases.

1986), or to about 4 km horizontal resolution at 1Hz and 15 km horizontal resolution at 4 sec. periods.

Ultimately the resolution of the migrated image also depends on station spacing and data coverage. By casting data migration as a linear operator, we can forward model the migration resolution which is a function of the **G** matrix. It is important to note that the resolution does not depend directly on the data itself but on the geometry of the experiment, which is a function of the station spacing and data coverage (ray coverage) used to produce the migrated image. We can forward model the resolution of the migration by first creating a fictitious earth model ($\dot{\mathbf{m}}$), and then produce a data set by $\dot{\mathbf{d}} = \mathbf{G}\dot{\mathbf{m}}$. This is similar to a "checker board" type resolution test typically applied to test resolution in tomographic inversion. We can then use regularized migration (eqn. 3.8) to create an image from the forward modeled data, thus testing our ability to recover the forward modeled fictitious earth model. Figure 3.8 shows the forward modeled resolution for the station spacing and data coverage used for migration synthetic data in Figure 3.4. The fictitious earth model used for forward modeling is shown in Figure 3.8a, and the Kirchhoff migrated and regularized migrated cross sections are shown in Figure 3.8b and Figure 3.8c respectively. The Kirchhoff migrated image exhibits considerable variation in amplitude, with the highest amplitudes occurring at shallow levels in regions with close station spacing. Regularized migration (3.8c) produces an image with less variation in amplitude, more closely resembling the starting model (3.8a), and does not show variations in amplitude due to the irregular station spacing. Both the Kirchhoff migrated and regularized migrated images show that migration resolution decreases rapidly off the ends of the network.

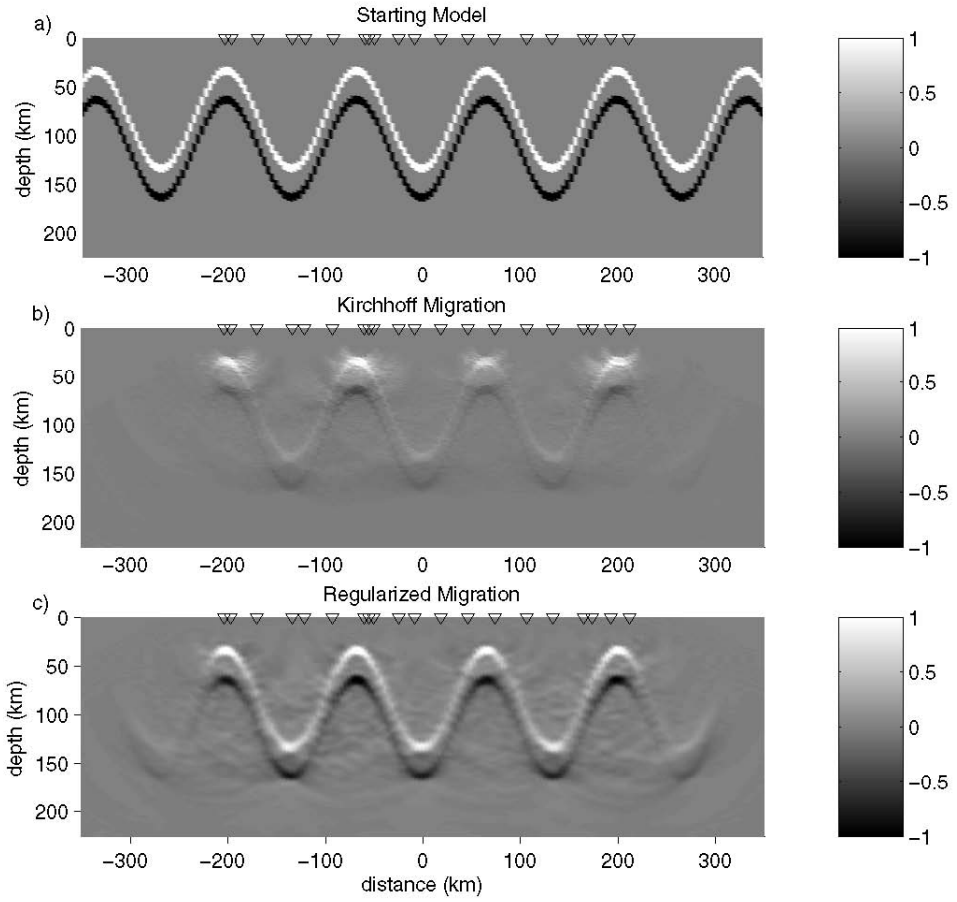

Figure 3.8: Forward modeled resolution of the Ps migration.

3.4 Conclusions

Instability in receiver function deconvolution, produced either by high background noise, or by holes in the vertical component spectra, can produce receiver function phases which are not representative of the velocity structure beneath the recording station. We have shown that by filtering receiver functions in the frequency-pseudo-wavenumber domain we can filter out receiver function amplitudes that have a high degree of variability as a function of horizontal slowness (epicentral distance) while preserving receiver function phases which have consistent moveout characteristics. Application of the methodology to synthetic receiver functions demonstrates that we can recover receiver function phases in the presence of high noise, with a 95% increase in correlation coefficient in filtered vs. unfiltered receiver functions as compared to noise free data.

Creating receiver function images from seismic data which may have irregular station spacing and uneven data coverage using standard receiver function imaging techniques can produce considerable imaging artifacts. We have shown that the application of regularized migration can minimize these imaging artifacts while producing an image with greater spatial continuity. We have shown that migrating both direct and reverberated P-to-S converted phases to their true subsurface position, and the subsequent stacking of these single phase migrations, can produce an image of the velocity discontinuity structure of the subsurface which has minimal imaging artifacts.

Acknowledgments

This study was supported by NSF grant EAR 9707190 and EAR 9706094. We also thank Los Alamos National Laboratory IGPP and the NMSU Arts and Sciences Research Center for their support.

References

Abers, G. A., Array measurements of phases used in receiver-function calculations: Importance of scattering, *Bull. Seis. Soc. Am., 88, n. 1,* 313-318, 1998.

Ammon, C.J., The isolation of receiver effects from teleseismic P-wave-forms, *Bull. Seis. Soc. Am., 81, n. 6,* 2504-2510, 1991.

Bostock, M. G., S. Rondenay, Migration of scattered teleseismic body waves *Geophys. Jour. Int., 137, n. 3,* 732-746, 1999.

Bostock, M., S. Rondenay, and J. Shragge, Multiparamter two-dimensional inversion of scattered teleseismic body waves, 1, Theory for oblique incidence, *J. Geophys. Res., 106,* 30785-30796, 2001.

Bracewell, R., The Fourier Transform and its Applications, 3rd ed., McGraw Hill, ISBN 0-07-303938-1, 2000.

Cassidy, J.F., Numerical Experiments in Broadband Receiver Function Analysis, *Bull. Seis. Soc. Am., 82, no. 3,* 1453-1474, 1992.

Clayton, R., and R. Wiggins, Source shape estimation and deconvolution of teleseismic body waves, *Geophys. J. R. Astr. Soc., 47,* 151-177, 1976.

Dellinger, J. A., S.H. Gray, G.E. Murphy, and J.T. Etgen, Efficient 2.5-D true-amplitude migration, *Geophysics, 65, n. 3,* 943-950, 2000.

Dueker K.G., and A.F. Sheehan, Mantle discontinuity structure beneath the Colorado Rocky Mountains and High Plains *J. Geophys. Res., 103, n. B4,* 7153-7169, 1998.

Duquet B., K. Marfurt, and J.A. Dellinger, Kirchhoff modeling, inversion for reflectivity, and subsurface illumination, *Geophysics, 65,* 1195-1209, 2000.

Eaton, D. W., J. Hope, and T. Bohlen, An Elastic Kirchhoff Method for Computing Synthetic Seismograms: Modeling the Receiver-function Response of an Irregular Moho Surface. SSA 97th annual meeting abstracts, *Seismological Res. Letts., 73, n. 2,* 232, 2002.

Fan, C., G. Pavlis, A. Weglein, and H. Zhang, Multiparamter Inversion of Forward Scattered Teleseismic Data Using an Inverse Scattering Series Method, *Eos Trans. AGU, 84(46),* Fall Meet. Suppl., Abstract S11E-0353, 2003.

Grand, S.P., and D. Helmberger, Upper mantle shear structure of North America, *Geophys. J. R. Astron. Soc., 76,* 399-438, 1984.

Langston, C.A., Corvallis, Oregon, Crustal and Upper Mantle Receiver Structure from Teleseismic P and S waves, *Bull. Seis. Soc. Am., 67,* 713-724, 1977.

Levander, A., USArray design implications for wavefield imaging in the lithosphere and upper mantle, *The Leading Edge, 22, n. 3,* 250-255, 2003.

Li, A., K. M. Fischer, S. van der Lee, and M. E. Wysession, Crust and upper mantle discontinuity structure beneath eastern North America, *J. Geophys. Res., 107, n. B5,* 10.1029/2001JB000190, 2002.

Nemeth, T., C. Wu, and G.T. Schuster, Least-squares migration of incomplete reflection data, *Geophysics, 64,* 208-221, 1999.

Poppliers, C. and G.L. Pavlis, Three-dimensional, prestack, plane wave migration of teleseismic P-to-S converted phases: 1. Theory, *J. Geophys. Res., 108,* 2112, doi:10.1029/2001JB000216, 2003.

Ryberg, T., M. Weber, Receiver function arrays: a reflection seismic approach, *Geophys. J. Int. 141,* 1-11, 2000.

Sheehan A.F., G.A. Abers, C.H. Jones, and A.L. Lerner-Lam, Crustal thickness variations across the Colorado Rocky Mountains from teleseismic receiver functions, *J. Geophys. Res., 100,* 20391-20404, 1995.

Sheehan A.F., P.M. Shearer, H.J. Gilbert, and K.G. Dueker, Seismic migration processing of P-SV converted phases for mantle discontinuity structure beneath the Snake River Plain, western United States, *J. Geophys. Res., 105, n. B8,* 19055-19065, 2000.

Shragge, J. and B. Artman, Wave-equation Imaging of Teleseismic Body-wave Coda, *Eos Trans. AGU, 84(46),* Fall Meet. Suppl., Abstract S11E-0335, 2003.

Stolt, R. H., and A. K. Benson, Seismic migration - theory and practice, *Geophysical Press, London-Amsterdam,*, 1986.

Tessmer, G., and A. Behle, Common reflection point data stacking technique for converted waves, *Geophys. Prosp, 36,* 671-688, 1988.

Yilmaz, Ö., Seismic Data Processing, *Society of Exploration Geophysicists*, 240-383, 1987.

Yuan, X., J. Ni, R. Kind, J. Mechie, and E. Sandvol, Lithospheric and upper mantle structure of southern Tibet from a seismological passive source experiment, *J. Geophys. Res., 102, n. B12,* 27491-27500, 1997

Zandt, G. and C.J. Ammon, Continental crust composition constrained by measurements of crustal Poisson's ratio, *Nature, 374,* 152-154, 9 March, 1995.

CHAPTER 4

Imaging the Seismic Structure of the Crust and Upper Mantle beneath the LA RISTRA Network

[1]A modified version of this chapter will be submitted to *Journal of Geophysical Research*, Wilson, D., R. Aster, J. Ni, S. Grand, M. West, W. Gao, W.S. Baldridge, and S. Semken, Imaging the Seismic Structure of the Crust and Upper Mantle Using Receiver Functions, Part 2: Application to the LA RISTRA Network, in preparation, JGR, 2004

Abstract

The seismic structure of the lithosphere in the southwestern United States is examined using receiver functions calculated from teleseismic arrivals recorded in the LA RISTRA (Colorado PLAteau, Rio Grande RIft, Great Plains Seismic TRAnsect) experiment. LA RISTRA was a NW-SE trending, 950.7 km linear network of broadband PASSCAL seismometers, deployed during 1999-2001 from Lake Powell, UT to Pecos, TX. We apply receiver function estimation and filtering methods developed in part 1 of this series to produce LA RISTRA receiver functions with decreased sensitivity to noise and deconvolutional instability. Crustal thickness and Vp/Vs ratios are estimated using both direct and reverberated P-to-S converted receiver function phases. We apply regularized receiver function migration methods to produce an image of the velocity discontinuity structure of the subsurface. Our results show much more topography at the base of the crust than has been observed in this region previously, with thickness changes up to 7 km over lateral distances of 50 km. Crustal thickness averages 44.1±2.4 km beneath the Great Plains (GP) and averages 46.8±2.0 km beneath the Colorado Plateau (CP). Crustal thinning beneath the RGR is relatively symmetric about the rift axis, with the thinnest crust (35 km) located directly beneath the rift axis, suggesting a pure shear stretching of the lithosphere beneath the RGR. We also observe a prominent northwest-dipping discontinuity, ranging from 65-85 km deep beneath the CP, and possible sub-crustal discontinuities beneath the GP. These discontinuities, along with recent xenolith data, may indicate preserved ancient lithospheric structures such as relict suture zones associated with Proterozoic subduction. We observe an upper mantle discontinuity at 250-300 km depth that may corre-

late with similar discontinuities observed beneath eastern North America. We also observe relatively flat discontinuities at 410 and 660 km depth, indicating there is not a large scale thermal anomaly beneath the RGR at these depths.

4.1 Introduction

The crustal basement in the RISTRA region (Figure 4.1) was formed by a series of continent building events in which Proterozoic terranes were accreted to the continent approximately from northwest to southeast (Condie, 1982; Bowring and Karlstrom, 1990). The accreted terranes consist of an assemblage of island arcs, oceanic plateaus, and marginal basin units (Condie, 1986; Condie and Selverstone, 1999; Frey et al., 2001). The array is oriented approximately parallel to the regional Proterozoic continental accretionary gradient, crossing two major Proterozoic province boundaries, the Mazatzal and Yavapai provinces (1.6-1.7 Ga and 1.7-1.8 Ga, respectively) in the northwestern portion of the array and the $\approx$ 1.1 Ga Grenville province boundary near the edge of the Delaware basin in the southeast (Condie, 1982; Bowring and Karlstrom, 1990). There is evidence for up to three periods of continental extension and rifting in the Proterozoic (Marshak and Paulsen, 1996). The first episode was northeast-southwest extension at 1.5-1.3 Ga, then east-west to northwest-southeast extension at 1.1 Ga in conjunction with the Grenville orogeny, and east-west extension at .7-.6 Ga. The regionally extensive, basement-penetrating faults which formed during this time may have provided zones of preexisting crustal weakness which shaped the style of Paleozoic crustal deformation (Marshak et al., 2000).

During the Pennsylvanian to Early Permian Ouachita-Marathon orogeny

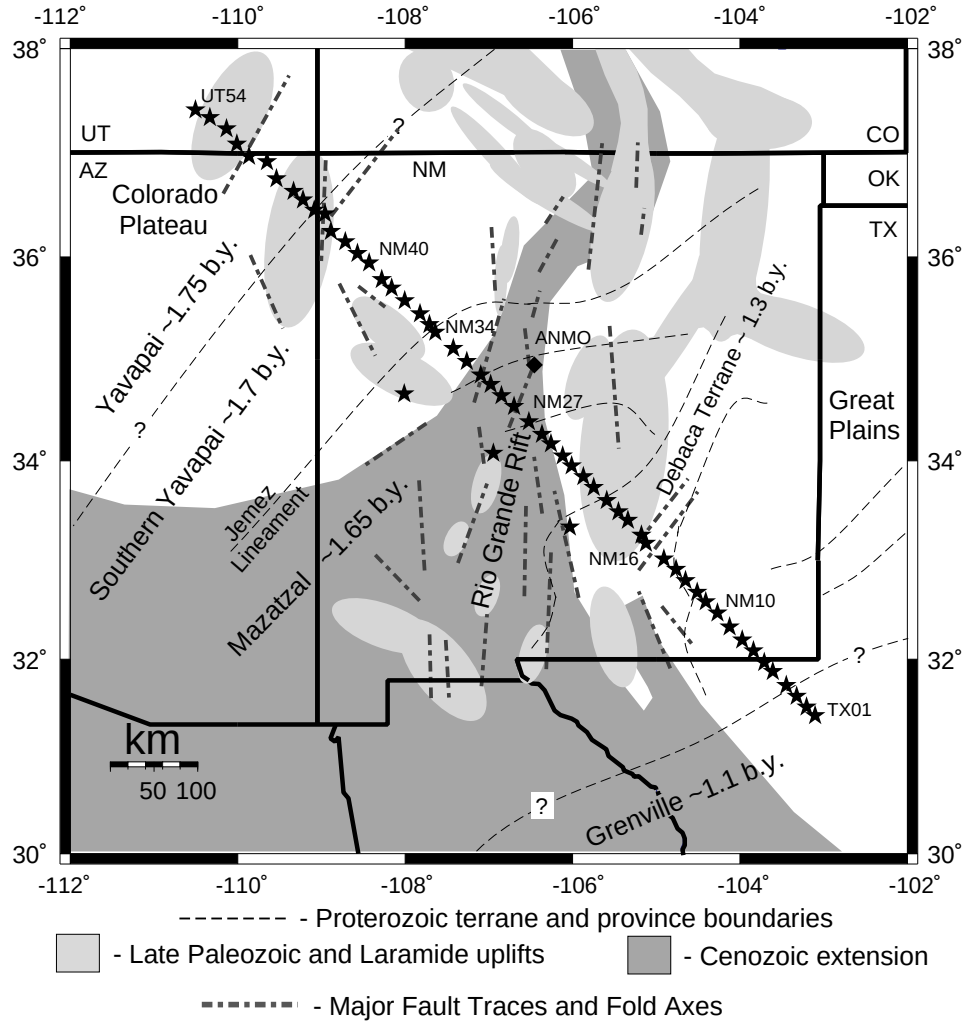

Figure 4.1: Regional tectonic setting of the LA RISTRA network, compiled from Baldridge et al. (1995), Bowring and Karlstrom (1990), Reed and others (1993), and Sloss (1988).

(320-280 Ma), the complex intraplate response associated with the collision between North America and South America-Africa resulted in the uplift of the Ancestral Rocky mountains (Kluth and Coney, 1981). During the Mesozoic Laramide (80-50 Ma) orogeny the region underwent compression as the Farallon slab was subducting along the North American west coast. Crustal deformation in the Laramide was characterized by fault-bounded, basement-cored uplifts separated by intervening sediment-filled basins. During this period the Farallon slab may have been been subducting at a low angle (e.g., Dickinson and Snyder, 1978) leading to suppressed subduction-related magmatism. Between approximately 43 to 30 Ma the flattened Farallon slab may have detached, and the accompanying mantle upwelling may have been the controlling factor for the space-time evolution of regionally prevalent mid-tertiary igneous activity (Humphreys, 1995).

During the past 30 million years the RISTRA region has been in extension, along with much of interior western North America. Extension has led to the creation of the Rio Grande Rift, but has left the Colorado Plateau relatively undeformed. The rift is thought to have formed in at least two stages. An initial stage at 30 to 20 Ma, associated with low angle faulting and doming in the crust, may have been caused by upper-mantle asthenospheric upwelling and thermal erosion of the lithosphere (Seager and Morgan, 1979; Morgan et al., 1986; Olsen et al., 1987). After perhaps 10 My of quiescence, rift activity resumed with high-angle normal faulting and alkalic basaltic volcanism (e.g., Baldridge et al., 1991). In the past 4 My there has been increased volcanism along the Jemez Lineament, including the Mount Taylor region, and where the Jemez Lineament and rift boundary intersects, in the Jemez mountains.

In this paper we examine the lithospheric structure which has been influenced by Proterozoic through recent tectonic events. A major challenge will be distinguishing features formed as early as the age of regional crustal formation from features which may have been caused by very recent tectonic movement. However, the two may be closely related as more recent tectonic events may take advantage of older structures and weaknesses in the lithosphere.

4.2 LA RISTRA data

The LA RISTRA project is designed to study the crust and mantle beneath the southwestern U.S. utilizing an exceptional data set consisting of 18 months of continuously recorded broadband IRIS PASSCAL data. LA RISTRA was a 950.7 km network consisting of 57 sites with 18±3.6 km station spacing approximately along a great circle from Lake Powell, UT to Pecos, TX. Three off-line stations deployed parallel to and southwest of the main network (Figure 4.1) are not considered in this study.

All sites were configured with Streckeisen STS-2 (120 s) seismometers and were continuously recording at a sampling rate of 20 samples/sec. RefTek 24-bit recording systems (72A-07 and 72A-08) were used at all sites. Seismometers were mounted on 10 cm thick pre-mix concrete pads with a diameter of approximately 0.3 m. Up to 0.4 m of dirt was mounded on top of each vault to provide further insulation and thermal mass. Local power supplies consisted of two 30 W solar panels and approximately 110 A-hrs of lead-acid battery capacity.

The network was designed to take advantage of the prolific teleseismic source zones along a western South American-Alaskan transect. Deployment began in July, 1999, and the network was fully deployed by November, 1999. The last station was removed from the field in May, 2001. During the deployment period 285 earthquakes with mb $\geq$ 5.6 were recorded with suitable offsets (25-105 degrees) for receiver function analysis (Figure 4.2). For a detailed analysis of the background noise characteristics from the RISTRA network, see Wilson et al. (2002).

4.3 Receiver Functions

We apply a receiver function estimation and filtering technique developed in Chapter 3 which filters out receiver function amplitudes that have a high degree of variability as a function of horizontal slowness (epicentral distance) while preserving receiver function phases that have consistent moveout characteristics.

Figure 4.3a shows receiver functions calculated for a single station for earthquakes from a range of epicentral distances (horizontal slownesses). The receiver functions were computed using waterlevel deconvolution (Clayton and Wiggins, 1976; Ammon, 1991) using a waterlevel of .001, and a value of $\alpha = 4$ used for Gaussian smoothing (low pass filtering). Although some receiver function phases appear to have lateral continuity, there is also a high level of noise present which appears as receiver function phases that do not appear on adjacent receiver functions. A number of receiver functions also exhibit "ringing", or periodic noise, possibly caused by deconvolution instability due to holes in the vertical component spectra. Figure 4.3b shows the transformation to the

Figure 4.2: Global distribution of the 84 earthquakes (diamonds) with mb $\geq$ 5.6, used for calculating the 2706 receiver functions used in this study. We use teleseisms from epicentral distances of 35-95 degrees, that are $\pm 10^{\circ}$ of the mean array azimuth. The RISTRA seismometer deployment is shown as great-circle swath.

$f-k$ domain of the receiver functions shown in Figure 4.3a. Noise, or receiver function amplitudes that vary rapidly as a function of horizontal slowness, is most evident in the $f-k$ domain as energy with relatively high values of k at low values of f. After filtering in the $f-k$ domain (Figure 4.3c,d), we observe much more lateral continuity of receiver function phases. Although we hve filtered out phases that change rapidly as a function of horizontal slowness, we have not filtered out receiver function phases which have consistent moveout characteristics such as the crustal phases observed in Figure 4.3c at approximately 5 and 16 sec.

4.3.1 Velocity Model Estimation

By measuring the time moveout of the direct converted and reverberated receiver function phases (assuming a locally flat layered structure), it is possible to estimate local depth and average Vp/Vs ratio between the surface and the discontinuity associated with each phase (e.g. Zandt and Ammon, 1995). In practice, individual phases can be difficult to observe and identify on individual traces. By assuming a starting average P-wave velocity model, we can estimate the local average crustal Vp/Vs ratio (γ) and thickness (H) at each station by stacking receiver function amplitudes at the predicted direct converted phase (Ps) times and reverberated phase ($PpPs$ and $PpSs+PsPs$) times for several receiver functions over a range of H and γ in the H-γ domain (Zhu and Kanamori, 2000). The stacked traces will produce a maximum where the three phases add constructively at the correct H and γ, and the variance can be calculated from the width of the solution peak. The main assumptions in this method are that the incoming P-wave is essentially a plane wave, that

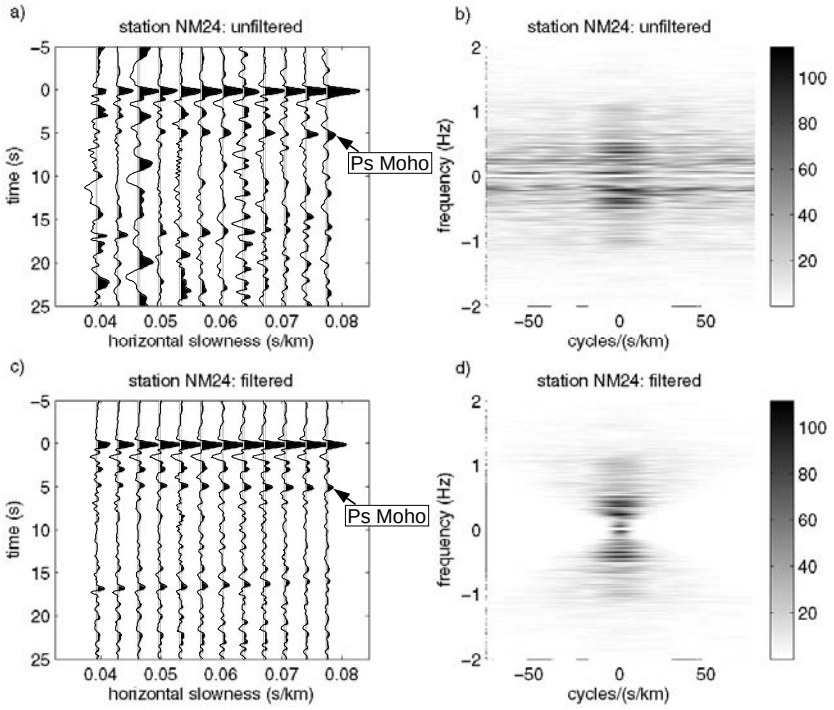

Figure 4.3: Receiver functions calculated for a single station (NM24) in the a) $t - p$ domain and b) $f - k$ domain before filtering, and in the c) $t - p$ domain and d) $f - k$ domain after filtering. Receiver functions have been binned into equally spaced p bins prior to transforming to the $f - k$ domain.

the velocity structure is comprised of locally flat lying layers, and that the crust is laterally uniform over the distance sampled be the direct and reverberating phases (20-50km). By using receiver functions from all azimuths and epicentral distances we minimize the effects of lateral heterogeneity and obtain the average crustal velocity structure at each station.

An important first step in estimating the crustal velocity model is an accurate characterization of the thickness and velocity of the near surface sedimentary layer. Since seismic velocities, particularly shear-wave velocities, can be much slower for sedimentary rocks than for crystalline rocks, there is potential for shear wave ray paths to have travel times of several seconds within the deep sedimentary basins crossed by the LA RISTRA network. Due to the strong impedance contrast between the rocks in the sedimentary basins and the crystalline Precambrian basement, sedimentary basins produce large primary and multiple phases. We use a variation of the Zhu and Kanamori (2000) method to estimate the seismic velocities from the basin primary and multiple phases. We assume that the layer thickness (H) is fixed and perform a search over a range of Vp and Vs to find the velocities which will cause the primary and multiple phases to add constructively and produce a maximum. The sedimentary layer thicknesses are well constrained (e.g., Sloss, 1988) from extensive exploration of basins for petroleum reserves.

We find that this method of estimating the sedimentary layer velocities works well when the sediments are sufficiently thick, or the velocities sufficiently slow, to produce distinct pulses for the primary and multiple modes. The predominantly Paleozoic sediments of the Delaware basin (TX01-NM10),

which are up to 7 km thick, produce distinct primary and multiple phases from which we have measured an average P-wave velocity of 4.96 km/s and S-wave velocity of 2.62 km/s (Vp/Vs = 1.89). The predominantly Mesozoic sediments of the San Juan basin (NM35-NM42), which are up to 2.2 km thick where the RISTRA network crosses, have sufficiently slow seismic velocities to produce distinct primary and multiple phases from which we have measured an average P-wave velocity of 3.05 and S-wave velocity of 1.35 (Vp/Vs = 2.26).

This method of estimating the sedimentary layer velocities does not work well in areas of steeply dipping shallow structure. Examples are station TX01-TX02 which are near the steep, fault-bounded edge of the Delaware basin's central basin platform, and stations NM28-NM30 which are in the narrow Albuquerque-Belen basin which is bounded by steeply dipping faults. In areas where we were unable to determine sedimentary layer velocities, an intermediate velocity between those found for the Delaware basin and San Juan Basin was used, depending on the average age of the local sedimentary layer.

The starting crustal P-wave velocity model used for velocity analysis was constructed using previous refraction data (e.g., Roller, 1965; Stewart and Pakiser, 1962; Sinno et al., 1986; Topozada and Sanford, 1976; Olsen et al., 1979). An example of receiver function phase moveout analysis is shown in Figure 4.4, and estimates of crustal thickness and Vp/Vs ratio along the RISTRA network are shown in figure 4.5. Crustal thickness estimates range from 43-51 km in the Colorado Plateau and 39-50 km thick in the Great Plains. Crustal thickness estimates show a uniform thinning to approximately 35 km thick in the center of the Rio Grande rift. While the thickness estimates from

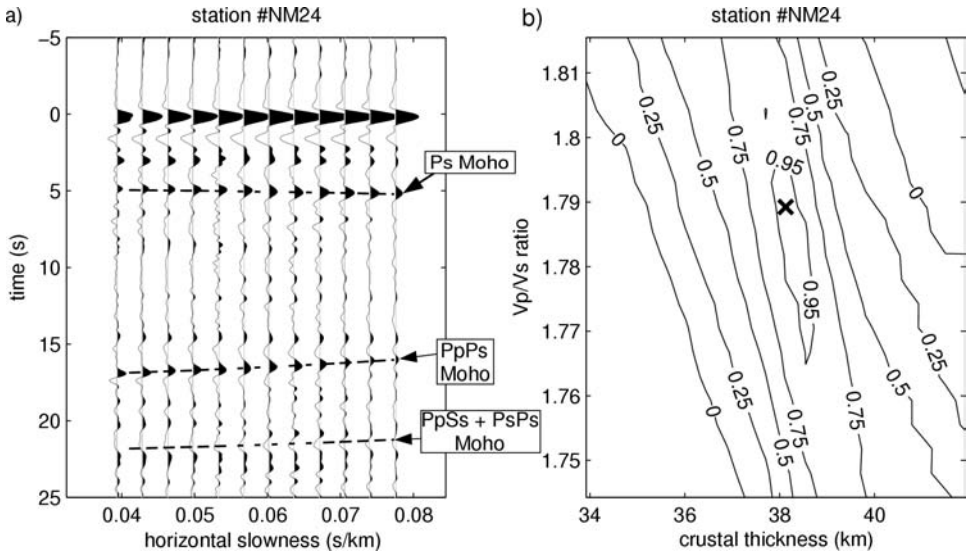

Figure 4.4: a) Receiver functions calculated for a single station (NM24) using events at a range of epicentral distances. Receiver functions have been binned into equally spaced p bins prior to transforming to the $f - k$ domain. Direct converted phases have moveout curves opposite in sign to reverberated phases, allowing us to discrimination among phase types. Dashed lines indicate best fit solutions obtained from moveout analysis. b) Contour of amplitudes in the $H - \gamma$ domain determined from moveout analysis. The best fit solution is indicated by the symbol **X**.

the center of the Rio Grande rift have lateral continuity (no large thickness jumps from station to station), thickness estimates from the Colorado Plateau and Great Plains show much more lateral variability.

Estimates of crustal average Vp/Vs ratios along the RISTRA array (Figure 4.5b) show high variability from station to station, with ratios ranging from 1.71 to 1.80. This range in values, as well as the associated high magnitude error estimates, is in part due to the shape of the solution peak shown in Figure 4.4b, which is stretched out in the direction of the γ axis. However, a high level

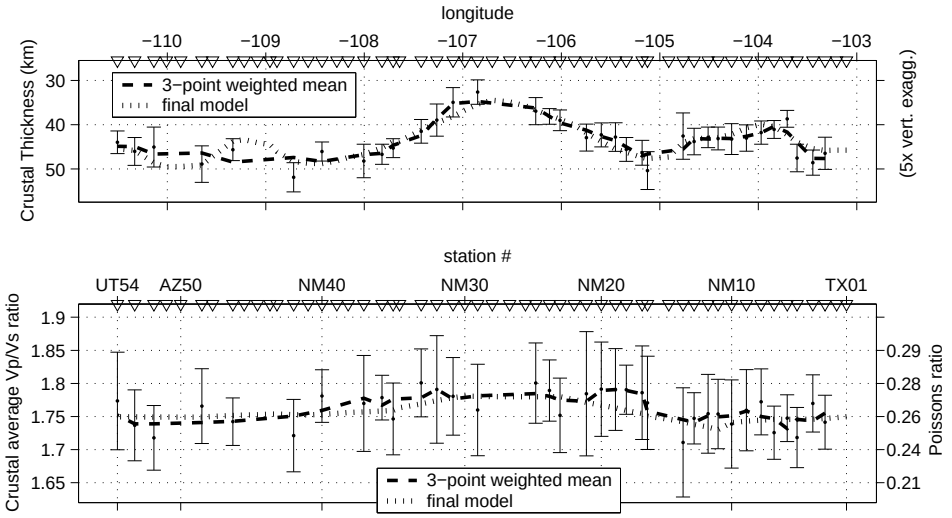

Figure 4.5: Results of the reverberation analysis.

of variability, along with lateral variability in crustal thickness estimates, may indicate strong lateral velocity heterogeneity or considerable Moho topography. Since this method of velocity estimation assumes a locally flat, homogeneous velocity model, violating one or both of these assumptions will produce an incorrect result. For migration of receiver functions, we use a smoothed version of these results, with Vp/Vs smoothly varying from 1.74 in the Great Plains, up to 1.78 near the RGR, and 1.75 in the Colorado Plateau. Detailed velocity analysis results are given in appendix B (Table B.1).

4.3.2 Receiver Function Migration

The RISTRA array provides multicomponent broadband seismic data along a long (950km) and densely occupied (approximately 18 km interstation spacing) transect which is well suited for the application of seismic migra-

tion techniques. We apply a regularized Kirchhoff receiver function migration method, developed in part 1 of this series, to produce images of the crust and upper mantle discontinuity structure beneath the RISTRA array. Figure 4.6a shows the Ps phase migrated receiver function cross section. A number of first order features can be seen including the direct conversion from the bottom of the Delaware basin (stations TX01-NM10) at 5-7 km depth, as well as strong basin multiples which are migrated to the incorrect depth of 20-30 km, directly beneath the correctly imaged Ps phase. The Ps phase generated at the Moho is also evident, occurring prominently at 35-50 km deep across the network. The Ps phase cross section also shows apparent sub-crustal discontinuities; however, in this single phase cross section, it is difficult to know if these apparent discontinuities are due to Ps phase energy migrated to the correct depth, or if they are caused by multiples from shallower events, which have been migrated to the incorrect depth (imaging artifacts).

The migrated image of the $PpPs$ and phase is shown in figure 4.6b. The $PpPs$ phase generated at the Moho, which was imaged at 150-170 km deep in the Ps migration, has now been moved to the correct depth of 35-50km deep. However, there are now evident imaging artifacts generated by the Ps phase which is now imaged shallower than its true depth. This can clearly be seen for the Moho Ps phase, which is now imaged at $\sim$10 km depth. Similarly, the migrated image of the $PpSs + PsPs$ phase (Figure 4.6)c, shows that the seismic energy for this phase has been moved to the correct depth, and the Ps and $PpPs$ phases are now imaging artifacts, imaged shallower than their true depth.

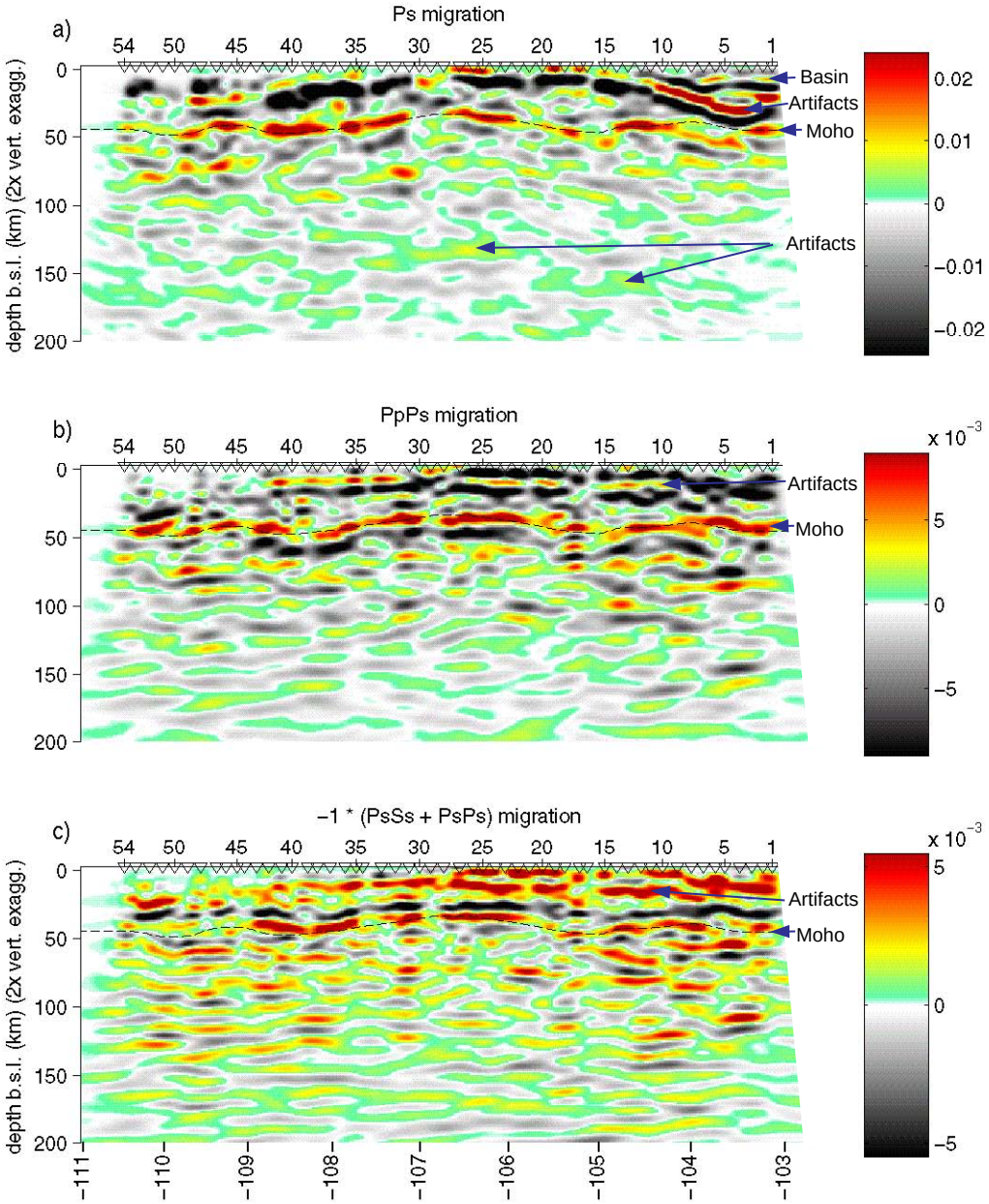

Figure 4.6: Migrated cross sections for the a) Ps, b) PpPs, and c) PpSs + PsPs phases. Positive amplitudes indicate a change from relatively high velocities below the discontinuity to lower velocities above. Each single phase migration shows a prominent Moho signal, but there are also evident imaging artifacts present.

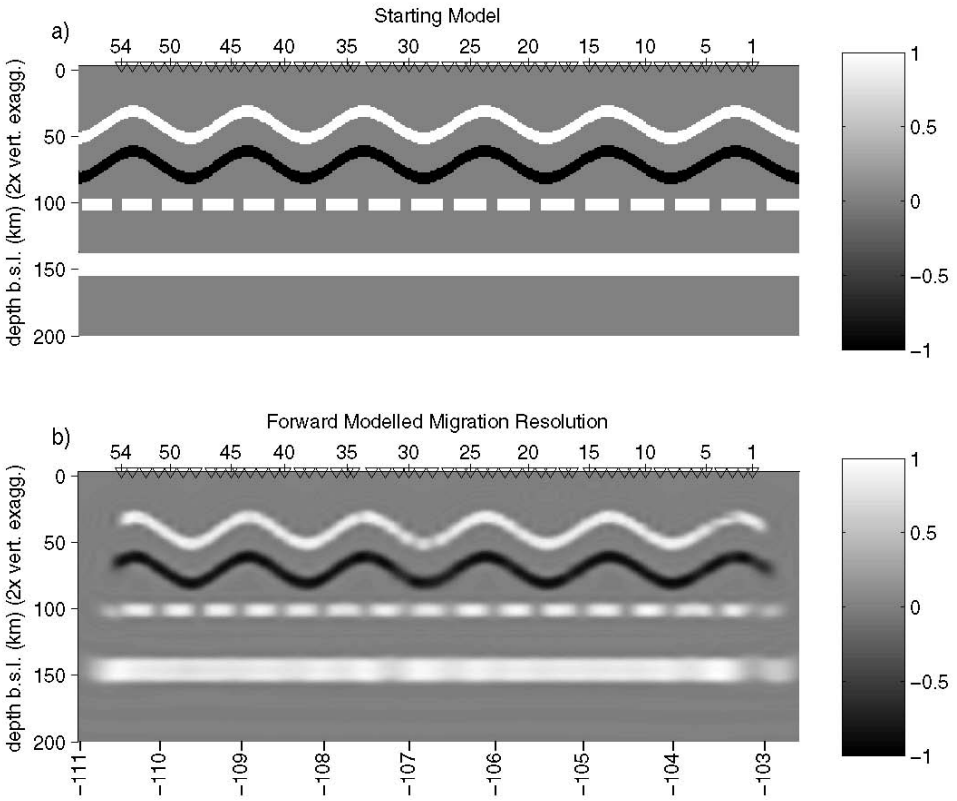

Figure 4.7: Forward modeled resolution of the lithosphere scale migration.

Forward modeled resolution for the lithosphere scale migration is shown in Figure 4.7. Regularized migration does an excellent job recovering the starting model, with minimal evident lateral variation in receiver function amplitudes. This is an indication that the number of receiver functions used in the imaging, and their associated raypaths, give ample coverage of the imaged region. Migration resolution decays rapidly off the ends of the network, but does extend slightly further off the northwestern edge of the network due to a larger number of receiver functions used from the northwest.

Figure 4.8 shows the upper mantle receiver function image consisting of the migrated Ps phase only. Reverberated receiver function phases originating from depths greater than 200 km are not included in the deep imaging because they lack coherence due to their long delay times (greater than 100 s) relative to the first P-wave arrival, and because they travel over a much larger lateral distance and therefore suffer greater influence from lateral velocity heterogeneity. Figure 4.8 shows that the upper mantle discontinuities at 410 and 660 km depth are relatively flat, with variations less than 20 km across the network. An apparent discontinuity is also observed at ∼250 km depth and shows highest amplitude beneath the northwestern half of the network, and appears to get slightly deeper to the southeast. The forward modeled upper mantle migration resolution is shown in Figure 4.9, and shows good later continuity of receiver function amplitudes. The effect of having fewer events to the southeast is more evident in the deep migration resolution, which fades out more rapidly to the southeast.

4.3.3 Stacking multiple phase images

The resulting stack of multiple phase images is shown in Figure 4.10. By stacking the migrated grids from multiple phases we have canceled a considerable amount of seismic energy (imaging artifacts), which was present in the individual phase migrated cross sections (Figure 4.6). Also, we have increased the relative amplitude of phases which appear at the same depth in the individual migrations. The most prominent phase in the resulting stack is the base of the crust (Moho) which appears at 40-50 km depth beneath the Colorado Plateau and Great Plains, and thins to a minimum of 35 km thickness in the

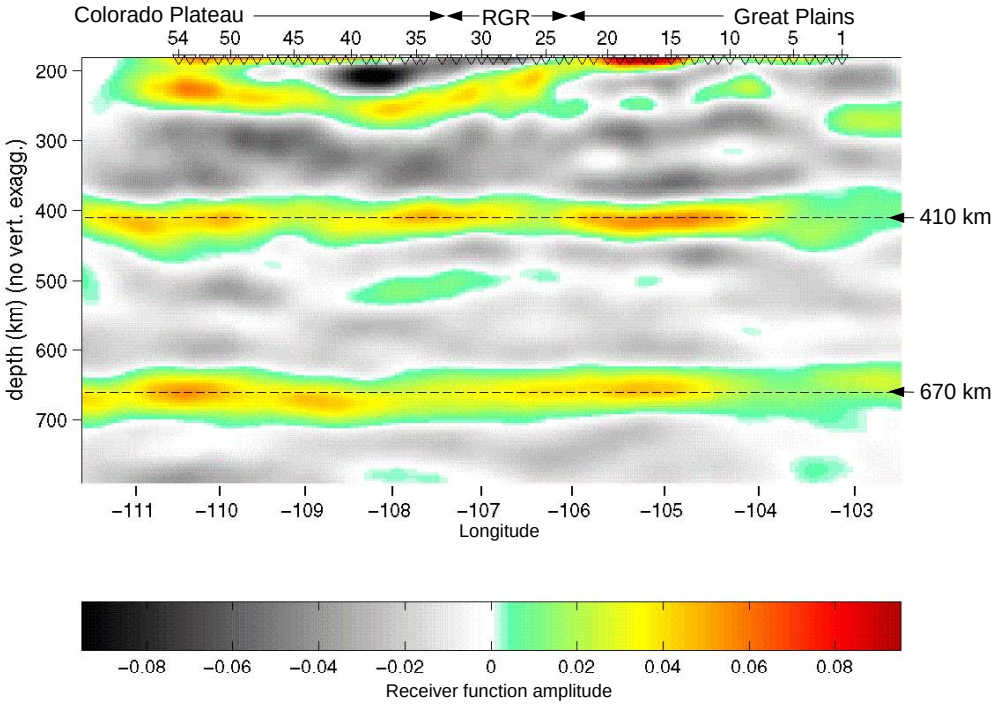

Figure 4.8: Migrated receiver function image of the upper mantle.

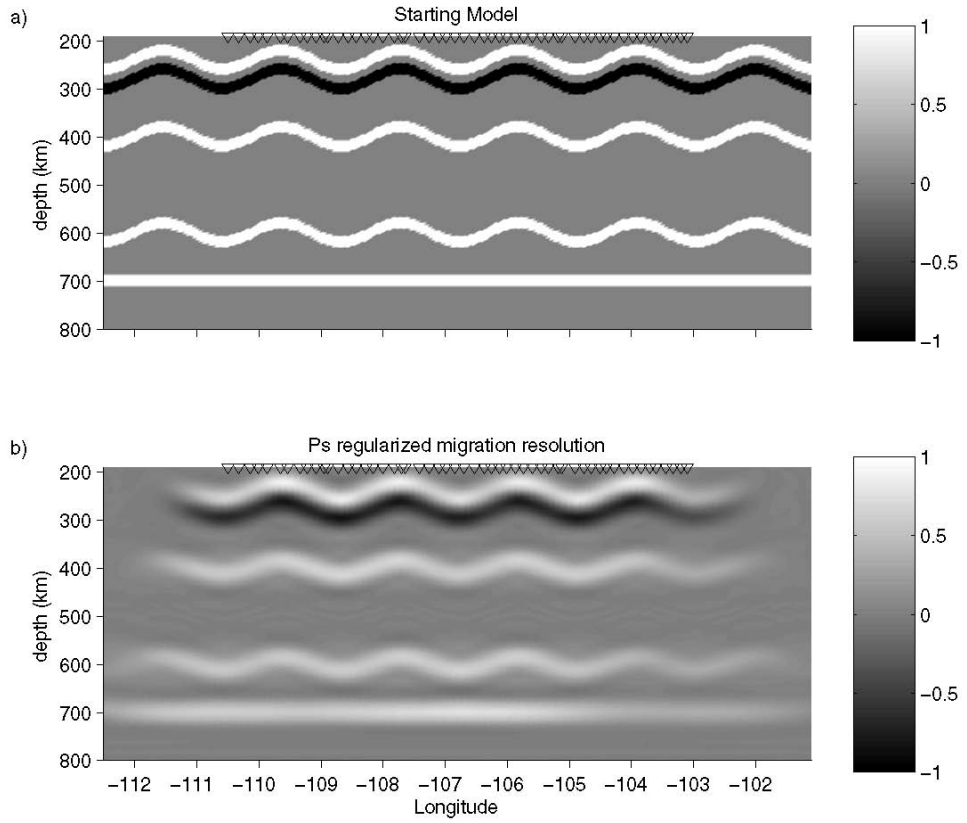

Figure 4.9: Forward modeled resolution for the upper mantle migration.

center of the Rio Grande rift. A number of sub-crustal discontinuities can also be seen, the most prominent of which is a northwestern dipping ($\sim 6.4°$) discontinuity at 65-85 km depth beneath the Colorado Plateau. Discontinuities can also be seen at 70-85 km depth beneath the center of the Rio Grande rift and at 50-120 km depth beneath the Great Plains. Sporadic seismic energy is also present at ∼150 km depth along the network; however, this is the depth that the crustal multiples arrive in the Ps migrated cross section (Figure 4.6a). If we have not cancelled out the multiples properly, which could be caused by velocity model errors or strong lateral velocity heterogeneity, the discontinuities at ∼150 km depth may be imaging artifacts propagating through into our final image. Other examples of imaging artifacts not being properly canceled can be seen at ∼10 km depth beneath stations NM09-NM12 and NM38-NM42. This is caused by imaging artifacts in the Ps phase image (from the strong $PpPs$ and $PpSs + PsPs$ multiples generated in the low velocity sediments of the San Juan and Delaware Basins) aligning with imaging artifacts in the reverberated phase images (from the Moho Ps energy which is now imaged shallower). The stacked receiver function image provides a valuable tool in assesing the alignment of receiver function phases; however, final interpretation should be done using the individual phase migrations along with the stacked cross section to avoid interpreting imaging artifacts that are not properly canceled as earth structure.

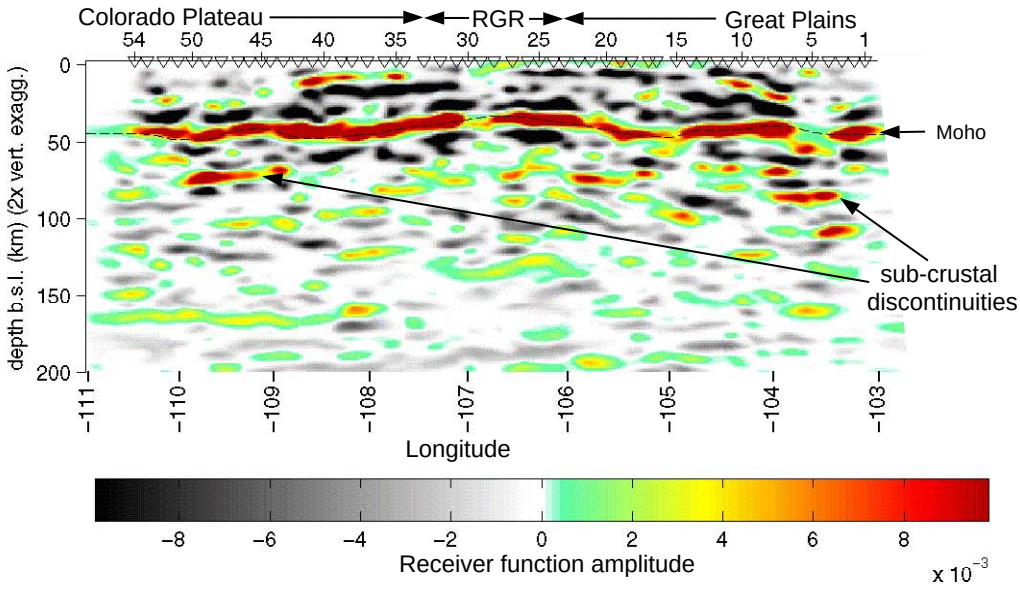

Figure 4.10: Stack of the a) Ps and PpPs phases, and b) Ps, PpPs, and PpSs+PsPs phases. Note the relative amplitude increase of the Moho and a number of sub crustal distcontinuities compared to the individual phase migrations. Although phase stacking has cancelled out many of the imaging artifacts, some artifacts are still evident at ∼170 km depth beneath the Colorado Plateau (Moho reverberations) and at ∼10 km depth beneath stations NM09-NM12 and NM38-NM42 (sedimentary basin reverberations).

4.4 Discussion

4.4.1 The Colorado Plateau

The average crustal thickness of the Colorado Plateau (46.8±2.0 km) is only modestly thicker than crustal thickness in the Great Plains (44.1±2.4 km; Figure 4.10); however, the Colorado Plateau maintains anomalously high elevation (∼2 km above sea level). The amount of buoyancy provided by this additional crustal thickness (2.7 km) would result in approximately .5 km of uplift (assuming isostasy, and crust and mantle densities of 2.7 and 3.3 g/cm^3 respectively). This suggests that the high elevation of the plateau cannot be due to shallow compensation by thickened crust alone, and argues for either a more buoyant crustal composition, mantle buoyancy, or a combination of the two.

Numerous analyses of crust and mantle xenoliths from the Najavo volcanic field, located in the heart of the Colorado Plateau, have provided insight to the composition, age, and tectonic history of the crust and mantle beneath the Colorado Plateau. Xenoliths from all levels of the Colorado Plateau crust show Mid-Proterozoic ages (1.7-2.0 Ga) with no indication of later magmatic underplating (Wendlandt et al., 1993). This suggests, along with the fact that the Colorado Plateau has not experienced major deformation, that structures associated with crustal formation may still be preserved. Selverstone et al. (1999) suggest that compositional changes in crustal xenoliths across the Najavo field are consistent with a northwest dipping Proterozoic subduction zone, with the crustal suture located near where the RISTRA network crosses the Arizona/New Mexico border (station NM44). This location coincides with the

approximate location where the receiver function image (Figure 4.10) shows a significant welt at the base of the crust, as well as coincident with the western edge of the San Juan basin, expressed at the Hogback monocline..

Recent surface wave inversion results from the RISTRA network (West et al., 2004) show a high velocity lithospheric root beneath the Colorado Plateau to 140-160 km depth. Mantle xenolith data from the Colorado Plateau suggest that the sub-crustal lithosphere is relatively depleted in Fe rich olivine (Smith, 2000; Lee et al., 2001) which could increase the buoyancy of the Colorado Plateau. Mantle xenolith data further suggests that at the time of magmatism (30-20 ma), the Colorado Plateau was characterized by a cool root analogous to those beneath Archean cratons, with compositional similarity to oceanic lithosphere (Roden and Shimizu, 1993; 2000). This cool root may extend to depths up to 140 km (Riter and Smith, 1996), and has U-Pb zircon ages which are mid-Proterozoic (Smith et al., 2002). If the sub-crustal lithosphere beneath the Colorado Plateau is mid-Proterozoic in age and has compositional similarity to oceanic lithosphere, then the sub-crustal discontinuities we are imaging in the receiver function cross sections could represent subducted slabs which have been trapped in the lithosphere since terrane accretion in the Proterozoic. Proterozoic suture zones within the crust are typically projected to be more steeply dipping (e.g., Selverstone et al., 1999) than the northwestern dipping ($\sim 6.4^{\circ}$) discontinuity observed at 65-85 km depth beneath the Colorado Plateau (4.10). This structure may represent proterozoic oceanic crust than was subducting to the northwest at a relatively shallow angle because it was relatively young and therefore had elevated temperatures (Selverstone et al., 1999).

A thick, cool lithospheric root should not contribute to the added buoyancy of the Colorado Plateau; however, surface wave inversion results by West et al. (2004) have identified an asthenospheric low velocity channel beneath the Plateau (160-300 km depth) and demonstrate that it is adequate to provide the added buoyancy to support approximately 1.3 km of the high elevation of the Colorado Plateau. This added buoyancy, along with the added buoyancy from slightly thickened crust, may explain the excess elevation of the Colorado Plateau.

4.4.2 The Rio Grande Rift

Extensional deformation of the lithosphere can be characterized by two end member models, a pure shear mode (McKenzie, 1978) and a simple shear mode (Wernicke, 1985). The pure shear mode is characterized by a brittlely deforming upper crustal layer and a ductilely deforming lower crust and mantle lithosphere. This produces symmetric thinning and a symmetric lithospheric cross section with the region of greatest lithospheric and crustal thinning located directly beneath the rift axis. The simple shear mode is characterized by shear along a low angle detachment fault which may span the entire lithosphere (Wernicke, 1985). This produces an asymmetric lithospheric cross-section with the region of greatest crustal thinning offset laterally from the region of greatest mantle lithosphere thinning. This offset can produce asymmetry in heat flow, flexural uplift, and thermal uplift (Buck et al., 1988)

Geochemical analysis of volcanic rocks from the RGR indicates a transition from rocks with a lithospheric source to rocks with an asthenospheric source (Perry et al., 1988), which is interpreted as a thinning of the litho-

sphere. Further analysis indicates that the lithosphere has thinned relatively symmetrically and the greatest lithospheric thinning is centered beneath the axis of the rift (Baldridge et al., 1991; McMillan, 1998), favoring a pure shear mode of deformation. Also, analysis of gravity data indicates a symmetric thinning of the lithosphere which closely tracks the rift axis (Cordell et al., 1991). Surface wave inversions (West et al., 2004) and tomography results (Gao et al., 2004) from the RISTRA network show a zone of low velocity ranging from 65 to 125 km depth, centered beneath the rift. These lines of evidence, along with the symmetric thinning of the crust observed in receiver function images (Figure 4.10) indicate an overall pure shear extensional mechanism for the Rio Grande rift lithosphere.

Upper mantle receiver function results (Figure 4.8) show negligible topography on the 410 km (exothermic, α-olivine to β-spinel) and 670 km depth (endothermic; γ-spinel to perovskite) mantle transition zone discontinuities, which indicates a lack of a localized thermal anomaly under the region at these depths. However, other mineral transitions such as majorite-perovskite which also occurs around 670 km depth, and has a positive pressure-temperature slope, can decrease the magnitude of the depth change predicted for the 670 km discontinuity (Akaogi and Ito, 1999). But, since the overall transition zone thickness does not change significantly, it indicates that mantle temperature at 410 to 670 km depth beneath the RGR are not significantly different than surrounding upper mantle temperatures. A strong increase in temperature associated with a deep mantle upwelling would be expected to compress the transition zone thickness by around 15 km per 100° C (Bina and Helffrich, 1994). This suggests that the thermal signature of the Rio Grande rift may be

predominantly confined to the uppermost mantle (less than 400 km depth).

An apparent discontinuity observed at ∼250 km depth (Figure 4.8) shows highest amplitude beneath the northwestern half of the network, and appears to get slightly deeper and lose continuity to the southeast. A similar discontinuity has been observed beneath the MOMA (Missouri to Massachusetts) array in the eastern United States (Li et al., 2002). The discontinuity appears at 270-280 km depth beneath the eastern portion of the array, then gets gradually deeper and shows more complex scattering in the western third of the array. This discontinuity is not observed globally, and its origin is under debate, but it may represent the base of an asthenospheric low velocity zone (Li et al., 2002). If this is the case beneath the RISTRA network, this discontinuity may represent the base of the asthenospheric low velocity channel identified by West et al. (2004). This is also supported by the observation that the ∼250 km depth discontinuity loses amplitude in the southeastern 1/3 of the network (Figure 4.8) which corresponds to the southeastern truncation of the low velocity channel (West et al.,2004).

4.4.3 The Great Plains

Crustal thickness in the Great Plains ranges from 40 km to 50 km with an average thickness of 44.1±2.4 km km. An apparent crustal thickening, centered near NM15, corresponds with right-lateral, strike-slip faults mapped on the surface (Figure 4.1). In the individual phase cross sections (Figure 4.6), strong reverberations from the Delaware basin are evident. The reverberations interfere with Moho and deeper direct conversion structural information. However, as the other migrated images are stacked in, these reverberations become

greatly attenuated, while direct converted energy mapped to its correct depth is enhanced.

We observe several dipping sub-crustal discontinuities beneath the Great Plains, but there is not an extensive collection of xenolith data to provide insight into the composition and age of the lithosphere like there is beneath the Colorado Plateau. However, exposures in west Texas, across the Grenville front, provide a profile that records more than 300 m.y. of orogenic activity, including arc-continent and continent-continent collision (e.g., Mosher, 1998). While the collisional suture is expressed at the surface near the southeasternmost end of the RISTRA network in western Texas, the associated subducted oceanic crust could be located well beneath stations located further northwest. Much of the region crossed by the southeastern portion of the RISTRA network (TX01-NM10) may have been extending in a back arc basin setting while arcs were accreting to the continent further southeast (1290-1230 Ma), and later continental rifting may have occurred (1150-1120 Ma) in the location of the present day faults associated with the central basin platform (Mosher, 1998; Kluth and Coney, 1981).

4.5 Conclusions

By migrating and subsequently stacking multiple receiver function phases we produce a seismic cross section of the structure along the LA RISTRA network which has enhanced primary conversions and attenuated reverberated phases. The composite migrated image of the Moho shows dramatic thinning of approximately 10 km under the central rift, as well as intriguing second-order features that suggest significant short-wavelength Moho topo-

graphic and impedance contrast variability (e.g., thickness changes of up to 7 km over lateral distances of less than 100 km). The thinnest crust is centered along the Rio Grande rift axis, indicating a pure shear thinning of the lithosphere. This is further supported by the rift centered region of low velocities observed in surface wave inversions and tomography results, as well as by regional isotopic data. Colorado Plateau crust is on average 2.7 km thicker than Great Plains crust, providing up to .5 km of Colorado Plateau uplift. This, along with added buoyancy from a deep, low-velocity channel imaged in surface wave analysis, may explain the excess elevation of the Colorado Plateau. We observe a prominent northwest-dipping discontinuity, ranging from 65-85 km deep beneath the Colorado Plateau, and possible sub-crustal discontinuities beneath the Great Plains. These discontinuities, along with recent xenolith data, may indicate preserved ancient lithospheric structures such as subducted oceanic crust associated with Proterozoic continental accretion. We observe an upper mantle discontinuity at 250-300 km depth that may correlate with similar discontinuities observed beneath eastern North America. This discontinuity may represent the base of an asthenospheric low velocity channel observed in surface wave velocity images. We also observe relatively flat discontinuities at 410 and 660 km depth, indicating there is not a large scale thermal anomaly beneath the RGR at these depths.

Acknowledgments

The RISTRA team especially thanks the PASSCAL Instrument Center at New Mexico Tech for planning and data processing assistance. We also thank the dozens of private landowners, the New Mexico State Land Office, the United States Forest Service, the United States Bureau of Land Management, the United States Fish and Wildlife Service, the Southern Utah Wilderness Alliance, Isleta Pueblo, Laguna Pueblo, and the Navajo Nation for assistance in the permitting the siting of these instruments. Persons wishing to conduct geological investigations on the Navajo Nation must first apply for and receive a permit from the Navajo Nation Minerals Department, PO Box 1910, Window Rock, Arizona, 86515, 928-871-6587. This study was supported by NSF grant EAR 9707190 and EAR 9706094. We also thank Los Alamos National Laboratory IGPP and the NMSU Arts and Sciences Research Center for their support. Essential field assistance was provided by Joe Leon, Eric Matzel, Richard Rapine, Frederik Tilmann, Wei-Chuang Huang, Al Blackhorse, Anca Rosca, Laurecita Luna, and Dueker's Diggers.

References

Akaogi, M. and E. Ito, Calorimetric study on majorite-perovskite transition in the system $Mg_4Si_4O_{12}-Mg_3Al_2Si_3O_{12}$: transition boundaries with positive pressure-temperature slopes, *Physics of the Earth and Planetary Interiors, 114,* 129-140, 1999.

Aldrich, M. J., Jr., Laughlin, A. W., A model for the tectonic development of the southeastern Colorado Plateau boundary, *J. Geophys. Res., 89, n. B12,* 10207-10218, 1984.

Ammon, C.J., The isolation of receiver effects from teleseismic P-wave-forms, *Bull. Seis. Soc. Am., 81, n. 6,* 2504-2510, 1991.

Baldridge, W.S., F. V. Perry, D.T. Vaniman, L.D. Nealey, B.D. Leavy, A.W. Laughlin, P. Kyle, Y. Bartov, G. Steinitz, and E. S. Gladney, Middle to late Cenozoic magmatism of the southeastern Colorado Plateau and central Rio Grand rift (New Mexico and Arizona, U.S.A.): a model for continental rifting, *Tectonophysics, 197,*, 327-354, 1991.

Bina, C. and G. Helffrich, Phase transition Clapeyron slopes and transition zone seismic discontinuity topography, *J. Geophys. Res., 99, n. B8,* 15853-15860, 1994.

Bowring, S.A., and K.E. Karlstrom, Growth, stabilization, and reactivation of Proterozoic lithosphere in the Southwestern United States, *Geology, 18, n. 12,* 1203-1206, 1990.

Buck, R.W., F. Martinez, M. S. Steckler, J.R. Cochran, Thermal Consequences of Lithospheric Extension: Pure and Simple, *Tectonics, 7,* 213-234, 1988.

Clayton, R., and R. Wiggins, Source shape estimation and deconvolution of teleseismic body waves, *Geophys. J. R. Astr. Soc., 47,* 151-177, 1976.

Condie, K.C., Plate-tectonics model for Proterozoic continental accretion in the southwestern United States, *Geology, 10, n. 1,* 37-42, 1982.

Condie, K.C., Geochemistry and Tectonic Setting of Early Proterozoic Supracrustal Rocks in the Southwestern United States, *Journal of Geology, 94,* 845-864, 1986.

Condie, K.C., and J. Selverstone, The Crust of the Colorado Plateau: New Views of an Old Arc, *Geology, 107,* 387-397, 1999.

Cordell, L., Y.A. Zorin, and G.R. Keller, The Decompensative Gravity Anomaly and Deep Structure of the Region of the Rio-Grande Rift, *Jour. Geoph. Res., 96,* 6557-6568, 1991.

Dickinson, W.R., and W.S. Snyder, Plate Tectonics of the Laramide Orogeny, *Geol. Soc. of Amer., Memoir 151,* 355-366, 1978.

Frey, B.A., K. C. Condie, and R. Kerrich, The Iron King Volcanics; a remnant of an oceanic plateau accreted to southwestern Laurentia 1.7 Ga, *Geological Society of America, Rocky Mountain Section, 53rd annual meeting, Abstracts with Programs, Geological Society of America, 33, n. 5,* 24, 2001.

Gao, W., S. Grand, W.S. Baldridge, D. Wilson, M. West, J. Ni, and R. Aster, Upper mantle convection beneath the central Rio Grande rift imaged by P and S wave tomography, *J. Geophys. Res., 109,* B03305, doi:10.1029/2003JB002743, 2004.

Humphreys, E.D., Post-Laramide removal of the Farallon slab, western United States, *Geology , 23, n. 11,* 987-990, 1995.

Kluth, C.F. and P.J. Coney, Plate tectonics of the Ancestral Rocky Mountains, *Geology, 9,* 10-15, 1981.

Langston, C.A., Corvallis, Oregon, Crustal and Upper Mantle Receiver Structure from Teleseismic P and S waves, *Bull. Seis. Soc. Am., 67,* 713-724, 1977.

Lee, C., Q. Yin, R.L. Rudnick, and S. B. Jacobsen, Preservation of ancient and fertile lithospheric mantle beneath the southwestern United States, *Nature, 411, n. 6833,* 69-73, 2001.

Li, A., K. M. Fischer, S. van der Lee, and M. E. Wysession, Crust and upper mantle discontinuity structure beneath eastern North America, *J. Geophys. Res., 107, no. B5,* 10.1029/2001JB000190, 2002.

Marshak, S., K. Karlstrom, and J.M. Timmons, Inversion of Proterozoic Extensional Faults: An Explanation for the pattern of Laramide and Ancestral Rockies Intracratonic Deformation, United States, *Geology, 28, n. 8,* 735-738, 2000.

Marshak, S., and T. Paulsen, Midcontinent U.S. fault and fold zones: A legacy of Proterozoic Intracratonic Extensional Tectonism?, *Geology, 24, n. 2,* 151-154, 1996.

McKenzie, D., Some remarks on the development of sedimentary basins, *Earth Planet. Sci. Lett., 40,* 25-32, 1978.

McMillan, N. J., Temporal and Spatial Magmatic Evolution of the Rio Grande Rift,*New Mexico Geological Society Guidebook, 49,* 107-116, 1998.

Morgan, P, W. Seager, and M. Golombek, Cenozoic Thermal, Mechanical and Tectonic Evolution of the Rio Gr ande Rift, *Jour. Geophys. Res., 91,* 6263-6276, 1986.

Mosher, S., Tectonic evolution of the southern Laurentian Grenville orogenic belt, *GSA Bulletin, 110, no. 11,* 1357-1375, 1998.

Olsen, K.H., G.R. Keller, and J.N. Stewart, Crustal structure along the Rio Grande Rift from seismic refraction profiles, in *Rio Grande Rift; tectonics and magmatism,* 127-143, 1979.

Olsen, K.H., W. S. Baldridge, and J. F. Callender, Rio Grande rift: an overview, *Tectonophysics, 143,* 119-139, 1987.

Perry, F.V., W. S. Baldridge, D. J. DePaolo, Chemical and isotopic evidence for lithospheric thinning beneath the Rio Grande rift, *Nature, 332,* 432-434, 1988.

Reed, J. C., Jr., T. T. Ball, G. L. Farmer, and W. B. Hamilton, A broader view, in *Precambrian: Conterminous U. S., The Geology of North America, C-2,* edited by J. C. Reed, Jr. and others, Geol. Soc. Amer., Boulder, Colo., 614-622, 1993.

Riter, J.C.A. and D. Smith, Xenolith constraints on the thermal history of the mantle below the Colorado Plateau, *Geology, 24, n. 3,* 267-270, 1996.

Roden, M.F., and N. Shimizu, Ion microprobe analyses bearing on the composition of the upper mantle beneath the Basin and Range and Colorado Plateau provinces, *J. Geophys. Res., 98,* 14091-14108, 1993.

Roden, M.F., and N. Shimizu, Trace element abundances in mantle-derived minerals which bear on compositional complexities in the lithosphere of the Colorado Plateau, *Chem. Geol., 165,* 283-305, 2000.

Roller, J.C., Crustal structure in the eastern Colorado Plateau province from seismic refraction measurements, *Bull. Seismol. Soc. Am., 55,* 107-119, 1965.

Seager, W.R., and P. Morgan, Rio Grande Rift in southern New Mexico, West Texas, and northern Chihuahua in *Rio Grande Rift; tectonics and magmatism,* 87-106, 1979.

Selverstone, J., A. Pun, K.C. Condie, Xenolithic evidence for Proterozoic crustal evolution beneath the Colorado Plateau, *Geol. Soc. Amer. Bull., 111, n. 4,* 590-606, 1999.

Sinno, Y.A., and G.R. Keller, A Rayleigh Wave Dispersion Study Between El Paso, Texas and Albuquerque, New Mexico, *J. Geophys. Res., 91, n. B6,* 6168-6174, 1986.

Sloss, L.L. editor, Sedimentary cover, North American Craton, U.S., *The Geology of North America, D-2*, 1988.

Smith, D., Insights into the evolution of the uppermost continental mantle from xenolith localities on and near the Colorado Plateau and regional comparisons, *J. Geophys. Res., 105, n. B7,* 16769-16781, 2000.

Smith, D., D. E. Moser, J. Connelly, K. Manser, and D. Schulze, U-Pb Zircon Ages of Eclogites, Garnetites, and Cenozoic Rock-Water Reactions in Proterozoic Mantle Below the Colorado Plateau, *GSA 2002 Annual Meeting Abstracts with Programs,* 2002.

Stewart, S. W. and L. C. Pakiser, Crustal structure in eastern New Mexico interpreted from the GNOME explosion, *Bull. Seismol. Soc. Am., 52,* 1017-1030, 1962.

Toppozada, T.R., Sanford, A.R., Crustal structure in central New Mexico interpretation from the Gasbuggy explosion, *Bull. Seismol. Soc. Am., 66,* 877-886, 1976.

Wendlandt, E., D. J. DePaolo, and W. S. Baldridge, Nd and Sr isotope chronostratigraphy of Colorado Plateau lithosphere: implications for magmatic and tectonic underplating of the continental crust, *Earth Planet. Sci. Lett., 116,* 23-43, 1993.

West, M., J. Ni, W.S. Baldridge, D. Wilson, R. Aster, W. Gao, and S. Grand, Crust and upper mantle shear wave structure of the southwest United States: Implications for rifting and support for high elevation, *J. Geophys. Res., 109,* B03309, doi:10.1029/2003JB002575, 2004.

Wernicke, B., Uniform Sense Normal Simple Shear of the Continental Lithosphere,*Canadian. Jour. Earth. Sci., 22,* 108-125, 1985.

Wilson, D., J. Leon, R. Aster, J. Ni, J. Schlue, S. Grand, S. Semken, S. Baldridge, and W. Gao, Broadband Seismic Background Noise at Temporary Seismic Stations Observed on a Region al Scale in the Southwestern United States, *Bull. Seismol. Soc. Amer., 92,* 3335-3341 (2002).

Zandt, G. and C.J. Ammon, Continental crust composition constrained by measurements of crustal Poisson's ratio, *Nature, 374,* 152-154, 9 March, 1995.

Zhu, L. and H. Kanamori, Moho depth variation in southern California from teleseismic receiver functions, *J. Geophys. Res., 105, n. B2,* 2969-2980, 2000.

CHAPTER 5

Lithospheric Structure of the Rio Grande Rift

[1]A modified version of this chapter has been submitted to *Nature*, Wilson, D., M. West, R. Aster, J. Ni, S. Grand, W. Gao, W.S. Baldridge, and S. Semken, in review, 2004

Abstract

A high resolution, regional, passive seismic experiment in the Rio Grande rift (RGR) region of the southwestern United States has produced new images of upper mantle velocity structure and crust-mantle topography. Synthesizing these results with geochemical and other geophysical evidence reveals highly symmetric lower-crustal and upper-mantle lithosphere extensional deformation, suggesting a pure-shear rifting mechanism for the RGR. Extension in the lower crust is distributed over a region four times the width of the rift's surface expression. We propose that the laterally distributed, pure shear extension is a combined effect of low strain rate and a regionally elevated geotherm at the time of rift initiation. Distributed extension in the lower crust and mantle has induced less concentrated vertical mantle upwelling and less vigorous small-scale convection than would have arisen from more localized deformation. The lack of focussed mantle upwelling may explain a deficit of rift-related volcanics in the RGR compared to other major rift systems such as the Kenya rift.

5.1 Introduction

Rifting has a profound influence on continental evolution, fundamentally controlling crustal thinning and continental breakup. The character of a continental rift depends on how lithospheric strain is accommodated. Possible strain configurations range between pure-shear and simple-shear end members. The pure shear model is characterized by ductilely deforming lower crust and mantle lithosphere and predicts symmetric thinning and a symmetric lithospheric cross section with respect to the rift axis (McKenzie, 1978). The simple-shear model is characterized by strain localization along a master or

sequence of low-angle (10° - 30° dip) detachment(s) that may span the entire lithosphere (Wernicke, 1985). A low-angle detachment predicts an asymmetric lithospheric cross-section, with greatest crustal thinning laterally offset from greatest mantle lithosphere thinning.

In both the simple- and the pure-shear models, extensional thinning of crust and mantle lithosphere produces local upwelling of warm asthenosphere to replace thinned lithosphere. Additional heat is released by adiabatic decompression, producing partial melting and rift-associated volcanism. The emplacement of advected warmer material creates lateral temperature gradients that can induce small-scale convection (Buck, 1986; Huismans et al., 2001). Small-scale convective cells may create significant additional horizontal stresses that further advance rifting, volcanism, and other lithosphere-scale deformation (Mutter et al., 1988; Huismans et al., 2001).

The simple- and pure-shear models offer distinct topographic, heat flow, gravity anomaly, and lithospheric velocity structural predictions. Ideally, it should be possible to distinguish between the models by the topographic expression of the rift, because the asymmetry of simple-shear deformation predicts asymmetry in rift flanks flexural uplift (Weissel and Karner, 1989), with greatest uplift offset laterally from the surface expression of the rift. Rift flank topography along the RGR (Figure 5.1) is in fact relatively symmetric about the rift axis, with variations of typically less than 1-2 km between adjacent rift flanks. However, the use of topography as a diagnostic may be significantly complicated by crustal composition and the fact that rifting has resulted in brittle deformation in the uppermost crust expressed as a series of asymmetric

grabens (Chapin and Cather, 1994; Olsen et al., 1987).

Similarly, the asymmetry of the simple-shear model predicts a complementary heat flow asymmetry (Buck et al., 1988). Heat flow measurements in the RGR region show a broad region of roughly symmetric high heat flow trending approximately along the rift axis (Russell and Snelson, 1994), consistent with pure-shear extension. However, regional heat flow values along the RGR and elsewhere may be significantly complicated by advective hydrothermal transport within the crust (Reiter et al., 1986).

5.2 Crust and Upper Mantle Structure

A diagnostic for assessing the existence of simple-shear detachment(s) is to image the location of maximum crustal thinning relative to the surface expression of the rift axis. We have constructed a new image of the crust-mantle boundary using receiver functions computed from teleseismic body waves recorded by the 950-km-long, 54-station LA RISTRA experiment (Wilson et al., 2002; Gok et al., 2003; Wilson et al., 2003; Gao et al., 2004; West et al., 2004; Wilson et al., 2004), a linear transect that crossed the RGR obliquely near 34.5° (Figure 5.1). Receiver function processing isolates P-to-S converted seismic phases generated by impedance discontinuities (Langston, 1977). Discontinuity images are constructed by migration and stacking of many receiver functions with different ray paths through the crust and mantle, recorded at many stations. LA RISTRA receiver function images (Figure 5.2) indicate crustal thickness ranging from 45 to 50 km beneath both the Colorado Plateau (stations NM34-UT54), and the Great Plains (TX01-NM20), with a rift-associated thinning to approximately 37 km centered beneath the RGR axis

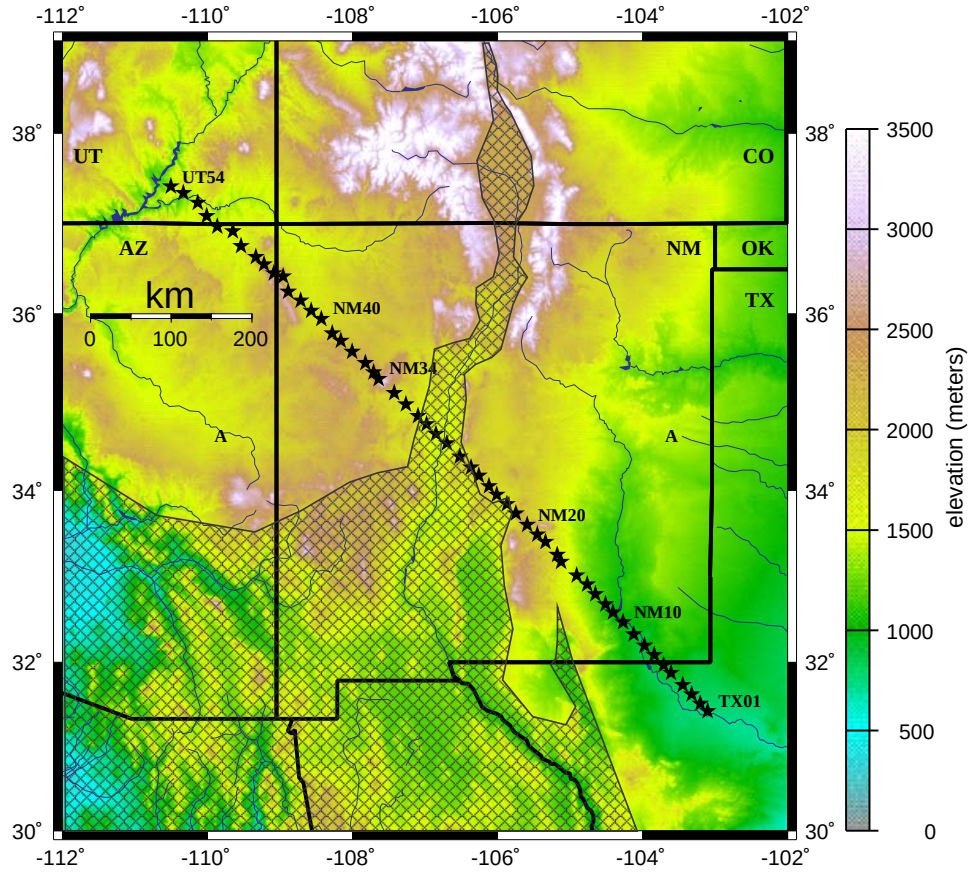

Figure 5.1: Elevation of the Rio Grande rift and surrounding region. The crosshatched pattern indicates the region of Cenozoic extension (Olsen et al, 1987). Stars indicate broadband seismic stations of the LA RISTRA experiment.

to within a few kilometers. These estimated crustal thicknesses are consistent with previous compilations of refraction surveys (Keller and Baldridge, 1999) across the RGR.

Using geologic constraints from previous seismic reflection work (Russel and Snelson, 1994), we modelled the predicted geometry of the base of the crust (Moho) and the base of the lithosphere resulting from the amount of extension seen at the surface in the southern Albuquerque - Belen basin (16.9 km of extension over 60 km; Figures 5.2, 5.3). The modelling technique (Weissel and Karner, 1989) takes into account the kinematics of lithospheric extension, the isostatic response to crust and lithospheric thinning, and the elastic response of the lithosphere (flexure). Extension by either east- or west-dipping simple shear (Figure 5.2a, 5.2b) predicts offset Moho upwarping that is significantly different than that observed, with the location of maximum crustal thinning offset laterally from the surface expression of the rift. The maximum misfit within 100 km of the rift axis between observed Moho depths and depths predicted by simple shear extension for 15°, 30°, and 45° east and west-dipping faults is greater than 6 km for each case. In contrast, modelling extension as pure shear (Figure 5.2c) produces Moho upwarp that is centered on the rift axis and is highly consistent with the observed Moho geometry. Assuming that extension in the lower crust takes place over the same lateral distance (60 km) as in the upper crust (LC:UC = 1), sharp localized crustal thinning can occur, up to approximately 15 km, which is much greater and more localized than that observed. By allowing model extension in the lower crust to be distributed over a greater lateral distance we obtain more broadly distributed crustal thinning that is a much better fit to the observed Moho upwarp. A LC:UC ratio of

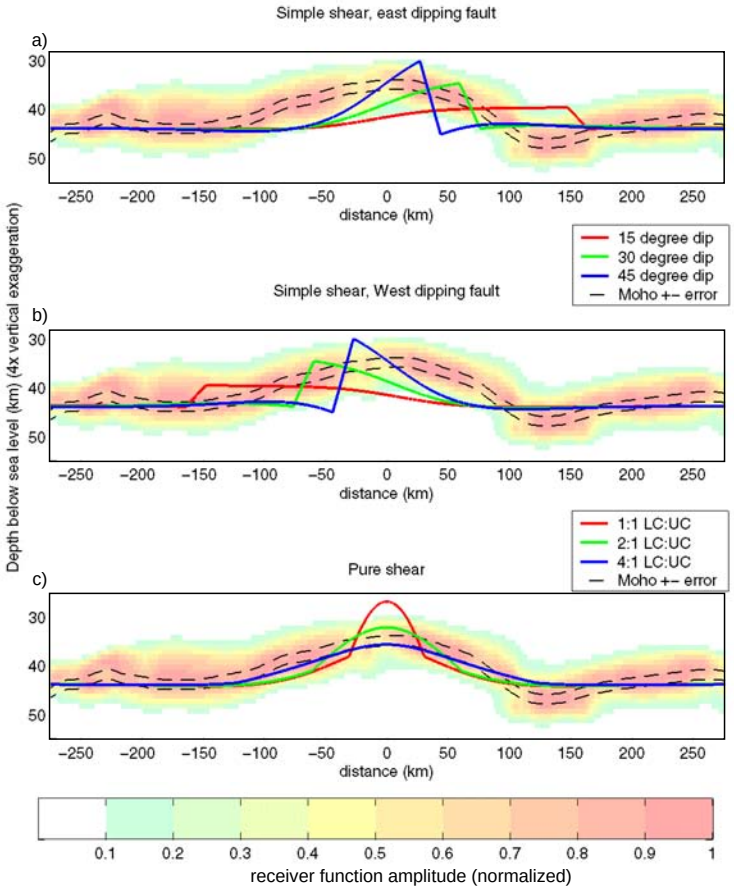

Figure 5.2: Modelled topography of the base of the crust predicted under simple shear extension for a) East-dipping faults and b) West-dipping faults with dips of 15:, 30:, and 45:, and c) from modelling pure shear extension, with the lateral distribution of lower crustal extension relative to upper crustal extension (LC:UC) ranging from 1:1 to 4:1. For each LC:UC ratio, the volume of crustal thinning is the same. The shape of upper crustal thinning used for pure shear modelling is a truncated Gaussian, scaled to fit the dimensions of the Albuquerque - Belen RGR basin transacted by the experiment. Underlying colours show positive migrated seismic receiver function amplitudes projected onto an east-west, rift-perpendicular profile, defining the observed base of the crust. Dashed lines represent plus and minus one standard deviation crustal thickness (1/4 wavelength, or about 1.5 km at Moho depths) for the migrated receiver function image.

4:1 (lower crustal extension over 240 km laterally) gives the smallest maximum misfit of 1.8 km within 100 km of the rift.

An observation that complements the crustal thinning profile is the lithospheric thinning profile and its rift axis symmetry. Gravity data suggest thinning of the lithosphere near the rift axis (Cordell et al., 1991), and previous regional teleseismic experiments (Parker et al., 1984; Davis, 1991; Slack et al., 1996) have noted increased teleseismic delay times, suggestive of an elevated lithosphere/asthenosphere boundary. In the central RGR, the elevated lithosphere/asthenosphere boundary is centered beneath the rift, but in the southern RGR the anomaly fans out to the southwest (Slack et al., 1996) as the RGR transitions into the Basin and Range province, a region of considerably greater Cenozoic extension. Geochemical analysis of volcanic rocks in the RGR region suggests asthenospheric ("depleted") magmatic source zones near the rift axis and lithospheric ("enriched") source zones on the outer flanks, further supporting thinned lithosphere roughly beneath the rift axis (Perry et al., 1988; Baldridge et al., 1991; McMillan, 1998).

While each of the above lines of evidence suggest lithospheric thinning is centered approximately beneath the rift axis, this study provides the first simultaneous view of the crust, Moho and upper mantle. Inversion of LA RISTRA surface wave dispersion data indicates that shear velocities within 100 km of the rift axis are uniformly slow throughout the crust (Figure 5.3). These velocities are likely the result of elevated temperatures and the possible presence of melt (West et al, 2004). The symmetry of the low velocities and inferred thermal structure is challenging to explain with asymmetric crustal processes.

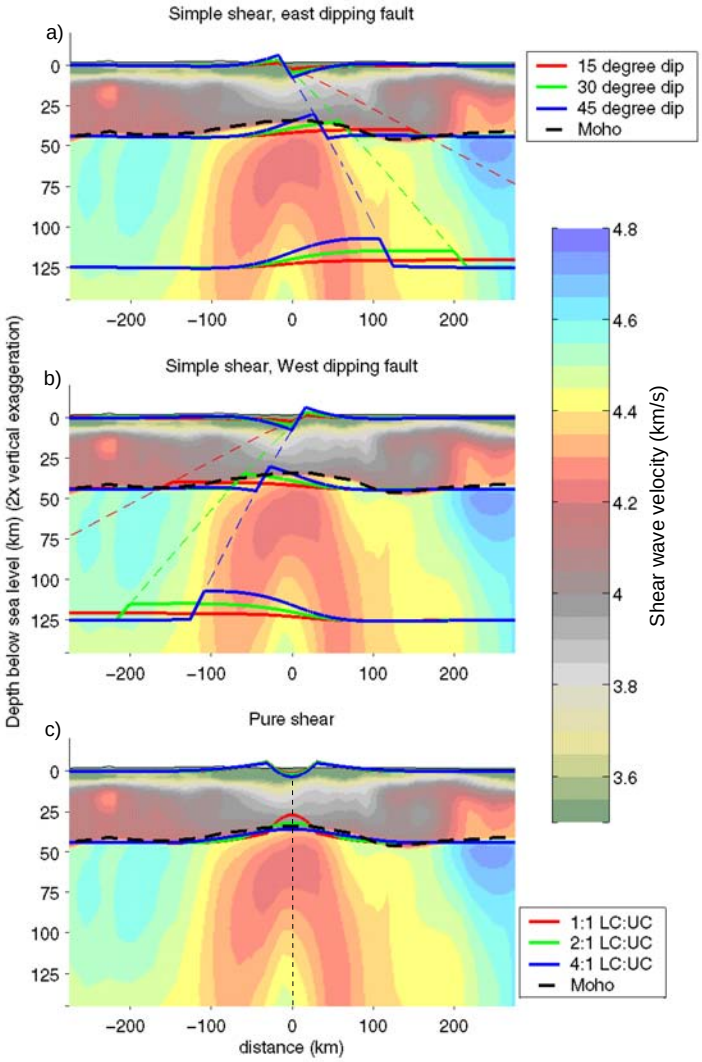

Figure 5.3: Lithospheric-scale cross-section in the identical projection used in Figure 5.2, showing predicted surface topography and uplift of the Moho and lithosphere topography from modelling shown in Figure 2. Underlying colours depict crust and upper-mantle shear-wave velocities determined from surface-wave phase velocity inversion (West et al., 2004). Horizontal resolution of the surface wave velocity model is 55 km in the crust and 105 km in the upper mantle. Error (1 standard deviation) in the velocity model is 0.09 km/s above, and 0.07 km/s below the Moho. The vertical dotted line in c) denotes the rift axis. The centering of crust and mantle low velocities on the rift axis, and the symmetry of the low velocities, indicate symmetric mantle extension about the rift axis.

Upper mantle shear wave velocities (Figure 5.3) reveal a transition between high velocities beneath the Great Plains and Colorado Plateau and a broad region of low velocities beneath the RGR. A similar pattern of low velocities centered beneath the rift is observed in P- and S-body-wave tomography (Gao et al., 2004). Modelled lithospheric upwarp due to simple shear extension (Figure 5.3a,b) shows that the predicted location of maximum lithospheric upwarp for fault dips of 15°, 30°, and 45° is offset from the rift axis by approximately 300, 180, and 100 km respectively for a reference lithospheric thickness of 125 km. Although the amount of lateral offset of maximum lithospheric upwarp depends on the reference lithospheric thickness used in modelling, simple shear extension (Figure 5.3a,b) predicts significant and observable offsets for a range of lithospheric thicknesses. Lithospheric thinning from pure shear extension, in contrast, predicts upwarp that is centered on the rift axis and is aligned with the observed rift-centered low shear wave velocity (Figure 5.3c). The low velocities beneath the RGR are up to 10% less than in the adjacent upper mantle. Only a few percent of this variation can be explained by compositional variation (West et al., 2004). This magnitude of variation also cannot be attributed to anisotropy because shear wave splitting results (Gok et al., 2003) indicate that the anisotropic character of the rift is not significantly different than in adjacent regions. Elevated temperatures, partial melting, lithospheric thinning, or a combination of these are thus the most likely causes of the region of low velocities. Whether these features drive rifting, result from rifting, or represent some intermediate state, is a subject of ongoing debate (Olsen et al., 1987). Regardless, the anomalous lithosphere centered beneath the rift is inconsistent with simple-shear dominated extension. The zone of low velocities

is furthermore considerably wider than the minimum horizontal resolution of 150 km (or 105 km, when projected to an east-west cross section) indicating that mantle lithosphere deformation is laterally distributed (Figure 5.3c), as would be expected for weak lithosphere deforming predominantly by ductile, pure-shear extension.

5.3 Discussion and Conclusions

Major factors controlling whether lithosphere will deform by localized brittle deformation, or by distributed ductile deformation, as seen here in the RGR, are lithospheric rheology, temperature, and strain rate (Morgan et al., 1986). Higher temperatures and low strain rates are conducive to ductile deformation. A regionally elevated geotherm during rift initiation (Morgan et al., 1986) is suggested by widespread regional ignimbrite volcanism around 30 Ma. This event, likely caused by the foundering of the subducting Farallon slab (Humphreys, 1995), may have significantly weakened the lithosphere beneath the RGR, thus favouring distributed ductile deformation. Cenozoic strain rates in the central RGR are also relatively low, with only 18-28% total extension (16.9 km extension over 60 km in the southern Albuquerque-Belen basin) during the last 30 Ma (Chapin and Cather, 1994; Russell and Snelson, 1994). Strain accumulation may have been concentrated in two distinct periods, 30-18 Ma and 10-5 Ma (Chapin and Cather, 1994). Even so, this suggests RGR formational strain rates of only 10^{-16} to 10^{-15} s^{-1} (0.56 to 1 mm/yr). This low strain rate, along with elevated temperature, may have enabled the lithosphere to deform ductilely, producing a symmetric region of laterally distributed pure-shear deformation. While volumes of lithospheric thinning and

upwelling mantle are the same for distributed versus concentrated deformation, we suggest that the increased lateral distribution of lithospheric deformation may have resulted in less concentrated vertical mantle upwelling. The lateral temperature gradients produced by distributed extension are smaller than would have been produced by concentrated extension (Mutter et al., 1988), inducing less vigorous small-scale convection and thus limiting the amount of heat delivered to the shallow rift. As a result, the RGR has experienced relatively small volumes of rift-related volcanism when compared to other rift systems (e.g., RGR extrusives are only 5-10% of the Kenya rift) (Olsen et al., 1987; Keller et al., 1991; Dunbar and Sawyer, 1988).

References

Baldridge, W.S., F. Perry, D. Vaniman, L. Nealey, B. Leavy, A. Laughlin, P. Kyle, Y. Bartov, G. Steinitz, and E. Gladney, Middle to Late Cenozoic Magmatism of the Southeastern Colorado Plateau and Central Rio-Grande Rift (New-Mexico and Arizona, USA) - A Model for Continental Rifting, *Tectonophysics, 197,* 327-354, 1991.

Buck, R.W., Small-scale convection induced by passive rifting: the cause for uplift of rift shoulders, *Earth Planet. Sci. Letts., 77,* 362-372, 1986.

Buck, R.W., F. Martinez, M. S. Steckler, J.R. Cochran, Thermal Consequences of Lithospheric Extension: Pure and Simple, *Tectonics, 7,* 213-234, 1988.

Chapin, C.E. and S.M. Cather, Tectonic Setting of the Axial Basins of the Northern and Central Rio Grande Rift, *Geol. Soc. Amer. Special Paper 291,* 5-24, 1994.

Cordell, L., Y.A. Zorin, and G.R. Keller, The Decompensative Gravity Anomaly and Deep Structure of the Region of the Rio-Grande Rift, *Jour. Geoph. Res., 96,* 6557-6568, 1991.

Davis, P.M., Continental Rift Structures and Dynamics with Reference to Teleseismic Studies of the Rio-Grande and East-African Rifts, *Tectonophysics,*

197, 309-325, 1991.

Dunbar, J., and D. Sawyer, Continental Rifting at Pre-existing lithospheric weaknesses, *Nature, 333,* 450-452, 1988.

Gao, W., S. Grand, W.S. Baldridge, D. Wilson, M. West, J. Ni, and R. Aster, Upper mantle convection beneath the central Rio Grande rift imaged by P and S wave tomography, *J. Geophys. Res., 109,* B03305, doi:10.1029/2003JB002743, 2004.

Gok, R., J.F. Ni, E. Sandvol, D. Wilson, W.S. Baldridge, R. Aster, M. West, S. Grand, W. Gao, F. Tilmann, and S. Semken, Shear wave splitting and mantle flow beneath LA RISTRA, *Geophys. Res. Lett., 30,* 1614, doi:10.1029/2002GL016616, 2003.

Huismans, R.S., Y.Y. Podladchikov, and S. Cloetingh, Transition from passive to active rifting: Relative importance of asthenospheric doming and passive extension of the lithosphere, *Jour. Geophys. Res., 106,* 11271-11291, 2001.

Humphreys, D., Post-Laramide removal of the Farallon slab, western United States, *Geology, 23,* 987-990, 1995.

Keller, G.R. et al., A Comparative Study of the Rio Grande and Kenya Rifts, *Tectonophysics, 197,* 355-371, 1991.

Keller, G. R., and W. S. Baldridge, The Rio Grande rift: A geological and geophysical review, *Rocky Mountain Geology, 34,* 131-148, 1999.

Langston, C.A., Corvallis, Oregon, Crustal and Upper Mantle Receiver Structure from Teleseismic P and S waves, *Bull. Seis. Soc. Am., 67,* 713-724, 1977.

McKenzie, D., Some remarks on the development of sedimentary basins, *Earth Planet. Sci. Lett., 40,* 25-32, 1978.

McMillan, N. J., Temporal and Spatial Magmatic Evolution of the Rio Grande Rift, *New Mexico Geological Society Guidebook, 49,* 107-116, 1998.

Morgan, P, W. Seager, and M. Golombek, Cenozoic Thermal, Mechanical and Tectonic Evolution of the Rio Grande Rift, *Jour. Geophys. Res., 91,* 6263-6276, 1986.

Mutter, J., W.R. Buck, and C. Zehnder, Convective Partial Melting, 1, A Model for the Formation of Thick Basaltic Sequences During the Initiation of Spreading, *Jour. Geophys. Res., 93,* 1031-1048, 1988.

Olsen, K.H., W. S. Baldridge, and J. F. Callender, Rio Grande rift: an overview, *Tectonophysics, 143,* 119-139, 1987.

Parker, E.C., P.M. Davis, J.R. Evans, H.M. Iyer, and K.H. Olsen, Upwarp of anomalous asthenosphere beneath the Rio Grande rift, *Nature, 312,* 354-356, 1984.

Perry, F.V., W.S. Baldridge, and D.J. DePaolo, Chemical and Isotopic Evidence for Lithospheric Thinning Beneath the Rio-Grande Rift, *Nature, 332,* 432-434, 1988.

Reiter, M., R.E. Eggleston, B.R. Broadwell, J. Minier, Estimates of terrestrial heat flow from deep petroleum tests along the Rio Grande Rift in central and southern New Mexico, *Jour. Geophys. Res., 91,* 6225-6245, 1986.

Russell, L. R. and S. Snelson, Structural style and tectonic evolution of the Albuquerque Basin segment of the Rio Grande Rift, New Mexico, U.S.A., in Interior rift basins, S. Landon, ed., *AAPG Memoir 59,* 205-258, 1994.

Slack, P.D., P. davis, W.S. Baldridge, K.H. Olsen, A. Glahn, U. Achauer, and W. Spence, The upper mantle structure of the central Rio Grande Rift region from teleseismic P- and S- wave travel time delays and attenuation, *J. Geophys. Res., 101,* 16,003-16,023, 1996.

Weissel, J.K., and G.D. Karner, Flexural Uplift of Rift Flanks Due to Mechanical Unloading of the Lithosphere During Extension, *J. Geophys. Res., 94,* 13919-13950, 1989.

Wernicke, B., Uniform Sense Normal Simple Shear of the Continental Lithosphere, *Canadian. Jour. Earth. Sci., 22,* 108-125, 1985.

West, M., J. Ni, W.S. Baldridge, D. Wilson, R. Aster, W. Gao, and S. Grand, Crust and upper mantle shear wave structure of t he southwest United States: Implications for rifting and support for high elevation, *J. Geophys. Res., 109,* B03309, do i:10.1029/2003JB002575, 2004.

Wilson, J. Leon, R. Aster, J. Ni, J. Schlue, S. Grand, S. Semken, S. Baldridge, and W. Gao, Broadband Seismic Background Noise at Temporary Seismic Stations Observed on a Regional Scale in the Southwestern United States, *Bull. Seismol. Soc. Amer., 92,* 3335-3341 2002.

Wilson, D., R. Aster, and the RISTRA Team, Imaging Crust and Upper Mantle Seismic Structure in the Southwestern United States Using Teleseismic Receiver Functions, *The Leading Edge, 22,* 232-237, 2003.

Wilson, D., R. Aster, J. Ni, S. Grand, M. West, W. Gao, W.S. Baldridge, and S. Semken, Imaging the Seismic Structure of the Crust and Upper Mantle Using Receiver Functions, Part 2: Application to the LA RISTRA Network, in preparation, JGR, 2004.

Acknowledgments

We thank G.R. Keller and two anonymous reviewers for helpful comments. Field and data handling assistance was provided by the IRIS PASSCAL Instrument Center at the New Mexico Institute of Mining and Technology (NMT). This research supported by NSF grants EAR 9707190 and EAR 9706094, the Los Alamos National Laboratory Institute for Geophysics and Planetary Physics, the New Mexico State University Arts and Sciences Research Center, and the NMT Geophysical Research Center. Persons wishing to conduct geological investigations on the Navajo Nation must first apply for and receive a permit from the Navajo Nation Minerals Department, PO Box 1910, Window Rock, Arizona, 86515, 928-871-6587.

APPENDIX A

LA RISTRA station and data specifications

LA RISTRA stations along the main transect of 54 stations were each equiped with a Strekeisen STS-2 broadband seismometer which has a low corner frequency of .00833 Hz, or 120 seconds. The three off-line stations (MB01, MB04, and MB05) were each equiped with a Guralp CMG-3T broadband seismometer which also has a low corner frequency of .00833 Hz. Data from the three off-line stations were not used in this study. All stations were continuously recording at 20 samples/second using either model 72A-07 or model 72A-08 data acquisition systems (DAS) from Refraction Technology Inc. (RefTek; http://www.reftek.com). Table A.1 contains a detailed list of LA RISTRA station specifications including location, elevation, dates of operation, and DAS model. LA RISTRA data are now freely available from the Incorporated Research Institutions for Seismology (IRIS) Data Management Center (DMC) (http://www.iris.edu), with network code XM for years 1999-2001. To convert to ground velocity a conversion factor of 1.3560e-09 (m/s)/count must be used for the 72A-07 DAS, and a conversion factor of 1.271e-9 (m/s)/count for the 72A-08 DAS. This conversion factor includes the seismometer sensitivity which is 1500 V/(m/s) for both the STS-2 and CMG-3T. The bibliography for this section contains a comprehensive list of LA RISTRA related publications and abstracts to date (May 2004). Additional information on LA RISTRA data and research results can be found at http://www.ees.nmt.edu/Geop/Ristra/ristra.html.

Table A.1: LA RISTRA Station Specifications

Station	Latitude	Longitude	Elevation (m)	Deployment Dates	DAS
TX01	31.4247	-103.1040	750	1999-09-11 2001-05-16	72A-08
TX02	31.5140	-103.2050	765	1999-09-11 2000-12-31	72A-08
TX03	31.6230	-103.3230	831	1999-09-01 2001-05-16	72A-08
TX04	31.7330	-103.4460	833	1999-09-11 2001-03-11	72A-08
TX05	31.8790	-103.6070	873	1999-09-11 2001-05-16	72A-08
TX06	31.9670	-103.7070	899	1999-10-30 2001-03-11	72A-08
NM07	32.0854	-103.8400	966	1999-09-11 2001-03-25	72A-08
NM08	32.1967	-103.9710	886	1999-09-11 2001-03-11	72A-08
NM09	32.3290	-104.1210	893	1999-09-11 2001-05-15	72A-08
NM10	32.4710	-104.2710	929	1999-09-12 2001-03-11	72A-08
NM11	32.5838	-104.4090	974	1999-09-11 2001-05-15	72A-08
NM12	32.6800	-104.5100	1066	1999-09-11 2001-03-12	72A-08
NM13	32.8003	-104.6520	1177	1999-09-13 2001-05-16	72A-08
NM14	32.9100	-104.7640	1219	1999-09-10 2001-03-12	72A-08
NM15	33.0150	-104.9090	1342	1999-09-13 2001-05-16	72A-08
NM16	33.1757	-105.1250	1625	1999-09-12 2001-03-12	72A-08
NM17	33.2570	-105.1790	1705	1999-09-18 2001-05-15	72A-08
NM18	33.4046	-105.3400	1624	1999-09-13 2001-05-15	72A-08
NM19	33.4900	-105.4500	2028	1999-10-01 2000-07-06	72A-08
NM20	33.6047	-105.5940	2034	1999-09-16 2001-03-10	72A-08
NM21	33.7328	-105.7450	2000	2000-05-25 2001-05-01	72A-08
NM22	33.8403	-105.8690	1691	1999-10-01 2001-03-04	72A-07
NM23	33.9499	-106.0130	1813	1999-10-02 2001-05-01	72A-07
NM24	34.0469	-106.1200	1874	1999-10-02 2001-01-31	72A-08
NM25	34.1669	-106.2600	1933	1999-07-05 2001-05-02	72A-07
NM26	34.2622	-106.3640	1854	1999-07-06 2001-03-05	72A-07
NM27	34.3857	-106.5240	1870	1999-07-06 2001-05-02	72A-08
NM28	34.5399	-106.7010	1484	1999-07-06 2001-03-03	72A-07
NM29	34.6470	-106.8490	1561	1999-07-08 2001-03-04	72A-08

Table A.1 continued

Station	Latitude	Longitude	Elevation (m)	Deployment Dates	DAS
NM30	34.7541	-106.9800	1515	1999-09-15 2001-03-03	72A-07
NM31	34.8478	-107.0990	1676	1999-11-10 2001-05-02	72A-07
NM32	34.9805	-107.2640	1685	1999-09-15 2000-12-28	72A-07
NM33	35.1109	-107.4230	2094	1999-05-22 2001-05-03	72A-08
NM34	35.2690	-107.6410	2735	1999-08-28 2000-09-05	72A-08
NM35	35.3448	-107.7070	2133	1999-08-05 2001-05-04	72A-08
NM36	35.4506	-107.8200	2176	1999-08-05 2001-03-07	72A-08
NM37	35.5779	-108.0050	2254	1999-08-04 2001-05-09	72A-08
NM38	35.6998	-108.1630	2077	1999-07-28 2000-11-16	72A-08
NM39	35.7853	-108.2780	1949	1999-07-28 2001-05-09	72A-08
NM40	35.9450	-108.4290	1796	1999-07-07 2001-03-06	72A-08
NM41	36.0353	-108.5700	1718	1999-07-29 2001-05-09	72A-08
NM42	36.1485	-108.7170	1794	1999-07-28 2001-03-18	72A-08
NM43	36.2495	-108.8870	1991	1999-11-15 2001-03-18	72A-08
NM44	36.4215	-108.9580	1921	1999-07-28 2001-05-09	72A-08
AZ45	36.4543	-109.0840	2683	1999-08-11 2000-10-21	72A-08
AZ46	36.5569	-109.2190	2009	1999-07-29 2001-05-09	72A-08
AZ47	36.6352	-109.3340	1752	1999-07-30 2001-03-17	72A-08
AZ48	36.7598	-109.5390	1664	1999-08-10 2001-05-10	72A-08
AZ49	36.9233	-109.6490	1512	1999-07-30 2001-03-16	72A-08
AZ50	36.9762	-109.8640	1469	1999-07-29 2001-05-10	72A-08
UT51	37.0900	-110.0090	1498	1999-07-29 2001-03-16	72A-08
UT52	37.2363	-110.1360	1671	1999-07-29 2001-05-10	72A-08
UT53	37.3460	-110.3310	1291	1999-11-13 2001-03-17	72A-08
UT54	37.4187	-110.5060	1439	1999-11-14 2001-03-17	72A-08
MB01	33.3363	-106.0339	1446	2000-03-25 2001-05-01	72A-08
MB04	34.0738	-106.9201	1414	1999-07-01 1999-11-09	72A-07
MB04B	34.0709	-106.9422	1489	2000-03-08 2001-05-25	72A-07
MB05	34.6636	-108.0113	2143	2000-03-18 2000-06-25	72A-08

References

Papers:

Wilson, D., R. Aster, J. Ni, S. Grand, M. West, W. Gao, W.S. Baldridge, and S. Semken, Imaging the Seismic Structure of the Crust and Upper Mantle Using Receiver Functions, Part 1: Methods, in preparation, JGR, 2004.

Wilson, D., R. Aster, J. Ni, S. Grand, M. West, W. Gao, W.S. Baldridge, and S. Semken, Imaging the Seismic Structure of the Crust and Upper Mantle Using Receiver Functions, Part 2: Application to the LA RISTRA Network, in preparation, JGR, 2004.

Wilson D., M. West, R. Aster, J. Ni, W. Gao, S. Grand, W.S. Baldridge, S. Semken, Lithospheric Structure of the Rio Grande Rift, Nature, in review, 2004.

Gao, W., S. Grand, W.S. Baldridge, D. Wilson, M. West, J. Ni, and R. Aster, Upper mantle convection beneath the central Rio Grande rift imaged by P and S wave tomography, J. Geophys. Res., 109, B03305, doi:10.1029/2003JB002743, 2004.

West, M., J. Ni, W.S. Baldridge, D. Wilson, R. Aster, W. Gao, and S. Grand, Crust and upper mantle shear wave structure of the southwest United States: Implications for rifting and support for high elevation, J. Geophys. Res., 109, B03309, doi:10.1029/2003JB002575, 2004.

Wilson, D., R. Aster, and the RISTRA team Imaging Crust and Upper Mantle Seismic Structure in the Southwestern United States Using Teleseismic Receiver Functions, The Leading Edge, 22, n. 3, 232-237, 2003.

Gok, R., J.F. Ni, E. Sandvol, D. Wilson, W.S. Baldridge, R. Aster, M. West, S. Grand, W. Gao, F. Tilmann, and S. Semken, Shear wave splitting and mantle flow beneath LA RISTRA, Geophys. Res. Lett., 30, n. 12, 1614, doi:10.1029/2002GL016616, 2003.

Wilson, D., Leon, J., Aster, R., Ni, J., Grand, S., Semken, S., Baldridge, S., Broadband Seismic Background Noise at Temporary Seismic Stations Observed on a Regional Scale in the Southwestern United States, Bull. Seismol. Soc. Amer., 92, n. 8, 3335, 2003.

Abstracts:

Wilson, D., R. Aster, M. West, J. Ni, W. Gao, S. Grand, W.S. Baldridge, and S. Semken, Results from the LA RISTRA Seismic Array: Implications for the Earthscope Flexible Seismometer Array, Seism. Soc. Meeting Abstracts, Seism. Res. Letts., 75, n. 2, 2004.

Adams, D., M. West, and J. Ni, Pn Tomography at the Intersection of the Rio Grande Rift and Jemez Lineament EOS Trans. AGU, 84(46), Fall Meet. Suppl., Abstract S31E-0815, 2003.

Gao, W., S. Grand, W.S. Baldridge, D. Wilson, M. West, J. Ni, and R. Aster, Convection Beneath the Rio Grande Rift and Surrounding Regions Deduced From Tomographic Seismic Images , EOS Trans. AGU, 84(46), Fall Meet. Suppl., Abstract S31E-0810, 2003.

Wilson D., M. West, R. Aster, J. Ni, W. Gao, S. Grand, W.S. Baldridge, S. Semken, Lithospheric and Upper Mantle Structure of the Rio Grande Rift: Implications for Pure Shear Extension, EOS Trans. AGU, 84(46), Fall Meet. Suppl., Abstract S22A-0420, 2003.

Wilson, D., R. Aster, J. Ni, M. West, S. Grand, W. Gao, W.S. Baldridge, and S. Semken, Seismic Structure of the Lithosphere in the Southwestern United States Using Receiver Functions, Seism. Soc. Meeting Abstracts, Seism. Res. Letts., 74, n. 2, 2003.

Gao, W., S. Grand, M. West, R. Gok, J. Ni, D. Wilson, R. Aster, J. Schlue, W.S. Baldridge, and S. Semken, Mantle Dynamics Beneath the Rio Grande Rift and Colorado Plateau, Eos Trans. AGU, 83(47), Fall Meet. Suppl., Abstract S61A-1115, 2002.

Ni, J., R. Gok, and E. Sandvol, Shear Wave Splitting and Mantle Flow Beneath the Ristra Array, Eos Trans. AGU, 83(47), Fall Meet. Suppl., Abstract S61A-1114, 2002.

West, M., J. Ni, D. Wilson, R. Aster, S. Grand, W. Gao, R. Gok, W.S. Baldridge, S. Semken, and J. Schlue, Structure of the Uppermost Mantle Beneath the RISTRA Array From Surface Waves, Eos Trans. AGU, 83(47), Fall Meet. Suppl., Abstract S61A-1116, 2002.

Wilson, D., R. Aster, J. Ni, S. Grand, M. West, R. Gok, W. Gao, J. Schlue, W.S. Baldridge, S. Semken, Seismic Structure of the Lithosphere in the Southwestern United States Using Receiver Functions, Eos Trans. AGU, 83(47), Fall Meet. Suppl., Abstract S61A-1113, 2002.

Wilson, D., R. Aster, J. Ni, J. Schlue, S. Grand, W.S. Baldridge, S. Semken, W. Gao, Crust and Upper Mantle Structure in the Southwestern United States beneath a Broadband PASSCAL Array, IRIS Consortium 14th Annual Workshop, 2002.

Wilson, D., R. Aster, J. Schlue, J. Ni, S. Grand, W. Gao, S. Baldrudge, and S. Semken, Crust and Upper Mantle Structure in the Southwestern United States Using Teleseismic Receiver Functions Seism. Soc. Meeting Abstracts, Seism. Res. Letts., 73, n. 2, 2002.

Gao, W., S. Grand, J. Ni, R. Aster, D. Wilson, J. Schlue, W.S. Baldridge, S. Semken, and E. Matzel, Mantle Seismic Structure beneath the Colorado Plateau, Rio Grande Rift and Great Plains from Seismic Tomography Eos Trans. AGU, 82(47), Fall Meet. Suppl., Abstract S21F-07, 2001.

Matzel, E., S. Grand, J. Ni, and R. Aster, The seismic structure of the upper mantle beneath the northwestern United States Eos Trans. AGU, 82(47), Fall Meet. Suppl., Abstract S21F-08, 2001.

Wilson, D., Aster, R., Ni, J., Schlue, J., Grand, S., Baldridge, S., Semken, S., Gao, W., Crust and upper mantle structure of the Colorado plateau-Rio Grande rift-Great Plains transect using teleseismic receiver functions, Eos Trans. AGU, 82(47), Fall Meet. Suppl., Abstract S21F-09, 2001.

Wilson, D., Aster, R., Ni, J., Grand, S., Schlue, J., Semken, S., Baldridge, S., Crust and upper mantle structure of the Colorado Plateau-Rio Grande rift transition zone using teleseismic receiver functions from a broadband PASSCAL array, IRIS Consortium 13th Annual Workshop, Jackson, WY, June 6-9, 2001.

Rosca, A., Wilson, D., Tilmann, F. Leon, J., Rapine, R., Matzel, E., Simmons, N., Blackhorse, A., Ni, J., Aster, R., Grand, S., Schlue, J., Baldridge, S., Semken, S., A crustal low velocity zone under the Colorado Plateau - Rio Grande Rift transition zone, EOS Trans AGU, 81 (48), Abstract T22B-07, 2000.

APPENDIX B

LA RISTRA velocity models

Table B.1: RISTRA velocity models

Station	Vp (km/s)	Crustal Thickness Estimate (km)	Final Crustal Thickness (km)	Vp/Vs Estimate	Final Vp/Vs
TX01	6.33	0	45.8	0	1.75
TX02	6.32	0	45.8	0	1.75
TX03	6.31	46.5 ± 3.6	45.8	1.74 ± 0.04	1.75
TX04	6.30	48.6 ± 2.8	45.4	1.77 ± 0.04	1.75
TX05	6.27	47.5 ± 3.1	43.9	1.72 ± 0.05	1.75
TX06	6.25	38.7 ± 1.9	42.3	1.75 ± 0.04	1.75
NM07	6.22	41.1 ± 2.0	40.4	1.73 ± 0.04	1.75
NM08	6.21	41.8 ± 2.6	39.9	1.77 ± 0.05	1.74
NM09	6.21	43.0 ± 3.0	40.7	1.76 ± 0.06	1.74
NM10	6.22	43.2 ± 3.5	42.2	1.74 ± 0.07	1.74
NM11	6.27	43.1 ± 2.6	42.9	1.75 ± 0.05	1.73
NM12	6.27	42.9 ± 2.3	43.1	1.75 ± 0.06	1.73
NM13	6.27	43.8 ± 3.0	43.2	1.75 ± 0.04	1.74
NM14	6.27	42.6 ± 5.2	44.0	1.71 ± 0.08	1.74
NM15	6.29	0	47.3	0	1.75
NM16	6.28	50.4 ± 4.3	47.6	1.77 ± 0.07	1.75
NM17	6.28	46.3 ± 2.8	47.4	1.79 ± 0.07	1.75
NM18	6.26	45.6 ± 2.7	46.2	1.79 ± 0.04	1.76
NM19	6.26	42.8 ± 3.2	45.5	1.79 ± 0.06	1.76
NM20	6.24	42.3 ± 2.7	43.8	1.79 ± 0.07	1.77
NM21	6.23	42.9 ± 3.0	41.9	1.78 ± 0.09	1.77
NM22	6.21	0	40.1	0	1.78
NM23	6.20	39.0 ± 2.3	38.8	1.75 ± 0.06	1.78
NM24	6.19	38.1 ± 1.8	37.9	1.79 ± 0.05	1.78
NM25	6.18	36.9 ± 3.1	36.7	1.80 ± 0.06	1.78
NM26	6.16	0	35.8	0	1.78
NM27	6.15	0	34.9	0	1.78

Crustal thickness and Vp/Vs estimates were determined by receiver function phase moveout analysis. An estimate of 0 indicates a solution could not be found. Final crustal thickness and Vp/Vs were determined by picking crustal depth from migrated receiver function images. Velocity models given in this table are also plotted in Figure 4.5.

Table B.2 continued.

Station	Vp (km/s)	Crustal Thickness Estimate (km)	Final Crustal Thickness (km)	Vp/Vs Estimate	Final Vp/Vs
NM28	6.14	0	34.5	0	1.78
NM29	6.14	32.6 ± 2.8	35.4	1.76 ± 0.07	1.78
NM30	6.14	0	36.8	0	1.78
NM31	6.15	35.0 ± 3.3	38.1	1.78 ± 0.06	1.78
NM32	6.10	38.9 ± 3.6	39.6	1.79 ± 0.08	1.77
NM33	6.05	41.5 ± 2.7	41.3	1.80 ± 0.05	1.77
NM34	6.10	0	43.7	0	1.76
NM35	6.13	45.3 ± 2.1	43.8	1.75 ± 0.05	1.76
NM36	6.16	46.7 ± 2.3	45.2	1.78 ± 0.03	1.76
NM37	6.19	48.2 ± 3.8	46.7	1.77 ± 0.07	1.76
NM38	6.21	0	47.4	0	1.76
NM39	6.23	0	48.2	0	1.75
NM40	6.25	46.1 ± 2.1	48.8	1.78 ± 0.04	1.75
NM41	6.26	0	48.7	0	1.75
NM42	6.27	51.9 ± 3.3	48.3	1.72 ± 0.05	1.75
NM43	6.26	0	46.1	0	1.75
NM44	6.26	0	44.5	0	1.75
AZ45	6.27	0	44.1	0	1.75
AZ46	6.29	0	43.4	0	1.75
AZ47	6.31	45.6 ± 2.5	43.7	1.74 ± 0.04	1.75
AZ48	6.35	0	47.2	0	1.75
AZ49	6.38	48.9 ± 4.1	49.1	1.77 ± 0.06	1.75
AZ50	6.44	0	49.5	0	1.75
UT51	6.49	0	49.5	0	1.75
UT52	6.49	45.0 ± 4.5	48.6	1.72 ± 0.05	1.75
UT53	6.47	46.0 ± 3.1	45.8	1.74 ± 0.05	1.75
UT54	6.46	44.0 ± 2.6	45.4	1.77 ± 0.07	1.75

APPENDIX C

Data Processing Software

The software used for downloading LA RISTRA seismic data from the Incorporated Research Institutions for Seismology (IRIS) Data Management Center (DMC) is freely available from the DMC website (http://www.iris.edu). IRIS programs used for downloading and converting data include WEED (Windowed Extraction of Event Data) and rdseed (for converting to SAC format). All receiver function estimation, filtering, and migration software used in this dissertation were written by the author in the MATLAB scripting language. Synthetic seismograms were generated using the program SUPERPLANE (Aster and Shearer, 1991a,b). Yilmaz (1987) contains an excellent overview of seismic data analysis in the frequency-wavenumber domain as well as an overview of Kirchhoff migration. For more information or use of the codes used in this dissertation, please see http://www.ees.nmt.edu/ davew/, or contact the author directly via email at davew@ees.nmt.edu.

REFERENCES

Abers, G. A., Array measurements of phases used in receiver-function calculations: Importance of scattering, *Bull. Seis. Soc. Am., 88, n. 1,* 313-318, 1998.

Akaogi, M. and E. Ito, Calorimetric study on majorite-perovskite transition in the system $Mg_4Si_4O_{12}$−$Mg_3Al_2Si_3O_{12}$: transition boundaries with positive pressure-temperature slopes, *Physics of the Earth and Planetary Interiors, 114,* 129-140, 1999.

Aldrich, M. J., Jr., Laughlin, A. W., A model for the tectonic development of the southeastern Colorado Plateau boundary, *J. Geophys. Res., 89, n. B12,* 10207-10218, 1984.

Ammon, C.J., The isolation of receiver effects from teleseismic P-wave-forms, *Bull. Seis. Soc. Am., 81, n. 6,* 2504-2510, 1991.

Aster, R., and P. Shearer, High-Frequency borehole seismograms recorded in the San Jacinto fault zone, Southern California. Part 1: Polarizations, *Bull. Seism. Soc. Am., 81,* 1057-1080, 1991a.

Aster, R., and P. Shearer, High-frequency borehole seismograms recorded in the San Jacinto fault zone, Southern California Part 2: Attenuation and Site Effects, *Bull. Seism. Soc. Am., 81,* 1081-1100, 1991b.

Baldridge, W.S., F. Perry, D. Vaniman, L. Nealey, B. Leavy, A. Laughlin, P. Kyle, Y. Bartov, G. Steinitz, and E. Gladney, Middle to Late Cenozoic Magmatism of the Southeastern Colorado Plateau and Central Rio-Grande Rift (New-Mexico and Arizona, USA) - A Model for Continental Rifting, *Tectonophysics, 197,* 327-354, 1991.

Baldridge, W.S., G.R. Keller, V. Haak, E. Wendlandt, G.R. Jiracek, and K.H. Olsen, The Rio Grande Rift, from Olsen, K.H., ed., *Continental Rifts: Evolution, Structure, Tectonics, Developments in Geotectonics, 25,* Elsevier, 233-273, 1995.

Beauduin, P., P. Lognonne, J. Montagner, S. Cacho, J. Karczewski, M. Morand, The effects of atmospheric pressure changes on seismic signals, or how to improve the quality of a station, *Bull. Seism. Soc. Am., 86,* 1760-1799, 1996.

Bina, C. and G. Helffrich, Phase transition Clapeyron slopes and transition zone seismic discontinuity topography, *J. Geophys. Res., 99, n. B8,* 15853-15860, 1994.

Bostock, M. G., S. Rondenay, Migration of scattered teleseismic body waves *Geophys. Jour. Int., 137, n. 3,* 732-746, 1999.

Bostock, M., S. Rondenay, and J. Shragge, Multiparamter two-dimensional inversion of scattered teleseismic body waves, 1, Theory for oblique incidence, *J. Geophys. Res., 106,* 30785-30796, 2001.

Bowring, S.A., and K.E. Karlstrom, Growth, stabilization, and reactivation of Proterozoic lithosphere in the Southwestern United States, *Geology, 18, n. 12,* 1203-1206, 1990.

Bracewell, R., The Fourier Transform and its Applications, 3rd ed., McGraw Hill, ISBN 0-07-303938-1, 2000.

Buck, R.W., Small-scale convection induced by passive rifting: the cause for uplift of rift shoulders, *Earth Planet. Sci. Letts., 77,* 362-372, 1986.

Buck, R.W., F. Martinez, M. S. Steckler, J.R. Cochran, Thermal Consequences of Lithospheric Extension: Pure and Simple, *Tectonics, 7,* 213-234, 1988.

Butler, R. and C.R. Hutt, Seismic noise on Rarotonga: surface versus downhole, *EOS Trans. Am. Geophys. Union., 73,* 548-549, 1992.

Cassidy, J.F., Numerical Experiments in Broadband Receiver Function Analysis, *Bull. Seis. Soc. Am., 82, n. 3,* 1453-1474, 1992.

Chapin, C.E. and S.M. Cather, Tectonic Setting of the Axial Basins of the Northern and Central Rio Grande Rift, *Geol. Soc. Amer. Special Paper 291,* 5-24, 1994.

Clayton, R., and R. Wiggins, Source shape estimation and deconvolution of teleseismic body waves, *Geophys. J. R. Astr. Soc., 47,* 151-177, 1976.

Condie, K.C., Plate-tectonics model for Proterozoic continental accretion in the southwestern United States, *Geology, 10, n. 1,* 37-42, 1982.

Condie, K.C., Geochemistry and Tectonic Setting of Early Proterozoic Supracrustal Rocks in the Southwestern United States, *Journal of Geology, 94,* 845-864, 1986.

Condie, K.C., and J. Selverstone, The Crust of the Colorado Plateau: New Views of an Old Arc, *Geology, 107,* 387-397, 1999.

Cordell, L., Y.A. Zorin, and G.R. Keller, The Decompensative Gravity Anomaly and Deep Structure of the Region of the Rio-Grande Rift, *Jour. Geoph. Res., 96,* 6557-6568, 1991.

Crawford, W., and S. Webb, Identifying and removing tilt noise from low-frequency (< 0.1 Hz) seafloor vertical seismic data, *Bull. Seism. Soc. Am., 90,* 952-963, 2000.

Davis, P.M., Continental Rift Structures and Dynamics with Reference to Teleseismic Studies of the Rio-Grande and East-African Rifts, *Tectonophysics, 197,* 309-325, 1991.

Dellinger, J. A., S.H. Gray, G.E. Murphy, and J.T. Etgen, Efficient 2.5-D true-amplitude migration, *Geophysics, 65, n. 3,* 943-950, 2000.

Dickinson, W.R., and W.S. Snyder, Plate Tectonics of the Laramide Orogeny, *Geol. Soc. of Amer., Memoir 151,* 355-366, 1978.

Dueker K.G., and A.F. Sheehan, Mantle discontinuity structure beneath the Colorado Rocky Mountains and High Plains *J. Geophys. Res., 103, n. B4,* 7153-7169, 1998.

Dunbar, J., and D. Sawyer, Continental Rifting at Pre-existing lithospheric weaknesses, *Nature, 333,* 450-452, 1988.

Duquet B., K. Marfurt, and J.A. Dellinger, Kirchhoff modeling, inversion for reflectivity, and subsurface illumination, *Geophysics, 65,* 1195-1209, 2000.

Eaton, D. W., J. Hope, and T. Bohlen, An Elastic Kirchhoff Method for Computing Synthetic Seismograms: Modeling the Receiver-function Response of an Irregular Moho Surface. SSA 97th annual meeting abstracts, *Seismological Res. Letts., 73, n. 2,* 232, 2002.

Fan, C., G. Pavlis, A. Weglein, and H. Zhang, Multiparamter Inversion of Forward Scattered Teleseismic Data Using an Inverse Scattering Series Method, *Eos Trans. AGU, 84(46),* Fall Meet. Suppl., Abstract S11E-0353, 2003.

Frey, B.A., K. C. Condie, and R. Kerrich, The Iron King Volcanics; a remnant of an oceanic plateau accreted to southwestern Laurentia 1.7 Ga, *Geological Society of America, Rocky Mountain Section, 53rd annual meeting, Abstracts with Programs, Geological Society of America, 33, n. 5,* 24, 2001.

Gao, W., S. Grand, W.S. Baldridge, D. Wilson, M. West, J. Ni, and R. Aster, Upper mantle convection beneath the central Rio Grande rift imaged by P and S wave tomography, *J. Geophys. Res., 109,* B03305, doi:10.1029/2003JB002743, 2004.

Given, H. K., Variations in broadband seismic noise at IRIS/IDA stations in the USSR with implications for event detection, *Bull. Seism. Soc. Am. 80,* 2072-2088, 1990.

Given, H. K., F. Fels, Site characteristics and ambient ground noise at IRIS IDA stations AAK (Ala-Archa, Kyrgyzstan) and LY (Talaya, Russia), *Bull. Seism. Soc. Am. 83,* 945-953, 1993.

Gok, R., J.F. Ni, E. Sandvol, D. Wilson, W.S. Baldridge, R. Aster, M. West, S. Grand, W. Gao, F. Tilmann, and S. Semken, Shear wave splitting and mantle flow beneath LA RISTRA, *Geophys. Res. Lett., 30,* 1614, doi:10.1029/2002GL016616, 2003.

Grand, S.P., and D. Helmberger, Upper mantle shear structure of North America, *Geophys. J. R. Astron. Soc., 76,* 399-438, 1984.

Gurrola, H., J. B. Minster, H. Given, F. Vernon, J. Berger, and R. Aster, Analysis of high frequency seismic noise in the western United States and eastern Kazakhstan, *Bull. Seism. Soc. Am., 80,* 951-970, 1990.

Henyey, T., EarthScope: A look into our continent, *Geotimes, 45,* 5-7, 2000.

Huismans, R.S., Y.Y. Podladchikov, and S. Cloetingh, Transition from passive to active rifting: Relative importance of asthenospheric doming and passive extension of the lithosphere, *Jour. Geophys. Res., 106,* 11271-11291, 2001.

Humphreys, D., Post-Laramide removal of the Farallon slab, western United States, *Geology, 23,* 987-990, 1995.

Keller, G.R. et al., A Comparative Study of the Rio Grande and Kenya Rifts, *Tectonophysics, 197,* 355-371, 1991.

Keller, G. R., and W. S. Baldridge, The Rio Grande rift: A geological and geophysical review, *Rocky Mountain Geology, 34,* 131-148, 1999.

Kennett, B. and van der Hilst, R., Using a synthetic continental array to study the earth's interior, *Journal Phys. Earth., 44,* 669-674, 1996.

Kluth, C.F. and P.J. Coney, Plate tectonics of the Ancestral Rocky Mountains, *Geology, 9,* 10-15, 1981.

Langston, C.A., Corvallis, Oregon, Crustal and Upper Mantle Receiver Structure from Teleseismic P and S waves, *Bull. Seis. Soc. Am., 67,* 713-724, 1977.

Lee, C., Q. Yin, R.L. Rudnick, and S. B. Jacobsen, Preservation of ancient and fertile lithospheric mantle beneath the southwestern United States, *Nature, 411, n. 6833,* 69-73, 2001.

Leon, J., Seismic background noise along the RISTRA array of broadband seismic stations extending from west Texas to southeast Utah, New Mexico Institute of Mining and Technology, Indepent Study, 2001.

Levander, A., USArray design implications for wavefield imaging in the lithosphere and upper mantle, *The Leading Edge, 22, n. 3,* 250-255, 2003.

Li, A., K. M. Fischer, S. van der Lee, and M. E. Wysession, Crust and upper mantle discontinuity structure beneath eastern North America, *J. Geophys. Res., 107, n. B5,* 10.1029/2001JB000190, 2002.

Marshak, S., K. Karlstrom, and J.M. Timmons, Inversion of Proterozoic Extensional Faults: An Explanation for the pattern of Laramide and Ancestral Rockies Intracratonic Deformation, United States, *Geology, 28, n. 8,* 735-738, 2000.

Marshak, S., and T. Paulsen, Midcontinent U.S. fault and fold zones: A legacy of Proterozoic Intracratonic Extensional Tectonism?, *Geology, 24, n. 2,* 151-154, 1996.

McKenzie, D., Some remarks on the development of sedimentary basins, *Earth Planet. Sci. Lett., 40,* 25-32, 1978.

McMillan, N. J., Temporal and Spatial Magmatic Evolution of the Rio Grande Rift, *New Mexico Geological Society Guidebook, 49,* 107-116, 1998.

Morgan, P, W. Seager, and M. Golombek, Cenozoic Thermal, Mechanical and Tectonic Evolution of the Rio Grande Rift, *Jour. Geophys. Res., 91,* 6263-6276, 1986.

Mosher, S., Tectonic evolution of the southern Laurentian Grenville orogenic belt, *GSA Bulletin, 110, n. 11,* 1357-1375, 1998.

Mutter, J., W.R. Buck, and C. Zehnder, Convective Partial Melting, 1, A Model for the Formation of Thick Basaltic Sequences During the Initiation of Spreading, *Jour. Geophys. Res., 93,* 1031-1048, 1988.

Nemeth, T., C. Wu, and G.T. Schuster, Least-squares migration of incomplete reflection data, *Geophysics, 64,* 208-221, 1999.

Olsen, K.H., G.R. Keller, and J.N. Stewart, Crustal structure along the Rio Grande Rift from seismic refraction profiles, in *Rio Grande Rift; tectonics and magmatism,* 127-143, 1979.

Olsen, K.H., W. S. Baldridge, and J. F. Callender, Rio Grande rift: an overview, *Tectonophysics, 143,* 119-139, 1987.

Parker, E.C., P.M. Davis, J.R. Evans, H.M. Iyer, and K.H. Olsen, Upwarp of anomalous asthenosphere beneath the Rio Grande rift, *Nature, 312,* 354-356, 1984.

Perry, F.V., W.S. Baldridge, and D.J. DePaolo, Chemical and Isotopic Evidence for Lithospheric Thinning Beneath the Rio-Grande Rift, *Nature, 332,* 432-434, 1988.

Peterson, J., Observations and modeling of seismic background noise, *Open-File Report 93-322,* U.S. Department of Interior Geological Survey, 1993.

Poppliers, C. and G.L. Pavlis, Three-dimensional, prestack, plane wave migration of teleseismic P-to-S converted phases: 1. Theory, *J. Geophys. Res., 108,* 2112, doi:10.1029/2001JB000216, 2003.

Reed, J. C., Jr., T. T. Ball, G. L. Farmer, and W. B. Hamilton, A broader view, in *Precambrian: Conterminous U. S., The Geology of North America, C-2,* edited by J. C. Reed, Jr. and others, Geol. Soc. Amer., Boulder, Colo., 614-622, 1993.

Reiter, M., R.E. Eggleston, B.R. Broadwell, J. Minier, Estimates of terrestrial heat flow from deep petroleum tests along the Rio Grande Rift in central and southern New Mexico, *Jour. Geophys. Res., 91,* 6225-6245, 1986.

Riter, J.C.A. and D. Smith, Xenolith constraints on the thermal history of the mantle below the Colorado Plateau, *Geology, 24, n. 3,* 267-270, 1996.

Roden, M.F., and N. Shimizu, Ion microprobe analyses bearing on the composition of the upper mantle beneath the Basin and Range and Colorado Plateau provinces, *J. Geophys. Res., 98,* 14091-14108, 1993.

Roden, M.F., and N. Shimizu, Trace element abundances in mantle-derived minerals which bear on compositional complexities in the lithosphere of the Colorado Plateau, *Chem. Geol., 165,* 283-305, 2000.

Rodgers, P. W., S. R. Taylor, and K. K. Nakanishi, System and site noise in the regional seismic test network from 0.1 to 20 Hz, *Bull. Seism. Soc. Am. 77,* 663-678, 1987.

Roller, J.C., Crustal structure in the eastern Colorado Plateau province from seismic refraction measurements, *Bull. Seismol. Soc. Am., 55,* 107-119, 1965.

Russell, L. R. and S. Snelson, Structural style and tectonic evolution of the Albuquerque Basin segment of the Rio Grande Rift, New Mexico, U.S.A., in Interior rift basins, S. Landon, ed., *AAPG Memoir, 59,* 205-258, 1994.

Ryberg, T., M. Weber, Receiver function arrays: a reflection seismic approach, *Geophys. J. Int. 141,* p.1-11, 2000.

Seager, W.R., and P. Morgan, Rio Grande Rift in southern New Mexico, West Texas, and northern Chihuahua in *Rio Grande Rift; tectonics and magmatism,* 87-106, 1979.

Selverstone, J., A. Pun, K.C. Condie, Xenolithic evidence for Proterozoic crustal evolution beneath the Colorado Plateau, *Geol. Soc. Amer. Bull., 111, n. 4,* 590-606, 1999.

Sheehan A.F., G.A. Abers, C.H. Jones, and A.L. Lerner-Lam, Crustal thickness variations across the Colorado Rocky Mountains from teleseismic receiver functions, *J. Geophys. Res., 100,* 20391-20404, 1995.

Sheehan A.F., P.M. Shearer, H.J. Gilbert, and K.G. Dueker, Seismic migration processing of P-SV converted phases for mantle discontinuity structure beneath the Snake River Plain, western United States, *J. Geophys. Res., 105, n. B8,* 19055-19065, 2000.

Shragge, J. and B. Artman, Wave-equation Imaging of Teleseismic Body-wave Coda, *Eos Trans. AGU, 84(46),* Fall Meet. Suppl., Abstract S11E-0335, 2003.

Sinno, Y.A., and G.R. Keller, A Rayleigh Wave Dispersion Study Between El Paso, Texas and Albuquerque, New Mexico, *J. Geophys. Res., 91, n. B6,* 6168-6174, 1986.

Slack, P.D., P. Davis, W.S. Baldridge, K.H. Olsen, A. Glahn, U. Achauer, and W. Spence, The upper mantle structure of the central Rio Grande Rift region from teleseismic P- and S- wave travel time delays and attenuation, *J. Geophys. Res., 101,* 16,003-16,023, 1996.

Sloss, L.L. editor, Sedimentary cover, North American Craton, U.S., *The Geology of North America, D-2*, 1988.

Smith, D., Insights into the evolution of the uppermost continental mantle from xenolith localities on and near the Colorado Plateau and regional conparisons, *J. Geophys. Res., 105, n. B7,* 16769-16781, 2000.

Smith, D., D. E. Moser, J. Connelly, K. Manser, and D. Schulze, U-Pb Zircon Ages of Eclogites, Garnetites, and Cenozoic Rock-Water Reactions in Proterozoic Mantle Below the Colorado Plateau, *GSA 2002 Annual Meeting Abstracts with Programs,* 2002.

Stewart, S. W. and L. C. Pakiser, Crustal structure in eastern New Mexico interpreted from the GNOME explosion, *Bull. Seismol. Soc. Am., 52,* 1017-1030, 1962.

Stolt, R. H., and A. K. Benson, Seismic migration - theory and practice, *Geophysical Press, London-Amsterdam,*, 1986.

Tessmer, G., and A. Behle, Common reflectio point data stacking technique for converted waves, *Geophys. Prosp, 36,* 671-688, 1988.

Toppozada, T.R., Sanford, A.R., Crustal structure in central New Mexico interpretation from the Gasbuggy explosion, *Bull. Seismol. Soc. Am., 66,* 877-886, 1976.

Uhrhammer, R. A., Background Noise PSD Analysis of USNSN Broadband Data for 1998, *Berkeley Seismological Laboratory report,* 22 pages, 2000.

Vila, J., The broadband seismic station CAD (Tunel del Cadi, eastern Pyrenees): Site characteristics and background noise, *Bull. Seism. Soc. Am. 88,* 297-303, 1998.

Weissel, J.K., and G.D. Karner, Flexural Uplift of Rift Flanks Due to Mechanical Unloading of the Lithosphere During Extension, *J. Geophys. Res., 94,* 13919-13950, 1989.

Welch, P., The use of Fast Fourier Transform for the estimation of power spectra: a method based on time averaging over short, modified periodograms, *IEEE Trans. Audio Electroacoustics, AU15,* 70-73, 1967.

Wendlandt, E., D. J. DePaolo, and W. S. Baldridge, Nd and Sr isotope chronostratigraphy of Colorado Plateau lithosphere: implications for magmatic and tectonic underplating of the continental crust, *Earth Planet. Sci. Lett., 116,* 23-43, 1993.

Wernicke, B., Uniform Sense Normal Simple Shear of the Continental Lithosphere, *Canadian. Jour. Earth. Sci., 22,* 108-125, 1985.

West, M., J. Ni, W.S. Baldridge, D. Wilson, R. Aster, W. Gao, and S. Grand, Crust and upper mantle shear wave structure of t he southwest United States: Implications for rifting and support for high elevation, *J. Geophys. Res., 109,* B03309, do i:10.1029/2003JB002575, 2004.

Wilson, J. Leon, R. Aster, J. Ni, J. Schlue, S. Grand, S. Semken, S. Baldridge, and W. Gao, Broadband Seismic Background Noise at Temporary Seismic Stations Observed on a Regional Scale in the Southwestern United States, *Bull. Seismol. Soc. Amer., 92,* 3335-3341 2002.

Wilson, D., R. Aster, and the RISTRA Team, Imaging Crust and Upper Mantle Seismic Structure in the Southwestern United States Using Teleseismic Receiver Functions, *The Leading Edge, 22,* 232-237, 2003.

Wilson D., M. West, R. Aster, J. Ni, W. Gao, S. Grand, W.S. Baldridge, S. Semken, Lithospheric Structure of the Rio Grande Rift, Nature, in review, 2004.

Wilson, D., R. Aster, J. Ni, S. Grand, M. West, W. Gao, W.S. Baldridge, and S. Semken, Imaging the Seismic Structure of the Crust and Upper Mantle Using Receiver Functions, Part 1: Methods, in preparation, JGR, 2004

Wilson, D., R. Aster, J. Ni, S. Grand, M. West, W. Gao, W.S. Baldridge, and S. Semken, Imaging the Seismic Structure of the Crust and Upper Mantle Using Receiver Functions, Part 2: Application to the LA RISTRA Network, in preparation, JGR, 2004

Withers, M. M., R. C. Aster, C. J. Young, and E.P. Chael, High frequency analysis of seismic background noise as a function of wind speed and shallow depth, *Bull. Seism. Soc. Am. 86,* 1507-1515, 1996.

Yilmaz, Ö., Seismic Data Processing, *Society of Exploration Geophysicists*, 240-383, 1987.

Young, C. J., E. P. Chael, M. M. Withers, and R. C. Aster, A comparison of high frequency ($\geq$1 Hz) surface and subsurface noise environment at three sites in the United States, *Bull. Seism. Soc. Am. 86,* 1516-1528, 1996.

Yuan, X., J. Ni, R. Kind, J. Mechie, and E. Sandvol, Lithospheric and upper mantle structure of southern Tibet from a seismological passic source experiment, *J. Geophys. Res., 102, n. B12,* 27491-27500, 1997

Zandt, G. and C.J. Ammon, Continental crust composition constrained by measurements of crustal Poisson's ratio, *Nature, 374,* 152-154, 9 March, 1995.

Zhu, L. and H. Kanamori, Moho depth variation in southern California from teleseismic receiver functions, *J. Geophys. Res., 105, n. B2,* 2969-2980, 2000.

Zurn, W, and R. Widmer, On noise-reduction in vertical seismic records below 2 mHz using local barometric-pressure, *Geop. Res. Lett., 22,* 3537-3540, 1995.